

The Visualization of the Human Brain Post Mortem

Inauguraldissertation

zur

Erlangung der Würde eines Doktors der Philosophie

vorgelegt der

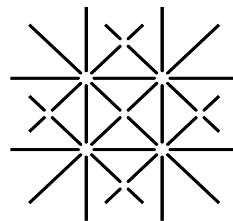
Philosophisch-Naturwissenschaftlichen Fakultät

der Universität Basel

von

Georg Schulz

aus Deutschland



**UNI
BASEL**

Basel, 2012

Genehmigt von der Philosophisch-Naturwissenschaftlichen Fakultät auf Antrag von:

Prof. Dr. Bert Müller, Fakultätsverantwortlicher
Prof. Dr. Ernst Meyer, Korreferent

Basel, den 26. Juni 2012

Prof. Dr. Martin Spiess, Dekan

Contents

Summary	v
Zusammenfassung	vii
List of Publications	ix
1 Introduction	1
2 Results	5
2.1 Deformations resulting from formalin fixation of the whole brain . . .	5
2.2 Deformations resulting from histology	17
2.3 Grating-based phase contrast X-ray SR μ CT of the human cerebellum	27
2.4 Multimodal imaging: PC- μ CT, μ MRI and histology	41
3 Conclusions	49
Bibliography	54
Acknowledgements	55
Curriculum Vitae	57

Summary

Minimally invasive deep brain neurosurgical interventions require a profound knowledge of the human brain morphology on the micrometer level. Generic brain atlases are based on histology including multiple preparation steps like sectioning and staining. Before the histological analysis of the human brain post mortem, the first preparation step is the extraction of it from the cranium. After that, formalin fixation of the brain is often performed. As the brain consists of inhomogeneous tissues, these steps lead to a three-dimensional strain field within the brain.

For the correction of these deformations three-dimensional magnetic resonance imaging has been used. In a single investigation, the brain was first examined post mortem within the cranium. After extraction, 13 magnetic resonance data sets were acquired over a fixation period of 70 days and compared to the initial data set. Using an affine registration of the data sets, the global volume shrinkage was found to be 8.1%. The local volume strains could be determined by means of a non-rigid registration. The study revealed maximal local volume strains of 32%.

In order to correct the distortions induced within the anisotropic, inhomogeneous soft matter by sectioning and staining and therefore to improve the accuracy of brain atlases, a non-destructive three-dimensional imaging technique with the required spatial resolution and contrast is of great significance. Micro-computed tomography provides true micrometer resolution. The application to post mortem human brain, however, is questionable because the differences of the components concerning X-ray absorption are weak. Therefore, magnetic resonance imaging has become the method of choice for three-dimensional imaging of human brain. Because of the limited spatial resolution of this method, an alternative has to be found for the three-dimensional imaging of microstructures within the brain. Therefore, synchrotron radiation-based microtomography in the recently developed grating-based X-ray phase contrast mode was used for the visualization of the brain tissue. Using data acquired at the beamline ID 19 (ESRF, Grenoble, France) it was demonstrated that grating-based microtomography yields premium images of human thalamus. This data can be used for the correction of histological distortions using three-dimensional non-rigid registration.

Grating-based phase contrast tomography can also be applied on the human cerebellum, another very important part of the human brain. Simultaneously this technique gives access to absorption contrast tomography. These two data sets are quantitatively compared with synchrotron radiation-based microtomography in optimized absorption contrast mode. It was demonstrated that, in addition to the blood vessels, grating interferometry identifies the stratum moleculare, the stratum granulosum and the white matter. Along the periphery of the stratum granulosum, microstructures of about 40 μm in diameter were detected, which were associated with the Purkinje cells because of their location, size, shape and density. The detection of individual Purkinje cells without the application of any stain or contrast agent is unique in the field of computed tomography and sets new standards in

non-destructive three-dimensional imaging.

Another well established imaging technique for the visualization of the human brain is magnetic resonance imaging which is known for its high contrast between white and gray matter. Unfortunately, the spatial resolution of the conventional medical magnetic resonance scanners is not sufficient enough to investigate the microanatomy of the brain. The required spatial resolution can be achieved by magnetic resonance microscopy using a small animal magnetic resonance scanner which takes advantage of a magnetic field of 9.4 T. These results were compared with grating-based phase contrast data sets. It was demonstrated that grating-based phase tomography using hard X-rays yields for human cerebellum comparable contrast values to magnetic resonance microscopy whereas the quality factors based on contrast and spatial resolution, for phase tomography, are obviously higher. The combination of the three complementary imaging techniques, namely phase contrast tomography, magnetic resonance microscopy and histology, permits the distinct segmentation of four tissues within the human cerebellum.

Zusammenfassung

Minimal-invasive neurochirurgische Eingriffe erfordern ein fundiertes Wissen über die Morphologie des menschlichen Gehirns auf der Mikrometer-Skala. Generische Gehirnatlantent, die dazu verwendet werden und auf histologischen Schnitten basieren, erfordern mehrere Präparationsschritte, wie z.B. das Schneiden in dünne Schnitte, sowie das Färben dieser histologischer Schnitte. Bevor histologische Untersuchungen am menschlichen Gehirn nach Eintritt des Todes stattfinden können, erfolgt die Entnahme, sowie meistens die Formalinfixierung, um der einsetzenden Verwesung vorzubeugen. Da das Gehirn aus inhomogenem Gewebe besteht, führen diese ersten Schritte zu lokalen Verzerrungen, die einem dreidimensionalen Spannungsfeld gleichen.

Zur Korrektur dieser Deformationen eignet sich insbesondere die Kernspintomographie. Während der vorliegenden Studie wurde das Gehirn zunächst innerhalb des Schädels, jedoch nach Eintreten des Todes, untersucht. Danach wurden 13 Datensätze über den gesamten Fixierungszeitraum von 70 Tagen mit Hilfe eines medizinischen Kernspintomographen erzeugt. Diese Datensätze wurden dann mit dem Anfangsdatensatz verglichen. Die globale Volumenabnahme von 8.1% konnte mit Hilfe einer affinen Registrierung berechnet werden. Mit nichtrigiden Registrierungen wurden zusätzlich dazu maximale lokale Volumenänderungen von bis zu 32% bestimmt.

Die darauf folgenden Präparationsschritte, insbesondere das Schneiden und das Färben der Schnitte, verursachen ebenfalls Verzerrungen des anisotropen und inhomogenen Gehirngewebes und führen so zu Ungenauigkeiten der Gehirnatlantent. Für eine Korrektur der Deformationen benötigt man ein zerstörungsfreies, dreidimensionales Bildgebungsverfahren, welches die benötigte räumliche Auflösung aufweisen kann. Mikro-Computertomographie bietet eine räumliche Auflösung von wenigen Mikrometern, kann jedoch die Anforderungen an den Kontrast nicht erfüllen, da die Unterschiede der Strukturen im Gehirn in Bezug auf Absorption der Röntgenstrahlen zu gering sind. Daher gilt bisher die Kernspintomographie als beste Methode, um dreidimensionale Visualisierungen vom Gehirn zu erzeugen. Jedoch genügt die räumliche Auflösung dieser Methode nicht den Anforderungen, die für die Korrektur der histologischen Schnitte benötigt wird. Die jüngst entwickelte gitterbasierte Phasenkontrast Mikro-Computertomographie an Synchrotronstrahlungsquellen bietet eine Alternative, um zelluläre Strukturen im Gehirn zu visualisieren. Mit den Daten, die an der Beamline ID 19 (ESRF, Grenoble, Frankreich) generiert wurden, konnte gezeigt werden, dass sich gitterbasierte Tomographie hervorragend zum Erzeugen hochqualitativer Bilder des menschlichen Thalamus eignet. Die Datensätze konnten schliesslich mit Hilfe der nichtrigiden Registrierung für die Korrektur der histologischen Schnitte verwendet werden, um die Genauigkeit eines Gehirnatlases zu erhöhen.

Die Anwendung der gitterbasierten Phasenkontrasttomographie kann auch auf das menschliche Kleinhirn, welches ein sehr wichtiger Teil des menschlichen Gehirns ist, ausgeweitet werden. Neben den Phasenkontrastdaten liefert diese Technik si-

multan auch Absorptionskontrastdaten, die jedoch nicht unter Absorptionskontrast-Bedingungen erzeugt werden können. Diese beiden Datensätze wurden quantitativ mit Ergebnissen, die mit optimierten Absorptionskontrast-Bedingungen aufgenommen wurden, verglichen. Es wurde gezeigt, dass sich die Phasenkontrasttomographie hervorragend dafür eignet, neben Blutgefäßen auch die Molekularschicht, die Körnerschicht sowie die weisse Substanz zu identifizieren. Entlang der Peripherie der Körnerschicht konnten Strukturen mit etwa 40 μm Durchmesser nachgewiesen werden, die aufgrund ihrer Lage, Grösse, Form und Dichte als Purkinje-Zellen identifiziert wurden. Dieser Nachweis von einzelnen Purkinje-Zellen ohne den Einsatz von Kontrastmitteln ist einzigartig auf dem Gebiet der Computertomographie und setzt neue Maßstäbe in der zerstörungsfreien dreidimensionalen Bildgebung.

Ein weiteres gut etabliertes Bildgebungsverfahren zur Visualisierung des menschlichen Gehirns ist die Kernspintomographie, die für einen hohen Kontrast zwischen weisser und grauen Substanz bekannt ist. Leider ist die räumliche Auflösung der konventionellen medizinischen Kernspin-Scanner nicht ausreichend genug, um Mikrostrukturen des Gehirns zu erforschen. Die erforderliche räumliche Auflösung kann durch Kernspin-Mikroskopie, unter Verwendung eines Kernspintomographen für Kleintiere mit einer Magnetfeldstärke von 9.4 T, erreicht werden. Die Resultate der Kernspin-Mikroskopie wurden mit den Datensätzen der gitterbasierten Phasenkontrast-Tomographie verglichen, mit dem Ergebniss, dass gitterbasierte Phasenkontrast-Tomographie mit harter Röntgenstrahlung bei der Visualisierung des menschlichen Kleinhirns vergleichbare Kontrastwerte zu der Kernspin-Mikroskopie hat, während die Qualität-Faktoren, die auf Kontrast und räumlicher Auflösung basieren, beim Phasenkontrast deutlich höher sind. Eine Kombination der drei sich ergänzenden Bildgebungsverfahren, nämlich der Phasenkontrast-Tomographie, Kernspin-Mikroskopie und Histologie, ermöglicht eine eindeutige Segmentierung von vier verschiedenen Gewebearten innerhalb des menschlichen Kleinhirns.

List of Publications

B. Müller, H. Deyhle, D. Bradley, M. Farquharson, **G. Schulz**, M. Müller-Gerbl, O. Bunk, “Scanning X-ray scattering: evaluating the nanostructure of human tissues.” *European Journal of Nanomedicine* **3**, 30-33 (2010). (doi:10.3884/0003.1.8)

G. Schulz, T. Weitkamp, I. Zanette, F. Pfeiffer, F. Beckmann, C. David, S. Rutishauser, E. Reznikova, B. Müller, “High-resolution tomographic imaging of a human cerebellum: comparison of absorption and grating-based phase contrast.” *Journal of the Royal Society Interface* **7**, 1665-1676 (2010). (doi:10.1098/rsif.2010.0281)

T. Weitkamp, I. Zanette, C. David, J. Baruchel, M. Bech, P. Bernard, H. Deyhle, T. Donath, J. Kenntner, S. Lang, J. Mohr, B. Müller, F. Pfeiffer, E. Reznikova, S. Rutishauser, **G. Schulz**, A. Tapfer J.-P. Valade, “Recent developments in X-ray Talbot interferometry at ESRF-ID19.” *Proceedings of SPIE* **7804**, 780406 (2010). (doi:10.1117/12.860203)

G. Schulz, A. Morel, M. Imholz, H. Deyhle, T. Weitkamp, I. Zanette, F. Pfeiffer, C. David, M. Müller-Gerbl, B. Müller, “Evaluating the microstructure of human brain tissues using synchrotron radiation-based micro computed tomography.” *Proceedings of SPIE* **7804**, 78040F (2010). (doi:10.1117/12.859273)

P. Cattin, **G. Schulz** M. Reyes, “Bildgebende Verfahren.” *Der MKG-Chirurg* **1**, 16-22 (2011). (doi:10.1007/s12285-010-0195-x)

G. Schulz, H.-J. Crooijmans, M. Germann, K. Scheffler, M. Müller-Gerbl, B. Müller, “Three-dimensional strain fields in human brain resulting from formalin fixation.” *Journal of Neuroscience Methods* **202**, 17-27 (2011). (doi:10.1016/j.jneumeth.2011.08.031)

G. Schulz, H. Deyhle, B. Müller, “Imaging the human body: Micro- and nanostructure of human tissues.” In: *Nanomedicine and Nanobiotechnology* (Ed. S. Logothetidis), Chapter 4, 69-94, Springer 2011. (doi:10.1007/978-3-642-24181-9)

B. Müller, H. Deyhle, S. Lang, **G. Schulz**, T. Bormann, F. Fierz, S. Hieber, “Three-dimensional registration of tomography data for quantification in biomaterials science.” *International Journal of Materials Research* **103**, 242-249 (2012). (doi:10.3139/146.110663)

H. Deyhle, **G. Schulz**, B. Müller, “Imaging the Human Body Down to the Molecular Level.” In: *Encyclopedia of Nanotechnology* (Eds. B. Bhushan, H.D. Winbigler), Springer 2012. (doi:10.1007/978-90-481-9751-4)

B. Müller, **G. Schulz**, A. Mehlin, J. Herzen, S. Lang, M. Holme, I. Zanette, S. Hieber, H. Deyhle, F. Beckmann, F. Pfeiffer, T. Weitkamp, “Grating-based tomography of human tissues.” *AIP Conference Proceedings* **1466**, 107-112 (2012). (doi:10.1063/1.4742277)

G. Schulz, T. Weitkamp, I. Zanette, F. Pfeiffer, M. Müller-Gerbl, C. David, B. Müller, “Asymmetric rotational axis reconstruction of grating-based phase contrast tomography of the human cerebellum.” *Proceedings of SPIE* **8506**, 850604 (2012). (doi:10.1117/12.928487)

G. Schulz, C. Waschkies, F. Pfeiffer, I. Zanette, T. Weitkamp, C. David, B. Müller, “Multimodal imaging of human cerebellum - merging X-ray phase microtomography, magnetic resonance microscopy and histology.” *Scientific Reports* **2**, 826 (2012). (doi:10.1038/srep00826)

Publications not directly related to the present thesis

B. Müller, S. Lang, M. Dominietto, M. Rudin, **G. Schulz**, H. Deyhle, M. Germann, F. Pfeiffer, C. David, T. Weitkamp, “High-resolution tomographic imaging of microvessels.” *Proceedings of SPIE* **7078**, 70780B (2008). (doi:10.1117/12.794157)

J. Roden, **G. Schulz**, A. Eisfeld, J. Briggs, “Electronic energy transfer on a vibronically coupled quantum aggregate.” *Journal of Chemical Physics* **131**, 044909 (2009). (doi:10.1063/1.3176513)

L. Kofmehl, **G. Schulz**, H. Deyhle, A. Filippi, G. Hotz, D. Berndt-Dagassan, S. Kramis, F. Beckmann, B. Müller, “Computed tomography to quantify tooth abrasion.” *Proceedings of SPIE* **7804**, 78041F (2010). (doi:10.1117/12.859278)

T. Bormann, S. Friess, M. de Wild, R. Schumacher, **G. Schulz**, B. Müller, “Determination of strain fields in porous shape memory alloys using micro computed tomography.” *Proceedings of SPIE* **7804**, 78041M (2010). (doi:10.1117/12.861386)

J. Herzen, F. Beckmann, T. Donath, M. Ogurreck, C. David, F. Pfeiffer, J. Mohr, E. Reznikova, S. Riekehr, A. Haibel, **G. Schulz**, B. Müller, A. Schreyer, “X-ray grating interferometer for imaging at a second-generation synchrotron radiation source.” *Proceedings of SPIE* **7804**, 780407 (2010). (doi:10.1117/12.860733)

B. Müller, **G. Schulz**, J. Herzen, S. Mushkolaj, T. Bormann, F. Beckmann, K. Püschel, “Morphology of urethral tissues.” *Proceedings of SPIE* **7804**, 78040D (2010). (doi:10.1117/12.859052)

S. Gürel, C. Unold, H. Deyhle, **G. Schulz**, S. Kühl, B. Saldamli, J. Tübel, R. Burgkart, F. Beckmann, B. Müller, “The microstructure of mandibular bone grafts and three-dimensional cell clusters.” *Proceedings of SPIE* **7804**, 78041G (2010). (doi:10.1117/12.859437)

B. Müller, H. Deyhle, **G. Schulz**, S. Mushkolaj, O. Bunk, “The nanostructure of biological tissues: a scanning X-ray scattering study.” *European Cells and Materials* **20**, Suppl. 3, 181 (2010). (ISSN 1473-2262)

A. Eisfeld, **G. Schulz**, J. Briggs, “The influence of geometry on the vibronic spectra of quantum aggregates.” *Journal of Luminescence* **131**, 2555-2564 (2011). (doi:10.1016/j.jlumin.2011.06.043)

Y.-C. Brogle-Kim, H. Deyhle, B. Müller, **G. Schulz**, T. Bormann, F. Beckmann, K. Jäger, “Evaluation of oral scanning in comparison to impression using three-dimensional registration.” *Proceedings of SPIE* **8506**, 85061R (2012). (doi:10.1117/12.929727)

C. Vögtlin, **G. Schulz**, H. Deyhle, K. Jäger, T. Liebrich, S. Weikert, B. Müller, “Comparison of denture models by means of micro computed tomography.” *Proceedings of SPIE* **8506**, 85061S (2012). (doi:10.1117/12.930068)

M. Holme, **G. Schulz**, H. Deyhle, S. Hieber, T. Weitkamp, F. Beckmann, J. Herzen, J. Lohrinus, F. Montecucco, F. Mach, A. Zumbuehl, T. Saxer, B. Müller, “Morphology of atherosclerotic coronary arteries.” *Proceedings of SPIE* **8506**, 850609 (2012). (doi:10.1117/12.930052)

H. Deyhle, T. Weitkamp, S. Lang, **G. Schulz**, A. Rack, I. Zanette, B. Müller, “Comparison of propagation-based phase-contrast tomography approaches for the evaluation of dentin microstructure.” *Proceedings of SPIE* **8506**, 85060N (2012). (doi:10.1117/12.929951)

1 Introduction

With approximately 10^{11} neurons and 10^{14} synapses [1] the brain is one of the most impressive structures in the human organism. Because of its outstanding functional importance there is a strong need for brain imaging modalities for diagnostics or navigation during treatments of brain diseases. For recently developed neurosurgical approaches, a profound knowledge of the morphology of the human brain down to the micrometer level is especially required. One such example is magnetic resonance (MR)-guided neurosurgery with high focused ultrasound (e.g., [2–4]), used to treat chronic neurophatic pain or movement disorders. With a spatial resolution of a fraction of a millimeter, conventional medical computed tomography (CT) or magnetic resonance imaging (MRI) scanners are not able to fulfill this requirement. Therefore, neurosurgeons use detailed stereotactic atlases based on histology (e.g. of the human brain [5] or the human thalamus and basal ganglia [6]) for orientation within the treated part. The advantages of the micrographs obtained by optical microscopy of the stained slices relate to reasonable contrast depending on the staining procedure and sub-micrometer resolution. However, the technique does not provide isotropic three-dimensional (3D) information of the brain as regularly obtained using CT and MRI. Another disadvantage is the deformation induced on the soft tissue during the multiple time-consuming preparation steps. Consequently, the histological slices do not reflect the exact situation of an intact brain. The aim of the present work is to find alternative non-destructive 3D imaging techniques with both reasonable contrast and a cellular spatial resolution. At the least, the spatial resolution should fulfill the requirement to correct the deformations induced during the different histological preparation steps.

Histological preparation steps

The first preparation step is the extraction of the brain from the cranium and the fixation in order to avoid its degradation. In the majority of cases, a formalin fixation is used. It is clear that the extraction procedure with its mechanical forces on the tissue causes deformations within the brain. But also during the fixation period, a global shrinkage and local deformations due to inhomogeneity of the brain tissue can be expected. The deformations due to formalin fixation can be explained by several physico-chemical reactions [7, 8]. Examinations on the influence of the formalin during fixation of the human brain stem are already reported [9]. These studies are based on length changes of 2D histological slices induced by the fixative. In order to determine volume changes of the brain tissue, 3D MRI data sets of the whole brain with sub-millimetre voxel lengths can be used. Conventional MRI is a non-destructive 3D imaging technique with high contrast between white and gray matter. The deformations can be extracted using 3D affine (global changes) and non-rigid (local strains) registrations [10] between the data sets of the brain post mortem within the cranium and after extraction after several fixation periods.

After several weeks of formalin fixation, the next steps are: (i) blocking of the investigated part, (ii) cryo-sectioning of the block into slices of several dozen micrometers and (iii) histochemical staining of the slices which enables the distinction between different nuclei and the fiber system. Obviously, all of these preparation steps have an influence on the soft tissue. After recording the images of the differently stained histological slices using optical microscopy, the micrographs have a spatial resolution on the sub-micrometer level. Because of the high difference in the spatial resolution between the micrographs and medical MRI data sets an alternative imaging technique with a spatial resolution on the micrometer level has to be found in order to determine these deformations. Conventional micro-computed tomography (μ CT) in absorption contrast mode fulfills the required spatial resolution, but does not show enough contrast within brain tissues despite the calculated differences in the Hounsfield numbers of white and gray matter [11]. However, synchrotron radiation-based μ CT (SR μ CT) with a much higher photon flux and tunable energies by the use of a monochromator allows for differentiation between brain tissues and so the correction of the histological slices, at least for human medulla oblongata [12]. Using a non-rigid registration, this 2D study demonstrated differences between the staining protocols. Unfortunately the contrast in the human medulla oblongata is already weak, so considerable doubt remains whether the contrast in absorption contrast is sufficient enough to visualize the human thalamus, an area which represents a major challenge in X-ray tomography because of the marginal differences of the absorption contrast values.

Phase contrast μ CT

For soft tissue, mainly consisting of hydrogen ($Z=1$), carbonate ($Z=6$) and oxygen ($Z=8$), X-ray tomography using the phase contrast mode is the better choice [14]. Contrary to absorption contrast, where the imaginary part $\beta(x, y, z)$ of the complex refractive index distribution

$$n(x, y, z) = 1 - \delta(x, y, z) + i\beta(x, y, z) \quad (1.1)$$

is measured, phase contrast μ CT (PC- μ CT) provides the decrement $\delta(x, y, z)$ of the real part of it. The imaginary part has a relation to the widely used linear X-ray attenuation coefficient $\mu(x, y, z)$ by the equation

$$\mu(x, y, z) = \frac{4\pi}{\lambda} \cdot \beta(x, y, z), \quad (1.2)$$

with the wavelength λ of the incident X-rays. For X-ray energies far away from the absorption edges $\delta(x, y, z)$ is related to the electron density distribution $\rho_e(x, y, z)$ by

$$\delta(x, y, z) = \frac{r_e \lambda^2}{2\pi} \rho_e(x, y, z), \quad (1.3)$$

with the classical electron radius r_e [13]. Nowadays, a variety of different principles exist which all are based on phase shifts of X-rays penetrating the specimen [15, 16].

The first approach which was based on a **crystal interferometer** was found 1965 by Bonse and Hart [17]. The idea is to split the beam where one part goes through the specimen and the second part of it is used as reference. The interference pattern

after the combination of the two beams provides information about the phase shift. Thus, this set-up allows a direct measurement of the profile of phase shifts induced into the X-ray wave by the specimen. Several applications exist where this technique was used to visualize soft tissue specimens (e.g. a rat cerebellum [14] or a mouse kidney [18]). The limitation of this imaging technique is the field of view because of technological constraints building the crystal interferometer.

Another, very widely used method is the **propagation-based** or **inline** phase contrast. As the method requires a sufficient degree of spatially coherent X-ray beam, the first experiments were only carried out in the mid 1990s after the first third-generation synchrotron light sources went into operation [19–22]. One big advantage of this method is that no additional optical components are needed as the Fresnel diffraction in the space between specimen and detector creates the contrast. A prominent implementation of this principle is known as **holotomography** where images are recorded at several distances behind the specimen and combined to quantitatively retrieve the phase shift [23]. This method was recently used for the only known 3D representation of a fossilized brain so far [24].

A third approach relevant for soft tissue is **analyzer-based imaging** (ABI). Using an analyzer crystal between the specimen and detector the phase shift of monochromatic X-rays induced by the specimen can be uncovered [25, 26]. A big advantage of the method is that it simultaneously gives access to absorption, refraction and scattering if suitable data analysis as shown for **diffraction-enhanced imaging** (DEI) is adopted [27]. Nevertheless, ABI requires a monochromatic X-ray beam with small divergence and high-quality, sufficiently large analyzer crystals.

For specimens with low contrast values, which is the case in the brain tissue, the recently developed **grating** or **Talbot interferometry** [28–30] shows excellent results [31, 32]. The idea here is to detect slight deflection angles of the incident X-rays caused by the phase object. The deflection angles $\alpha(y, z)$ are related to the first derivative of the phase shift $\Phi(y, z)$ [33] by the equation

$$\alpha(y, z) = \frac{\lambda}{2\pi} \frac{\partial \Phi(y, z)}{\partial y} = \int_{-\infty}^{\infty} \frac{\partial \delta(x, y, z)}{\partial y} dx. \quad (1.4)$$

As the deflection angles are smaller than the pixel sizes of the detector, a grating interferometer, consisting of a beam-splitter and an analyzer grating, is used. Analysis of the phase-stepping data [30] yields the deflection angle $\alpha(y, z)$ and, simultaneously, additional information related to absorption contrast and to small-angle scattering comparable to DEI. Recent developments of grating-based PC- μ CT, by including an additional attenuation grating, allow the use of polychromatic sources like X-ray tubes or low-brilliance sources like second-generation synchrotron sources [34, 35].

Human cerebellum

Besides the application of the grating based PC- μ CT for the correction of the histological slices, this method can be used for the visualization of a second very interesting part of the human brain. With more than 50 billion neurons, most of them located in the cerebellar cortex, the human cerebellum includes around 50 per

cent of the neurons of the entire brain [36]. The nerve center, where the impulses of almost all neurons of the cerebellar cortex converge and are transferred to their destination beyond the cortex, is formed by the so-called Purkinje cells. These cells exhibit spherical shapes with diameters of about 40-70 μm and are the largest cells of the cerebellum. So far, only osmium-stained ganglion cells have been made visible using SR μCT in absorption-contrast mode [37]. Regarding the sensitivity and the possible spatial resolution of around 10 μm , grating-based PC- μCT should have the ability to visualize individual Purkinje cells, surrounded by soft tissue, without the application of any contrast agent, which would be unique in the field of X-ray computed tomography.

Multimodal imaging

To date, two different imaging methods have been described which can be used for the visualization of the microstructure of the human brain, namely histology and PC- μCT . Conventional medical MRI, which is known for its superb contrast between white and gray matter, unfortunately is not able to fulfill this condition. The reason for that is the spatial resolution. At present, medical MRI generates images with sufficient contrast-to-noise ratio and reasonable scanning times, but which do not have voxel lengths below the sub-millimeter range.

Taking advantage of higher magnetic fields ($\sim 9\text{ T}$) (versus a magnetic field of a medical MRI scanner of $\lesssim 3\text{ T}$) and stronger gradient systems, small animal MR-scanners have already been used to visualize mice brains in vivo [38, 39] and human brain blocks post mortem [40, 41] with voxel sizes of a few tens of micrometers. Because of the higher spatial resolution the method is usually called magnetic resonance microscopy (μMRI). All of the techniques listed so far (PC- μCT , μMRI and histology) have inherent advantages and disadvantages. In particular, all of them have complementary information. A combination of the three data sets would result in comprehensive information on the microanatomy of the human cerebellum.

2 Results

2.1 Deformations resulting from formalin fixation of the whole brain

The manuscript presents a possibility to calculate the strain field within the brain induced by extraction and formalin fixation. The study is based on a comparison, using affine and non-rigid registration algorithms, of magnetic resonance imaging data sets at different preparation steps.

Published in Journal of Neuroscience Methods



Three-dimensional strain fields in human brain resulting from formalin fixation

Georg Schulz^{a,*}, Hendrikus J.A. Crooijmans^b, Marco Germann^a, Klaus Scheffler^{c,d},
Magdalena Müller-Gerbl^e, Bert Müller^a

^a Biomaterials Science Center, University of Basel, c/o University Hospital Basel, 4031 Basel, Switzerland

^b Radiological Physics, Department of Medical Radiology, University of Basel, University Hospital Basel, 4031 Basel, Switzerland

^c Magnetic Resonance Center, Max Planck Institute for Biological Cybernetics, Spemannstrasse 38-44, 72076 Tübingen, Germany

^d Department of Neuroimaging and MR-Physics, University of Tübingen, Paul-Ehrlich-Str. 15, 72076 Tübingen, Germany

^e Macroanatomy, Institute of Anatomy, University of Basel, Pestalozzistrasse 20, 4056 Basel, Switzerland

ARTICLE INFO

Article history:

Received 20 May 2011

Received in revised form 12 August 2011

Accepted 17 August 2011

Keywords:

Human brain

Formalin fixation

Magnetic resonance imaging

Affine registration

Non-rigid registration

Deformation field

ABSTRACT

Before investigating human brains post mortem, the first preparation step is often formalin fixation of the brain. As the brain consists of inhomogeneous tissues, the fixation leads to a three-dimensional strain field within the tissue. During the single case MR-based investigation of the brain, first, the starting point with the brain post mortem but still within the cranium, was examined. Then 13 MR data sets were acquired over a fixation period of 70 days and compared to the initial data set. Based on affine registration of the data sets, the global volume shrinkage was found to be 8.1%. By means of a non-rigid registration additional maximal local volume strains of 32% were determined.

© 2011 Elsevier B.V. All rights reserved.

1. Introduction

The current developments in neurosurgical approaches, like magnetic resonance (MR)-guided neurosurgery with high-intensity focused ultrasound (e.g., Kennedy et al., 2003; Jolesz and McDannold, 2008; Martin et al., 2009) require a profound knowledge of the morphology of the human brain down to the micrometer level. Currently, neurosurgeons use detailed stereotactic atlases of human brain (Schaltenbrand and Wahren, 1977; Morel, 2007) to plan the treatment. The generation of such a brain atlas involves several steps. First, the brain tissue has to be fixated in order to avoid its degradation. In most cases formalin fixation is used. After sectioning the brain in few several dozen micrometer thin slices, it is stained using different protocols. The histological slices enable the distinction between different nuclei and the fibre system. Unfortunately, the different preparation steps cause local deformations of the brain tissue compared to the in vivo situation. Such deformations were already investigated by Germann et al. (2008), where two-dimensional histological slices were corrected by the related computed tomography (CT) slices and by Schulz et al. (2010), where the histological data was stacked to a three-dimensional (3D) data set and corrected by the 3D CT data set. The

present contribution examines the formalin fixation, namely the global shrinkage and related local deformations resulting from the inhomogeneity of the brain tissues.

The shrinkage of soft tissues during fixation results from several physico-chemical reactions (Burck, 1982; Romeis and Böck, 1989). The most important process is the fixation of proteins (see scheme in Fig. 1). The structure of native proteins is maintained by numerous chemical bonds like hydrogen, covalent, dative and hydrophobic bonds as well as electrostatic and Van der Waals forces. The classical way to cross-link proteins is by denaturation: bonds break and chemically active groups become available for cross-linking. Another procedure is the application of fixatives like formaldehyde where the cross-linking of the proteins takes place without the denaturation by formation of methylene bridges and Schiff bases (see scheme in Fig. 2).

Most examinations on shrinkage during formalin fixation were accomplished on tissues like liver and kidney (Wüstenfeld, 1955; Bloom and Friberg, 1956; Bahr et al., 1957) or on brain tissue of animals like rats (Leibnitz, 1967; Hillman and Deutsch, 1978) and dogs (Fox, 1965). Of course, it has to be disputed how far these studies can be compared with human brain tissue. Examinations of the human brain stem exist where the shrinkage is measured on the basis of 2D histological slices (Quester and Schröder, 1997). The present study however uses 3D magnetic resonance imaging (MRI) data sets of the whole brain post mortem. Data sets of the brain inside the skull, after extraction, and at different fixation times were investigated.

* Corresponding author. Tel.: +41 61 265 9618; fax: +41 61 265 9699.
E-mail address: georg.schulz@unibas.ch (G. Schulz).

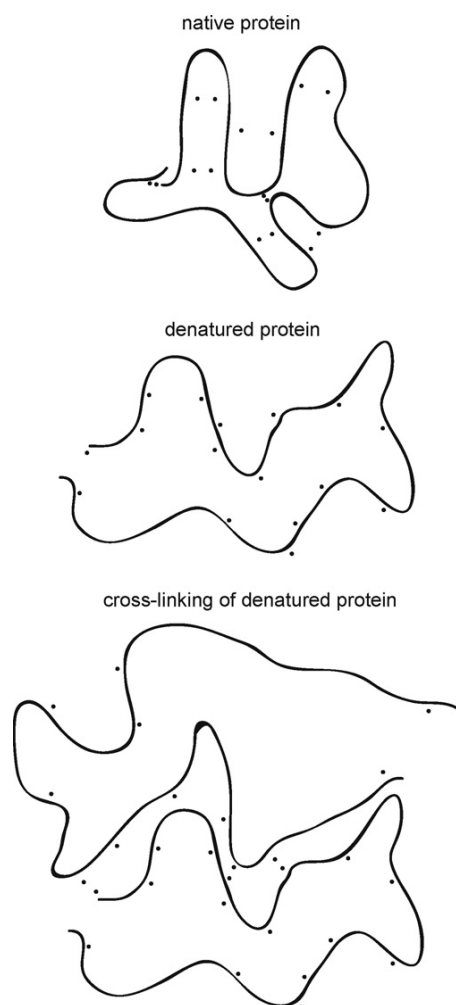


Fig. 1. Scheme of the cross-linking process of denatured proteins during fixation.

The evaluation of the deformations of the brain is based on 3D affine and non-rigid registration. This non-destructive technique allows examination of the influence of formalin on the brain tissue quantitatively. The usage of a 3D imaging technique combined with

non-rigid registration permits the extraction of the local deformations, which are relevant for the inhomogeneous brain tissue, and the separate examination of expansion and shrinkage of regions of interest inside the brain.

2. Materials and methods

For the measurements, a human brain of a 68 year old male with no neuropathological signs at autopsy was used. All procedures were conducted in accordance with the Declaration of Helsinki and according to the ethical guidelines of the Canton of Basel. After the first MRI scan of the intact head (within 48 h after death), the following steps of preparation were carried out. First, the scalp was detached and the calvaria removed through a horizontal cut. After the transection of the tentorium cerebelli and a cut through vasculature, nerves and the medulla, the brain was extracted and put into 10% formalin for fixation. The brain was then measured again after diverse formalin fixation degrees. During the measurements it was in a container filled with formalin. Here, the brain was sinking to the ground of the container, but because of similar density to the formalin solution the touching area was restricted to a very small interface with negligible influence on the brain's shape.

All MRI scans were performed on a Verio 3T whole body scanner (Siemens Health Care, Erlangen, Germany). MPRAGE acquisitions with 0.7 mm isotropic resolution and a field of view (FOV) of $268.0 \times 268.0 \times 179.2 \text{ mm}^3$ were performed with an 8° flip angle, 2000 ms repetition time, 2.72 ms echo time, and 700 ms inversion time. Twelve averages were taken in order to reach sufficient signal to noise ratio (SNR) within a total scan time of 154 min. The determined SNR of the data sets had a value of 200. Four of the data sets were scanned using MPRAGE acquisitions with 1.0 mm isotropic resolution, a FOV of $256.0 \times 256.0 \times 256.0 \text{ mm}^3$, an 8° flip angle, 2000 ms repetition time, 2.41 ms echo time and 700 ms inversion time. Taking four averages to reach identical SNR level, the total scan duration was 34 min.

For the determination of the volume changes of the brain one day after extraction and during formalin fixation a 3D affine registration algorithm was used (Fierz et al., 2008). The registrations were performed using the classical maximization of mutual information (MI) principle (Maes et al., 1996; Viola and Wells, 1995). In order to determine local deformations of the brain caused by extraction and formalin fixation, the related 3D data sets were registered by means of a non-rigid registration algorithm

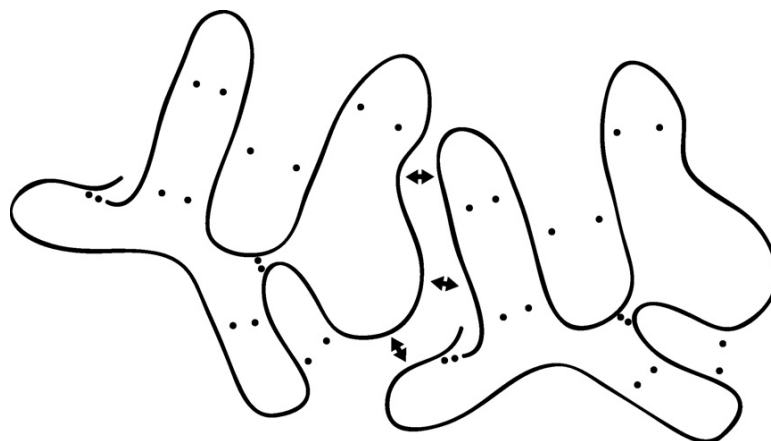


Fig. 2. Scheme of the cross-linking process of non-denatured or minimally denatured proteins during fixation using a fixative.

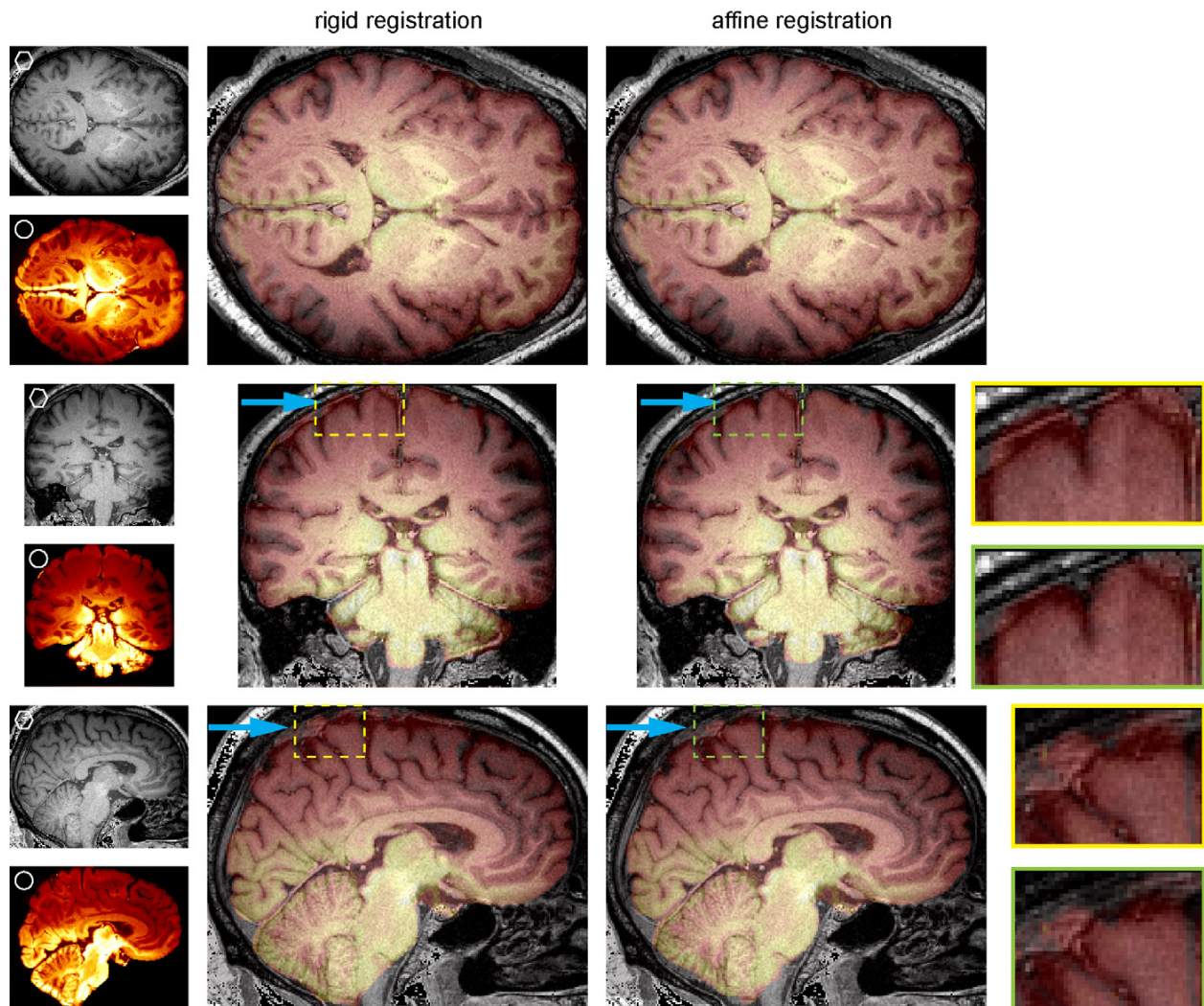


Fig. 3. Three-dimensional rigid and affine registration of the data sets of the brain inside the cranium (gray scale, hexagon) and one day after extraction (orange colored, circle). On the right side the images before and after registration are overlaid with the colored image being semi-transparent. The arrowheads demonstrate the deformations caused by extraction and one day of formalin fixation and the correction of them using affine registration. (For interpretation of the references to color in this figure legend, the reader is referred to the web version of the article.)

developed at Computer Vision Lab, ETH Zurich. The chosen registration algorithm is based on the adaptive hierarchical image subdivision strategy, which decomposes the non-rigid matching problem into numerous local affine registrations of sub-images of decreasing size (Andronache et al., 2008). The local registrations were again performed using the classical maximization of MI principle. The local registration parameters were found using the Powell multi-dimensional search algorithm (Press et al., 1988) such that the MI between the reference and the floating sub-images was maximized. The hierarchical image splitting strategy was proposed by Likar and Pernus (2001) and was recently extended to 3D with several improvements (Andronache et al., 2008). The hierarchical splitting was governed by a sub-image information consistency test in the form of the Moran spatial autocorrelation coefficient. At each level of the hierarchy, the consistency of the information contained in each of the further subdivided images was tested, and all those sub-images failing this test were no longer subdivided or registered at the successive levels. This consistency test was also used as the stopping criterion for the entire

registration algorithm. The hierarchical image subdivision was complete when no structural information was found in any of the currently partitioned sub-images, and therefore, their local registration was meaningless. As a consequence of the use of the information consistency test, at the last hierarchical level, the size of the sub-images may differ from one another. A typical minimum size is around $8 \times 8 \times 8$ voxels depending on the level of details and noise in the original image. The final deformation field was estimated from all registration parameters of all sub-images at the last hierarchical level by thin plate spline (TPS) interpolation. As the deformation field induced by formalin fixation has been unknown so far, it was impossible to provide a validation of the registration result for the particular case. The error bars were deduced using this registration method validated for the liver (Andronache, 2006). More precisely, using a MR scanner, T1 and T2 weighted images of the liver were acquired simultaneously at different stages of the respiratory cycle. The non-rigid registration was then used to recover the deformation fields, and the statistics led to an accuracy of 1.07 ± 0.75 in voxel dimensions.

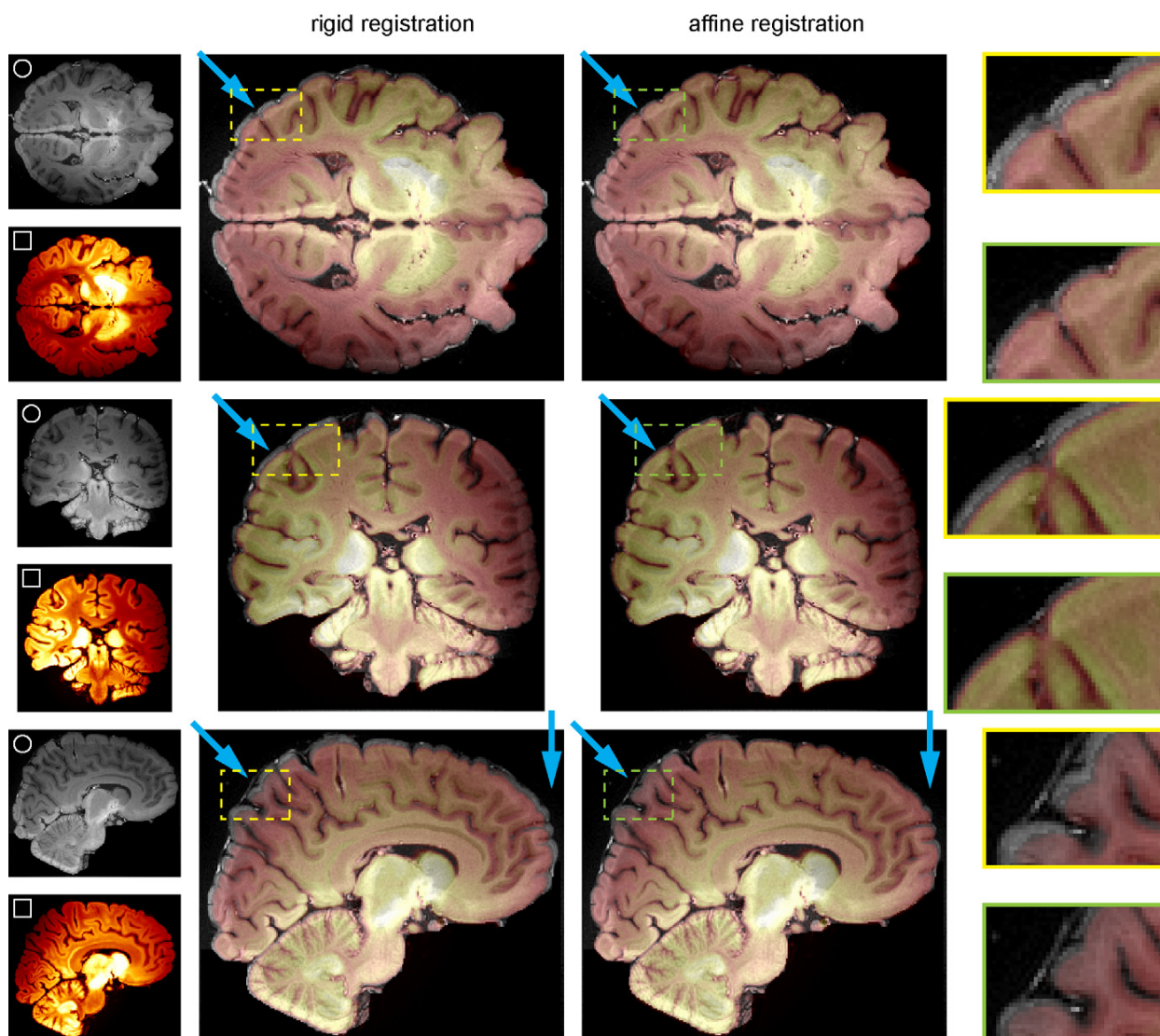


Fig. 4. Three-dimensional rigid and affine registration of the data sets of the brain one day after extraction (gray scale, circle) and after 70 days of formalin fixation (orange colored, square). Here, as well, the images before and after registration are overlaid with the colored image being semi-transparent. The arrowheads demonstrate the deformations arisen during formalin fixation and the correction of them using affine registration. (For interpretation of the references to color in this figure legend, the reader is referred to the web version of the article.)

3. Results

3.1. Global volume changes due to extraction and formalin fixation

Fig. 3 illustrates the deformations caused during the extraction and after one day of formalin fixation. For this purpose the MRI data set of the brain inside the cranium (hexagon) was registered with the data set one day after extraction (circle) using a rigid and affine registration algorithm. Having six degrees of freedom, i.e. three degrees of translation and three degrees of rotation, the two data sets were rigidly registered. Affine registration also includes scaling in the three orthogonal directions. The virtual cuts are given according to the data acquisition to avoid potential artifacts as the result of resampling. The data set scanned one day after extraction (colored orange) is matched to the data set before extraction and is made semi-transparent in order to indicate the differences.

Regarding the rigid registration, the blue arrowheads hint that the volume of the data set of the brain one day after extraction is larger than that of the data set inside the skull. After the affine registration, where additionally a scaling factor is used for the registration, the borders of the brain fit much better. The scaling factor of 1.052 ± 0.003 means an expansion of the brain of $5.2\% \pm 0.3\%$ resulting from extraction and one day of formalin fixation. Furthermore the registered data set of the brain one day after extraction was compared to the data sets at further steps of fixation. Fig. 4 shows the comparison of the brain one day after extraction (circle) with the one after 70 days of fixation (square). Here, the data set after 70 days of fixation is colored orange, made semi-transparent and laid over the data set one day after extraction. Again the arrowheads illustrate the differences between the data sets. The matching indicates that the volume of the data set after 70 days of fixation is smaller than that one day after extraction. This assumption can be proved by the affine registration of the data sets resulting in a

scaling factor of 0.934 ± 0.003 . The modification of the brain volume at different steps of formalin fixation can be seen in Fig. 5. During a fixation period of 70 days, nine scans with 0.7 mm isotropic voxel size (blue data sets) and four scans with 1.0 mm isotropic voxel size (orange data sets) were acquired. After the increase of the volume one day after extraction, a decrease of the volume can be observed during the fixation period. A fit using an exponential function provides the value for the volume shrinkage of the brain after infinite time of fixation. The fit parameter y_0 in Fig. 5 represents a total volume shrinkage value (compared to the volume inside the skull) of $96.7\% \pm 0.5\%$. This value contains both effects, namely the expansion during the first day after extraction and shrinkage during fixation. Consequently, the net shrinkage value during fixation without the effect of extraction and one day of formalin fixation is $91.9\% \pm 0.6\%$.

3.2. Local deformations caused by extraction and formalin fixation

After the affine registration, the data sets were registered using the non-rigid registration algorithm in order to determine additional local deformations inside the brain induced by extraction and formalin fixation. Figs. 6 and 7 compare the results of the affine and

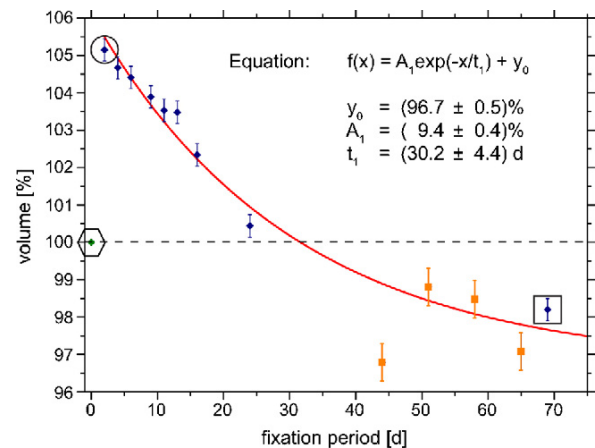


Fig. 5. Time-dependent progress of the whole brain volume one day after extraction and further formalin fixation. Highlighted are the moments of the brain inside the cranium (hexagon), one day after extraction (circle) and after 70 days of fixation (square) which are illustrated in Figs. 3 and 4. The blue data sets were acquired with an isotropic voxel size of 0.7 mm, the orange data sets with 1.0 mm. (For interpretation of the references to color in this figure legend, the reader is referred to the web version of the article.)

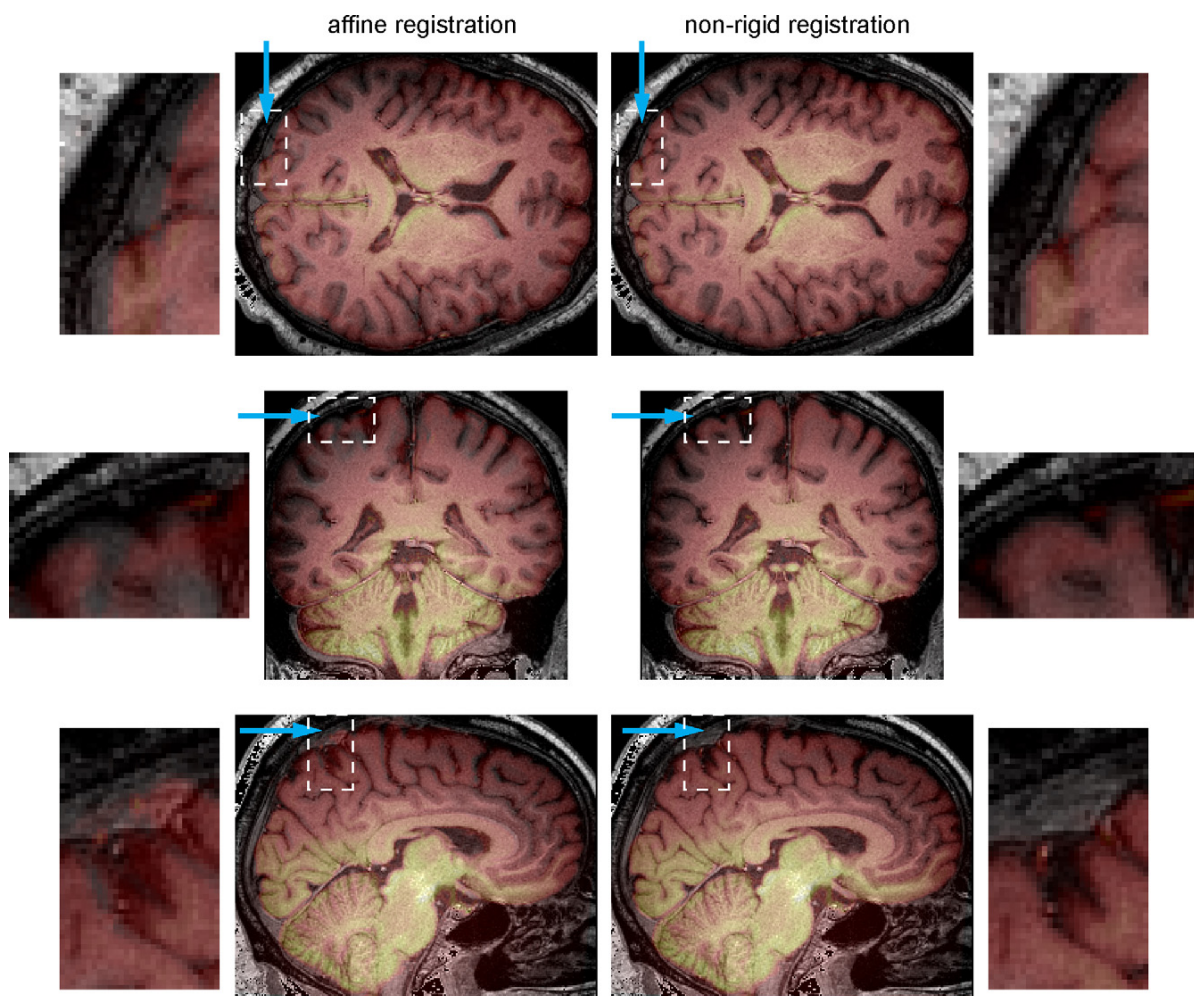


Fig. 6. Comparison between three-dimensional affine and non-rigid registration of the data set of the brain inside the cranium with the data set one day after extraction. The arrowheads illustrate the benefits of the non-rigid registration algorithm.

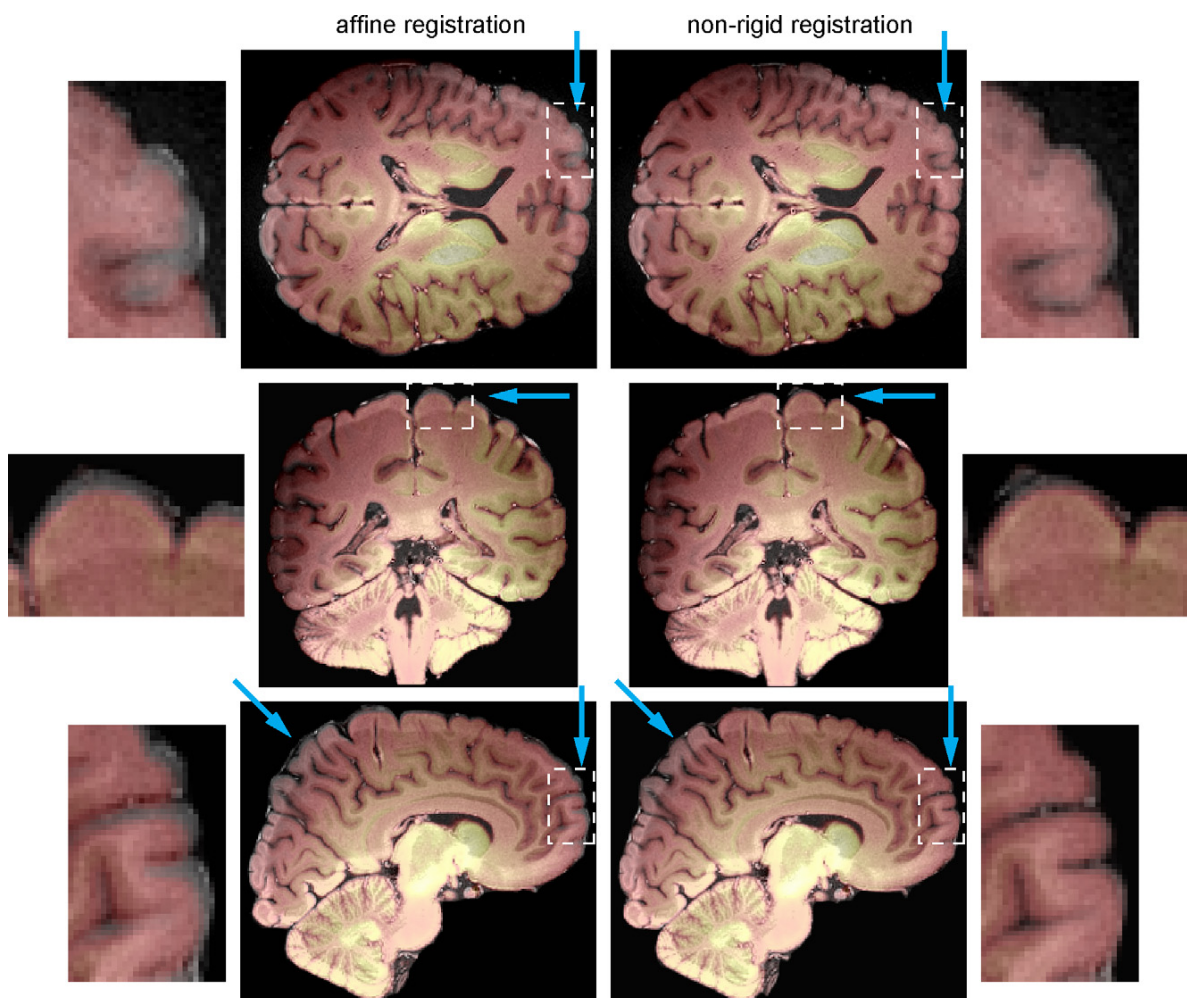


Fig. 7. Comparison between three-dimensional affine and non-rigid registration of the data set one day after extraction with that after 70 days of formalin fixation. The arrowheads illustrate the benefits of the non-rigid registration algorithm.

the non-rigid registration. The arrowheads indicate the differences of the registration results.

Performing the non-rigid registration, the individual voxels of the deformed data set are shifted to the related 3D positions of the initial data set of the intracranial state. The resulting 3D deformation vector field caused by the extraction and one day formalin fixation of the brain is illustrated in Fig. 8. First, the magnitude of the voxel displacement vectors is shown by means of three orthogonal slices on the left side of the figure. The average strain value, which is equal to the average magnitude value of the 3D displacement vectors, is 0.6 mm. The more interesting value is the maximal magnitude of the displacements which amounts to 3.7 mm. In order to demonstrate the orientations of the displacement vectors, a more detailed 2D vector field was shown for several interesting areas (insets at the right side of the figure). The mean absolute pixel displacements (arrow length) of the whole data set in x -, y - and z -direction amount to 0.34 mm, 0.25 mm and 0.30 mm. The maximal pixel displacements amount to 3.62 mm, 2.30 mm and 2.81 mm in the directions of the x -, y - and z -axis. The 3D deformation field induced by formalin fixation is shown in Fig. 9. Again the values of the averaged extension, amounting to 0.15 mm, 0.11 mm and 0.19 mm, and the maximal strains, amounting to 1.88 mm, 1.30 mm and 2.65 mm, were determined for x -, y - and z -direction. The

maximal magnitude of the displacement vector field due to formalin fixation amounts to 2.7 mm.

3.3. Determination of the local volume strain field

The deformation field shown in Section 3.2 corresponds to a voxel displacement field. In order to investigate differences in the shrinkage values of interested regions of the brain, a local volume strain field was determined.

Having the 3D displacement field \bar{D} , a 3D local strain field in x -direction $\bar{\epsilon}_x$ can be calculated by

$$\bar{\epsilon}_x = \bar{D}_x * \bar{k}_x, \quad (1)$$

the convolution of the x -coordinate of the displacement field \bar{D}_x with the 3D kernel

$$\bar{k}_x(:, 1, :) = \bar{k}_x(:, 2, :) = \bar{k}_x(:, 3, :) = \frac{1}{18 \cdot l_x} \begin{pmatrix} -1 & 0 & 1 \\ -1 & 0 & 1 \\ -1 & 0 & 1 \end{pmatrix}, \quad (2)$$

l_x being the voxel length of the data set in x -direction. Eq. (1) is a matrix which contains local shrinkage values (negative signs) and local expansion values (positive sign) of data set sub-volumes having the size of $3 \times 3 \times 3$ voxels. Values equal to zero represent

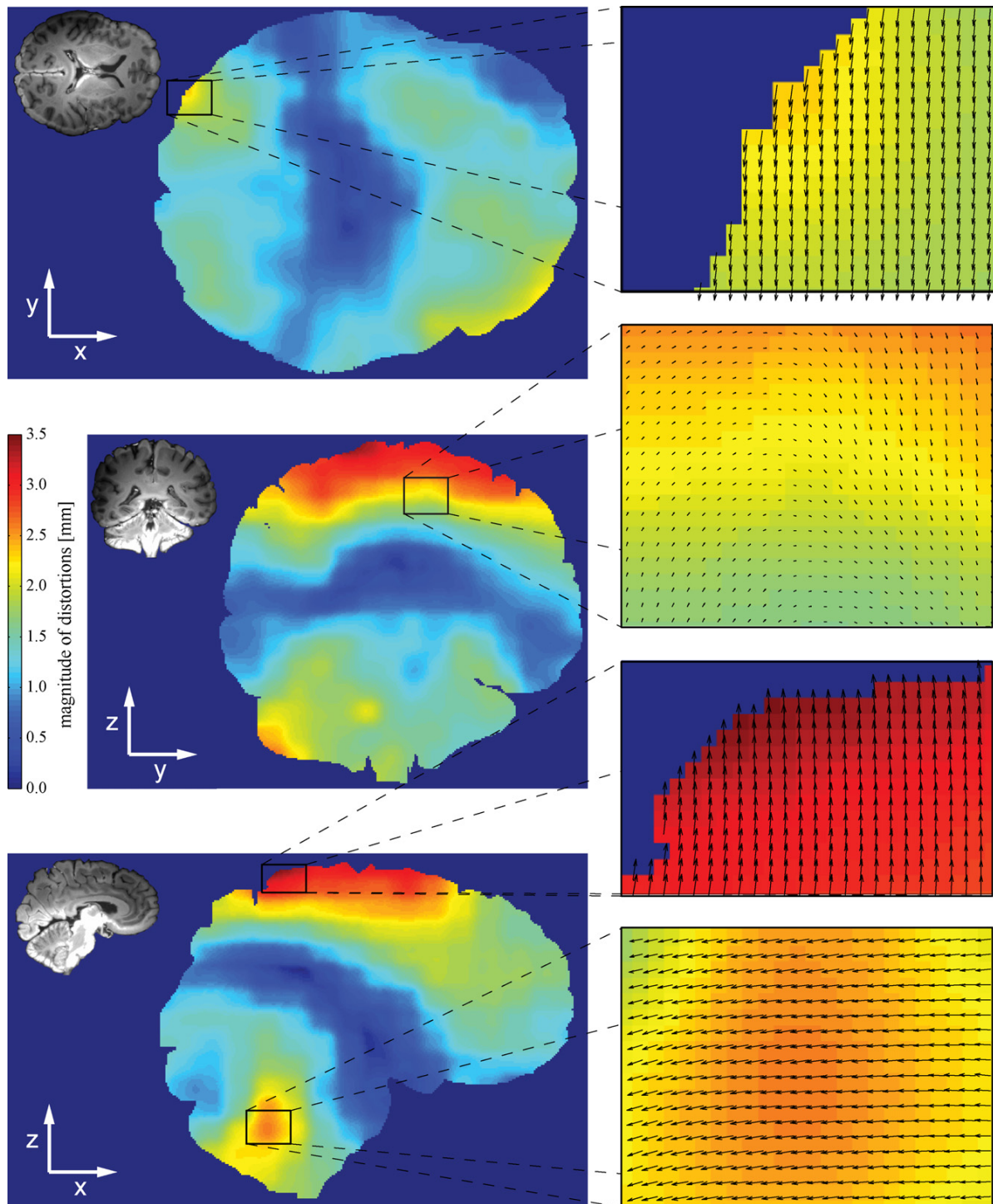


Fig. 8. Three-dimensional deformation vector field of the brain due to extraction and one day of formalin fixation, exemplary shown by means of the magnitude of the voxel displacement vectors for the three orthogonal slices. Zooms of selected regions illustrate the orientation of the vectors projected on the corresponding plane.

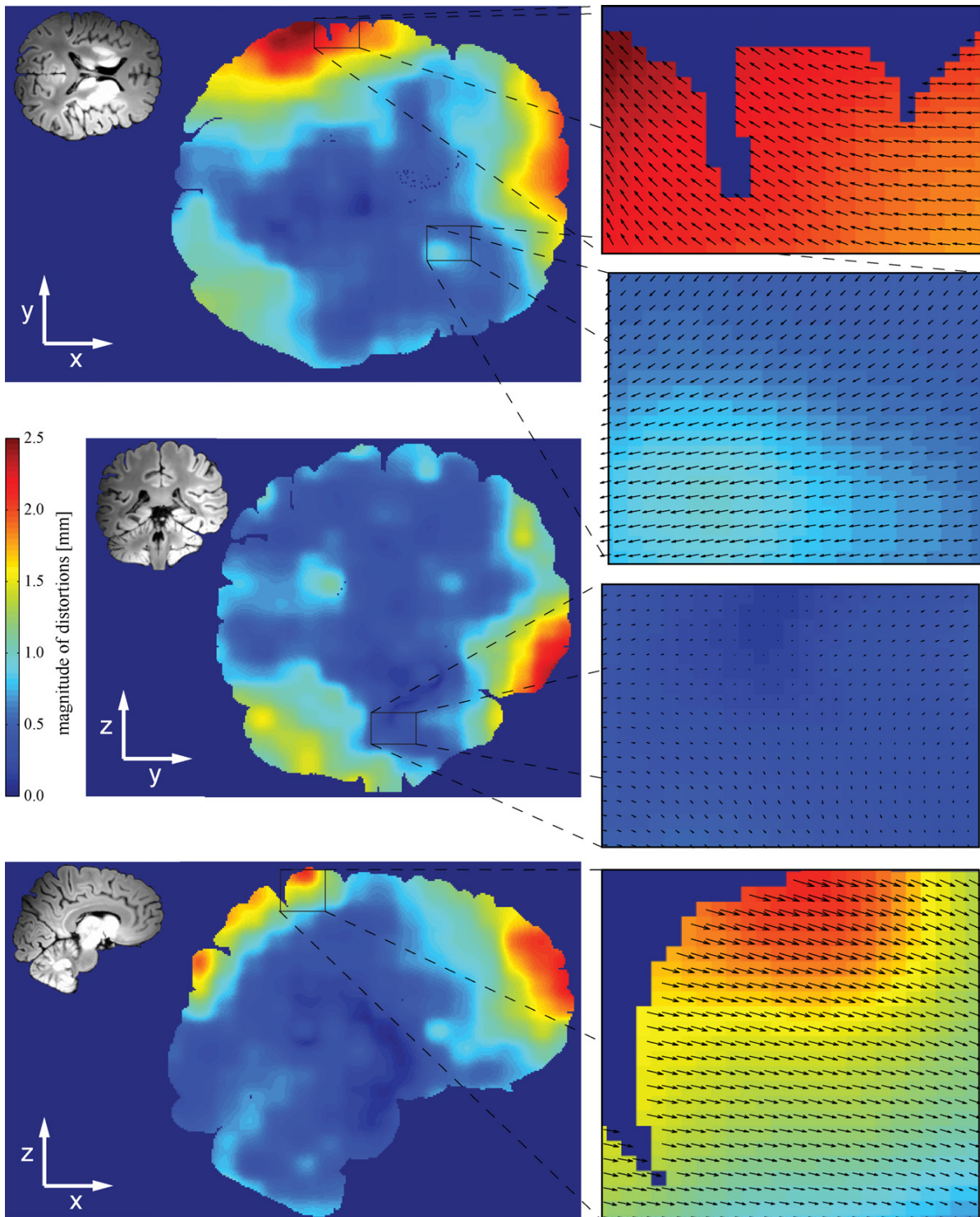


Fig. 9. Deformation vector field induced by formalin fixation shown by maps of the magnitude of the voxel displacement vectors and two-dimensional vector fields of selected regions which demonstrate the orientations of the deformations.

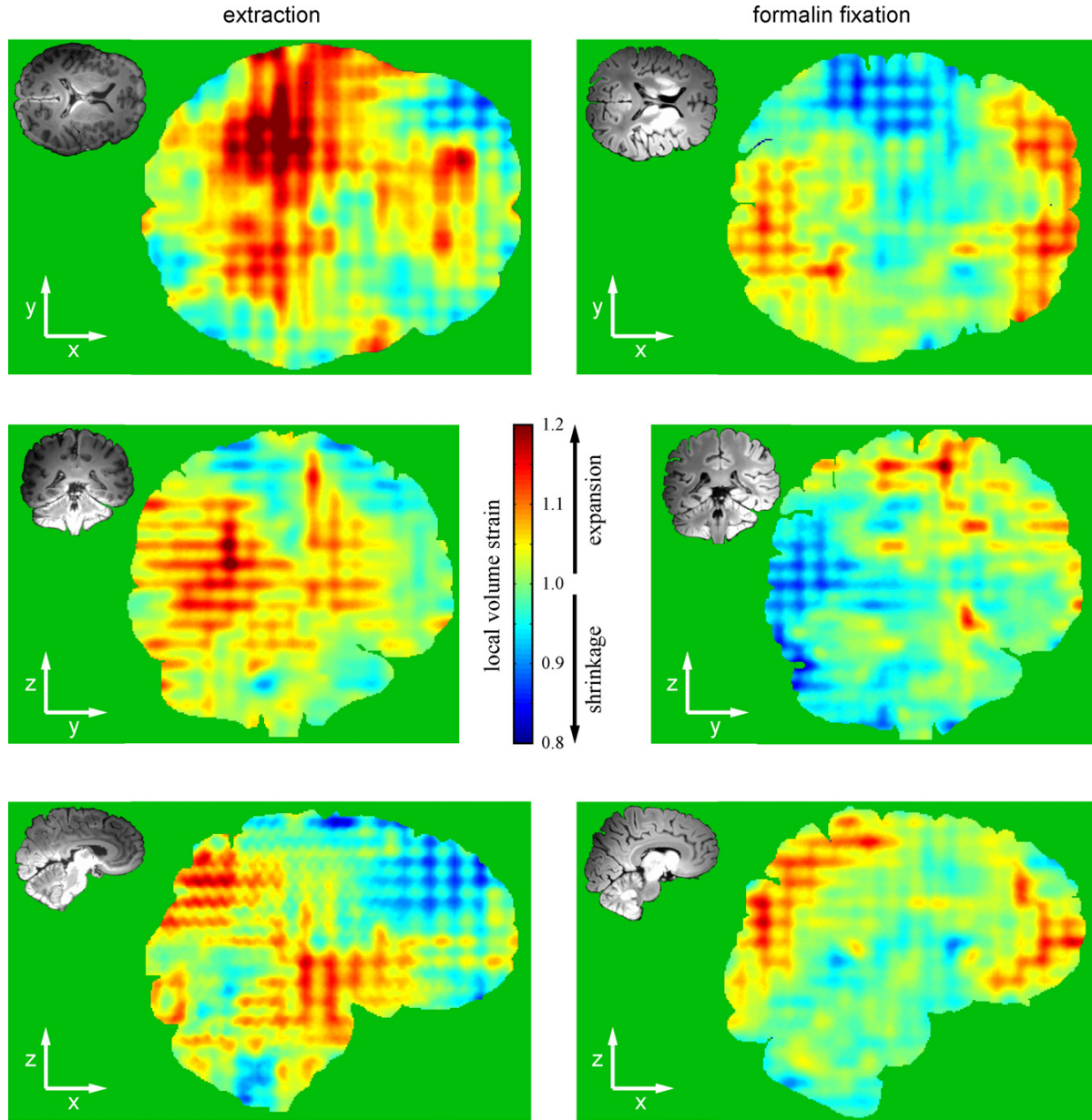


Fig. 10. Local volume strain field induced by extraction and formalin fixation shown by maps of the local scaling factors.

volumes with neither shrinkage nor expansion. An other way to define strains is the use of scaling factors. The scaling factors in x-direction can be determined by

$$\bar{S}_x = \bar{J} + \bar{\varepsilon}_x, \quad (3)$$

where \bar{J} is a matrix of ones having the same dimensions as $\bar{\varepsilon}_x$. Using the kernels

$$\bar{k}_y(:, :, 1) = \bar{k}_y(:, :, 2) = \bar{k}_y(:, :, 3) = \frac{1}{18 \cdot l_y} \begin{pmatrix} 1 & 1 & 1 \\ 0 & 0 & 0 \\ -1 & -1 & -1 \end{pmatrix} \quad (4)$$

and

$$\bar{k}_z(1, :, :) = \bar{k}_z(2, :, :) = \bar{k}_z(3, :, :) = \frac{1}{18 \cdot l_z} \begin{pmatrix} 1 & 1 & 1 \\ 0 & 0 & 0 \\ -1 & -1 & -1 \end{pmatrix}, \quad (5)$$

the local strains in y- and z-direction can then be determined by

$$\bar{S}_y = \bar{J} + \bar{D}_y * \bar{k}_y \quad \text{and} \quad \bar{S}_z = \bar{J} + \bar{D}_z * \bar{k}_z. \quad (6)$$

The determination of the local volume strains is a componentwise multiplication of the calculated scaling matrices

$$\bar{S}_{vol} = \bar{S}_x \cdot \bar{S}_y \cdot \bar{S}_z. \quad (7)$$

Fig. 10 demonstrates the local volume strain field induced by extraction plus one day of fixation and as a result of formalin fixation over a period of 70 days. The local strain field after one day after extraction has maximal volume strains of 1.32 and minimal values of 0.73. During the fixation period, maximal strains of 1.22 and minimal strains of 0.76 occurred. In order to affirm the global scaling factors determined by the affine registration in Section 3.1, the mean value of the local strains should amount to one being in

balance between shrinkage and expansion which is the case with the mean strain value of 1.008 for the data set one day after extraction and 1.001 for the data set after formalin fixation.

4. Discussion

Because of its high lateral spatial resolution, microscopy of histological sections is generally used for the characterization of brain tissue down to the cellular level. One of the first preparation steps is the formalin fixation of the whole brain after the extraction. Firstly, one expects a global volume change due to the extraction from the cranium and, inside the brain, local deformations caused by the handling procedure. Secondly, the fixation process should induce a shrinkage of the whole volume (Lang, 2006). Because of the inhomogeneity of the brain tissue, that can be explained by different chemical composition for instance of cerebral white and gray matter (Brooks et al., 1980), we also can expect a local strain field, which was not investigated until now. So far, the determination of the shrinkage of human brain during formalin fixation is based on the measurement of linear shrinkage values of brain slices (Mouritzen Dam, 1979; Quester and Schröder, 1997). During their study concerning Huntington's disease, Halliday et al. (1998) describe the determination of the volume shrinkage induced by formalin fixation measuring the volumes by fluid displacements. Unfortunately, using this technique, it is impossible to determine the volume changes induced by extraction of the brain or the local deformations due to the inhomogeneity of the brain tissue. Therefore, it is important to find a technique which enables us to determine the whole volume changes as well as the local strains in order to allow the correction of the artifacts induced by extraction and formalin fixation of the human brain.

MRI permits the non-destructive 3D visualization of the extracted human brain as well as inside the cranium and is known for its superb contrast between white and gray matter which makes registration between the data sets easy. The comparison of the data sets, intracranial and after extraction at different fixation steps can be arranged by means of an affine registration (for the determination of the volume change) and by means of a non-rigid registration (for the determination of the local strains). Rigid registration relates to solid states of identical size. Affine registration consequently belongs to the non-rigid approaches. Therefore, one might better term the non-rigid approach used in this study as elastic registration.

After the extraction of the brain and one day of formalin fixation, a volume expansion of the whole brain of $5.2\% \pm 0.3\%$ was determined. This first measurement after extraction is a superposition of the initial expansion related to extraction from cranium and the initiated early stages of fixation. The effect of expansion can be explained by lower pressure values outside the cranium and the swelling effect caused by osmotic pressure of the formalin solution (Hrdlicka, 1966; Blinkow and Glezer, 1968). Subsequently, the formalin treatment of the soft tissue induces brain shrinkage. The pure formalin fixation (without the effect caused after one day of extraction) of human brain tissue during a period of 70 days resulted in a volume shrinkage of $8.1\% \pm 0.6\%$. Mouritzen Dam (1979) indicates a volume shrinkage of gray matter of 33%. This value was determined by the measurement of slice thickness changes during formalin fixation with different concentrations and extrapolating the linear shrinkage value on the volume shrinkage. The assumption that the shrinkage of the different parts of the brain is isotropic is debatable, as shown by Quester and Schröder (1997). On the basis of an investigation of the formalin effect on human brain stem, they showed that the shrinkage is anisotropic, resulting in a shrinkage value of 8.3% along the longitudinal direction and almost no shrinkage along the transversal directions which results in a volume shrinkage of

around 8.3%. The volume shrinkage of the human brain stem is in the range of the value we obtained for the volume shrinkage of the whole brain. Values between 5% and 9% volume shrinkage during formalin fixation with concentration of 5–10% and pH values between 7.1 and 7.4 were determined by Burck (1982), measuring area changes of slices of different human soft tissues. These values also conform well with our result. The listed results are linear (Mouritzen Dam, 1979; Quester and Schröder, 1997) or area (Burck, 1982) measurements of specific parts of the brain which then are extrapolated to the volume shrinkage value. Furthermore, these techniques cannot reveal the effect of the brain extraction. The technique used here allows, besides the real 3D determination of the brain shrinkage during formalin fixation, the evaluation of the effect of extraction on the brain volume expansion. The two counteractive effects result in a net volume shrinkage of the brain of $3.3\% \pm 0.5\%$ compared to the post mortem situation of the brain inside the cranium.

The most important advantage of the technique is the possibility, not only to determine the global shrinkage of the brain, but also to analyse local shrinkage values and deformations of different parts of the brain. After MRI of the brain at the different steps of the investigation, one can determine volume shrinkage values using an affine and local strain field using a non-rigid registration. The calculated maximal local volume strain values of 32% and -27% due to extraction and one day of formalin fixation and 22% and -24% due to formalin fixation in addition to the whole volume changes cannot be disregarded. The maximal local strains have been found at different parts of the brain depending on the fixation time, Fig. 10). After extraction and one day of formalin fixation, the maximal expansion values were mainly located at the ventricles what can be seen on top left of the figure. The enlargement of the ventricles due to the lower pressure outside the cranium explains this behavior in a natural way. During the earlier stages of formalin fixation, the maximal strain values were found in the outer region of the brain to which the formalin could diffuse rather fast.

The non-rigid registration algorithm not only determines the changes but also corrects them and thereby generating a 3D data set which, despite underlying different preparation steps, correlates well with the data set of the brain post mortem inside the cranium, although having endured different preparation steps.

5. Conclusions

In order to determine the volume change of the whole human brain during extraction and formalin fixation, an affine registration algorithm was applied on MRI data sets at diverse steps of the study. Furthermore, the contribution demonstrated the power of 3D non-rigid registration in order to correct local artifacts produced during the extraction and the formalin fixation. This technique generates a morphological condition of the brain that is very close to the post mortem situation inside the skull. This data set can then be used for the correction of the high resolution data set (e.g., synchrotron radiation-based microcomputed tomography) of a smaller part like the thalamus and finally for the correction of the micrographs of the histological slices and consequently the correction of stereotactic atlases.

Acknowledgements

The authors gratefully acknowledge P. Zimmermann for the extraction and the fixation of the human brain, the Computer Vision Lab at the ETH Zurich (A. Andronache) for the availability of the registration tool and A. Morel for constructive advice in medical

questions. The study has been financially supported by the Swiss National Science Foundation (CR2312.125 406).

References

- Andronache A. Multi-modal non-rigid registration of volumetric medical images. Information Technology and Electrical Engineering, ETH, Zürich, Zürich No. 16601; 2006.
- Andronache A, von Siebenthal M, Székely G, Cattin P. Non-rigid registration of multi-modal images using both mutual information and cross-correlation. *Med Image Anal* 2008;12:3–15.
- Bahr GF, Bloom G, Friberg U. Volume changes of tissues in physiological fluids during fixation in osmium tetroxide or formaldehyde and during subsequent treatment. *Exp Cell Res* 1957;12:342–55.
- Blinkow SM, Glezer II. The human brain in figures and tables. New York: Plenum Press; 1968.
- Bloom G, Friberg U. Shrinkage during fixation and embedding of histological specimens. *Acta Morphol Neerl Scand* 1956;1:12–20.
- Brooks RA, Di Chiro G, Keller MR. Explanation of cerebral white-gray contrast in computed tomography. *J Comput Assist Tomogr* 1980;4:489–91.
- Burck HC. *Histologische Technik*. 5th ed. Stuttgart: Thieme; 1982.
- Fierz F, Beckmann F, Huser M, Irsen S, Leukers B, Witte F, et al. The morphology of anisotropic 3D-printed hydroxyapatite scaffolds. *Biomaterials* 2008;29:3799–806.
- Fox MW. Uptake of formalin by brain tissue from dogs killed at various stages of development. *Nature* 1965;205:1221.
- Germann M, Morel A, Beckmann F, Andronache A, Jeanmonod D, Müller B. Strain fields in histological slices of brain tissue determined by synchrotron radiation-based micro computed tomography. *J Neurosci Methods* 2008;170:149–55.
- Halliday GM, McRitchie DA, Macdonald V, Double KL, Trent RJ, McCusker E. Regional specificity of brain atrophy in Huntington's disease. *Exp Neurol* 1998;154:663–72.
- Hillman H, Deutsch K. Area changes in slices of rat-brain during preparation for histology or electron-microscopy. *J Microsc* 1978;114:77–84.
- Hrdlicka A. Brain and brain preservatives. *Proc US Nat Mus* 1966;30:245–320.
- Jolesz FA, McDannold NJ. Current status and future potential of MRI-guided focused ultrasound surgery. *J Magn Reson Imaging* 2008;27:391–9.
- Kennedy JE, ter Haar GR, Cranston DW. High intensity focused ultrasound: surgery of the future? *Br J Radiol* 2003;76:590–9.
- Lang G. *Histotechnik: Praxislehrbuch für die Biomedizinische Analytik*. Wien: Springer-Verlag; 2006.
- Leibnitz L. Die Veränderung von Gewicht, Volumen und spezifischem Gewicht des Rattengehirnes nach Fixierung, Dehydrierung und Aufhellung. *J Hirnforsch* 1967;9:97–104.
- Likar B, Pernus F. A hierarchical approach to elastic registration based on mutual information. *Image Vis Comput* 2001;19:33–44.
- Maes F, Collignon A, Vandermeulen D, Marchal G, Suetens P. Multi-modality image registration by maximization of mutual information. In: *Mathematical methods in biomedical image analysis*. IEEE; 1996. p. 14–22.
- Martin E, Jeanmonod D, Morel A, Zadicario E, Werner B. High intensity focused ultrasound for non-invasive functional neurosurgery. *Ann Neurol* 2009;66:858–61.
- Morel A. *Stereotactic atlas of the human thalamus and basal ganglia*. New York: Informa Healthcare USA, Inc; 2007.
- Mouritzen Dam A. Shrinkage of the brain during histological procedures with fixation in formaldehyde solutions of different concentrations. *J Hirnforsch* 1979;20:115–9.
- Press WH, Flannery BP, Teukolsky SA, Vetterling WT. *Numerical recipes in C – the art of scientific computing*. Cambridge University Press; 1988.
- Quester R, Schröder R. The shrinkage of the human brain stem during formalin fixation and embedding in paraffin. *J Neurosci Methods* 1997;75:81–9.
- Romeis B, Böck P. *Mikroskopische Technik*. 17th ed. München: Urban & Fischer; 1989.
- Schaltenbrand G, Wahren W. *Atlas for stereotaxy of the human brain*. Stuttgart: Thieme; 1977.
- Schulz G, Morel A, Imholz MS, Deyhle H, Weitkamp T, Zanette I, et al. Evaluating the microstructure of human brain tissues using synchrotron radiation-based micro computed tomography. *Proc SPIE* 2010;78040:78040F.
- Viola P, Wells WM. Alignment by maximization of mutual information. In: *Proceedings of the fifth international conference on computer vision*; 1995. p. 16–23.
- Wüstenfeld E. Experimental contribution to the problem of volume changes and penetration time in histological technic. I. Effect of five fixatives in the volume of the liver, kidney, spleen and muscle at room temperature. *Z Wiss Mikrosk* 1955;62:241–7.

2.2 Deformations resulting from histology

The strain field induced by sectioning and staining during histology can be corrected by means of a non-rigid registration of the stacked histological data set with X-ray phase contrast microtomography data acquired before histology.

Published in Proceedings of SPIE

Evaluating the microstructure of human brain tissues using synchrotron radiation-based micro computed tomography

Georg Schulz*^a, Anne Morel^b, Martha S. Imholz^a, Hans Deyhle^a, Timm Weitkamp^c, Irene Zanette^c, Franz Pfeiffer^d, Christian David^e, Magdalena Müller-Gerbl^f, and Bert Müller^a

^aBiomaterials Science Center, University of Basel, Basel, Switzerland;

^bCenter for Clinical Research, University Hospital Zurich, Zurich, Switzerland;

^cEuropean Synchrotron Radiation Facility (ESRF), Grenoble, France;

^dDepartment of Physics/Biophysics (E17), Technische Universität München, Garching, Germany;

^eLaboratory for Micro- and Nanotechnology, Paul Scherrer Institut, Villigen, Switzerland;

^fInstitute of Anatomy, University of Basel, Basel, Switzerland;

ABSTRACT

Minimally invasive deep brain neurosurgical interventions require a profound knowledge of the morphology of the human brain. Generic brain atlases are based on histology including multiple preparation steps during the sectioning and staining. In order to correct the distortions induced in the anisotropic, inhomogeneous soft matter and therefore improve the accuracy of brain atlases, a non-destructive 3D imaging technique with the required spatial and density resolution is of great significance. Micro computed tomography provides true micrometer resolution. The application to post mortem human brain, however, is questionable because the differences of the components concerning X-ray absorption are weak. Therefore, magnetic resonance tomography has become the method of choice for three-dimensional imaging of human brain. Because the spatial resolution of this method is limited, an alternative has to be found for the three-dimensional imaging of cellular microstructures within the brain. Therefore, the present study relies on the synchrotron radiation-based micro computed tomography in the recently developed grating-based phase contrast mode. Using data acquired at the beamline ID 19 (ESRF, Grenoble, France) we demonstrate that grating-based tomography yields premium images of human thalamus, which can be used for the correction of histological distortions by 3D non-rigid registration.

Keywords: X-ray phase contrast, X-ray grating interferometry, X-ray Talbot interferometry, human brain tissue, human thalamus, histology, stereotactic brain atlas

1. INTRODUCTION

The performance of minimally invasive interventions such as gamma knife or MR-guided focused ultrasound surgeries for the treatment of chronic neuropathic pain or movement disorders [1] requires a profound knowledge of the location of the target volume. So far, neurosurgeons use detailed stereotactic atlases of the human thalamus [2,3] for the orientation within the treated part. Such brain atlases are based on histological sectioning with thicknesses of several dozen micrometers. Micrographs on sub-micrometer level of the differently stained histological slices can then be obtained by optical microscopy.

For anisotropic and inhomogeneous soft matter like brain tissue, the multiple preparation steps during sectioning and staining induce local deformations, which are already quantified in two dimensions (2D) using synchrotron-radiation-based micro computed tomography in absorption contrast mode [4]. Here, the histological slices with a lateral spatial resolution better than a micrometer were non-rigidly registered with the less detailed tomography data. The relatively weak contrast in the X-ray tomography data was sufficient [5] to reasonably correct the histological slices and to demonstrate differences between staining protocols. Unfortunately, this study was restricted to corrections in 2D. Three-dimensional (3D), non-destructive techniques for the correction of these spatial distortions with a spatial resolution down to the micrometer level would give even more reliable results and, therefore, would contribute to a more precise generic atlas of the brain parts of interest.

*georg.schulz@unibas.ch; phone +41 61 265 9618; fax +41 61 265 9699; www.bmc.unibas.ch

Developments in X-Ray Tomography VII, edited by Stuart R. Stock, Proc. of SPIE Vol. 7804, 78040F · © 2010 SPIE · CCC code: 0277-786X/10/\$18 · doi: 10.1117/12.859273

Proc. of SPIE Vol. 7804 78040F-1

Magnetic resonance imaging (MRI) is a non-destructive 3D imaging technique with high contrast between white and gray matter. Unfortunately, the limited spatial resolution of around three magnitudes larger than that of the micrographs inhibits the evaluation of the deformation field. Synchrotron radiation-based micro computed tomography (SR μ CT) in absorption contrast provides the required spatial resolution. The contrast in the human rostral medulla oblongata was already weak, so that considerable doubt remains as to whether the density resolution in absorption contrast mode actually results in high-quality images of the human thalamus which represents a major challenge in X-ray tomography as it exhibits weak absorption contrast. On this account, the SR μ CT experiment was carried out in phase contrast mode which is based on the phase shifts of X-ray waves penetrating the specimen [6]. An overview of the operating modes of the main X-ray phase contrast approaches can be found in literature [7]. During the present study, the recently developed grating interferometry [8-11] was used for the evaluation of the 3D deformation tensor induced by sectioning and staining of the human thalamus and consequently for the correction of the histological slices.

2. MATERIALS AND METHODS

2.1 Preparation of the brain specimen

The specimen was extracted from a donated male body. All procedures were conducted in accordance with the Declaration of Helsinki and according to the ethical guidelines of the Canton of Basel. One day after natural death, the brain was extracted at the Institute of Anatomy (University of Basel, Switzerland) and subsequently transferred to 10% formalin solution for fixation. After two weeks of fixation, a block of the thalamus was obtained by guillotine section at the University Hospital Zurich [3], Switzerland and placed in a container filled with 4% formalin solution. The position of the thalamus within the brain is shown by the MR-derived image in Figure 1. The size of the thalamic block was about $3 \times 3 \times 3 \text{ cm}^3$.

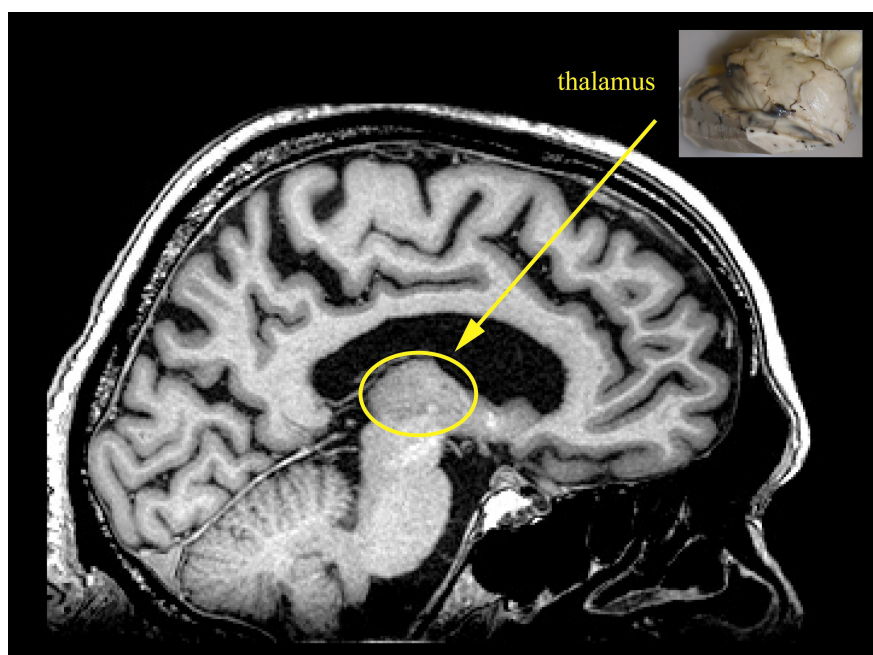


Figure 1. The MRI-slice of the investigated brain and the photography of the extracted thalamus (inset) indicate the location of the specimen inside the brain.

2.2 Grating interferometry

Phase contrast tomography provides information about the three-dimensional distribution of the real part of the refractive index of an object, often expressed in terms of its decrement from unity $\delta(x,y,z)$. Using the relation

$$\delta(x, y, z) = \frac{r_e \lambda^2}{2\pi} \rho_e(x, y, z), \quad (1)$$

where the constant r_e is the classical electron radius, it also yields the electron density distribution $\rho(x,y,z)$ for X-ray energies far away from the absorption edges. During our investigation a grating interferometer was used for detection of $\delta(x,y,z)$. Using the phase-stepping method, it is possible to detect slight deflections of the incoming X-rays caused by the phase object. The relation between local beam propagation direction $\alpha(y,z)$, wave phase shift $\Phi(y,z)$ and decrement of X-ray refractive index $\delta(x,y,z)$ is

$$\alpha(y,z) = \frac{\lambda}{2\pi} \frac{\partial \Phi(y,z)}{\partial y} = \int_{-\infty}^{\infty} \frac{\partial \delta(x,y,z)}{\partial y} dx. \quad (2)$$

A detailed description of grating interferometry and in particular of the phase-stepping method was published previously [10,12].

The grating interferometry experiment was performed at the beamline ID 19 (ESRF, Grenoble, France) [13]. The photon energy of 26 keV was selected using a double-crystal Si(111) monochromator in BRAGG geometry. The grating interferometer consists of a beam-splitter grating g_1 with a periodicity of $p_1 \approx 3.99 \mu\text{m}$ and a Si structure height of 34 μm , and the analyzer grating g_2 with a periodicity of $p_2 \approx 2 \mu\text{m}$ and a structure height of 25 μm . The beam-splitter and the analyzer grating were fabricated at the Paul Scherrer Institut (Villigen, Switzerland) [14]. With a distance between source and interferometer of 150 m and a distance between the gratings of $d \approx 376 \text{ mm}$ (9th Talbot order), the ratio of the grating periods, p_2/p_1 , was matched to the beam divergence [15].

The Eppendorf container with the thalamus in formalin solution was fixed at the high-precision rotation stage and immersed in a water tank with parallel polymethylmethacrylat plates for the measurements fixed during the whole experiment. This arrangement ensured minimized artifacts owing to X-ray phase curvature induced by the container surface. Specimen and tank were located about 10 cm upstream of the beam-splitter grating. The detector, placed about 3 cm downstream of the analyzer grating, was a lens-coupled scintillator and charge-coupled device (CCD) system using a FReLoN 2K (Fast-Readout, Low-Noise, ESRF Grenoble, France) CCD with 2048×2048 pixels. The effective pixel size corresponded to 31 μm . The field of view was 20.2 mm wide and 12.5 mm high. As the specimen width was larger than the field of view, one experiment was performed with an asymmetric axis position, shifted by 9 mm from the center of the detection unit as used previously [16]. In order to image the entire thalamus, four scans each at different height position of the specimen were acquired. During the second experiment, the axis position was shifted back to the centre of the detection unit and three scans at different height positions were acquired in order to image the inner part of the thalamus in local tomography mode. Projection radiographs were taken in 1200 steps over a range of 360° during the ‘off-axis’ experiment and 799 steps over a range of 360° during the conventional experiment where the axis position was at the centre of the detection unit. At each projection angle, four phase-stepping images were taken over one period of the interferometer fringe pattern. The exposure time for each image was set to a period of 1 s.

2.3 Histology

After the SR μ CT experiments, the block was transferred in progressively increasing sucrose concentrations over around two weeks for cryo-protection. The block was then frozen by immersion in isopentane ($\sim -30^\circ\text{C}$) and stored at -75°C . Using a Leica CM 3050, cryostat sections, 50 μm thick, were collected in 0.1 M phosphate buffer. For the staining procedure, the sections were mounted on gelatinized slides and stained for Nissl with cresyl violet or for myelin with a modified Heidenhain procedure [3]. The sections were then recorded (HP scanjet 7400c). Microphotographs of selected thalamic areas were taken using a Leica MZ16 microscope and DFC420-C digital camera.

2.4 Data treatment

After processing of the projections of the ‘off-axis’ scan, the missing part of each projection was added by the appropriate, 180° shifted projection multiplied by (-1). Both projection datasets were then reconstructed using a modified filter kernel (Hilbert transform) in combination with standard filtered back-projection algorithm [11,17,18].

In order to combine the global ‘off-axis’ with the local ‘non-off-axis’ volume, the datasets were registered using a three-dimensional rigid algorithm [19,20] with six degrees of freedom, namely three translation and three rotation degrees. The registration was performed using the classical maximization of mutual information (MI) principle [21,22].

The histological images were stacked to a 3D dataset by approximately correlating the orientations and positions of the slices. For the calculation of the deformation field the tomography and the histological 3D dataset were then registered

using a three-dimensional non-rigid classical maximization of MI algorithm [19]. All the data treatment steps, except the registration, were done with Matlab 7.8 (MathWorks, Natick, USA).

3. RESULTS AND DISCUSSION

Brain tissue provides quite weak X-ray attenuation contrast, which is necessary to distinguish between the grey and white matter or even between grey matter structures such as the nuclei in the thalamus. Therefore, one alternatively uses phase contrast imaging, which possesses much better contrast for soft tissues than absorption contrast.

3.1 Morphology of the human thalamus

The morphology of the thalamus can be investigated by using different staining procedures. Depending on the staining, certain intra- and extra- thalamic structures can be identified. The Haidenhain procedure, for example, shows location of myelinated fiber tracts (or white matter) which are responsible for fast transfer of the impulses. The right image of Figure 2 shows such a myelin-stained section through the posterior part of the human thalamus. The darkness of the color of the slice correlates with the concentration of the myelin. On the basis of this staining, one can differentiate at least between eleven different structures, most of them located outside the human thalamus. The structures belonging to the thalamus are the *reticular thalamic nucleus* (R), the *lateral* and *medial pulvinar* (PuL and PuM) and the *lateral* and *medial geniculate nucleus* (LGN and MGN). Structures belonging to the adjacent tissue are the *putamen* (PuT), the *internal capsule* (ic), the *medial lemniscus* (ml), the *superior colliculus* (SC), the *comissure of the SC* (csc), as well as the *periaqueductal grey area* (PAG).

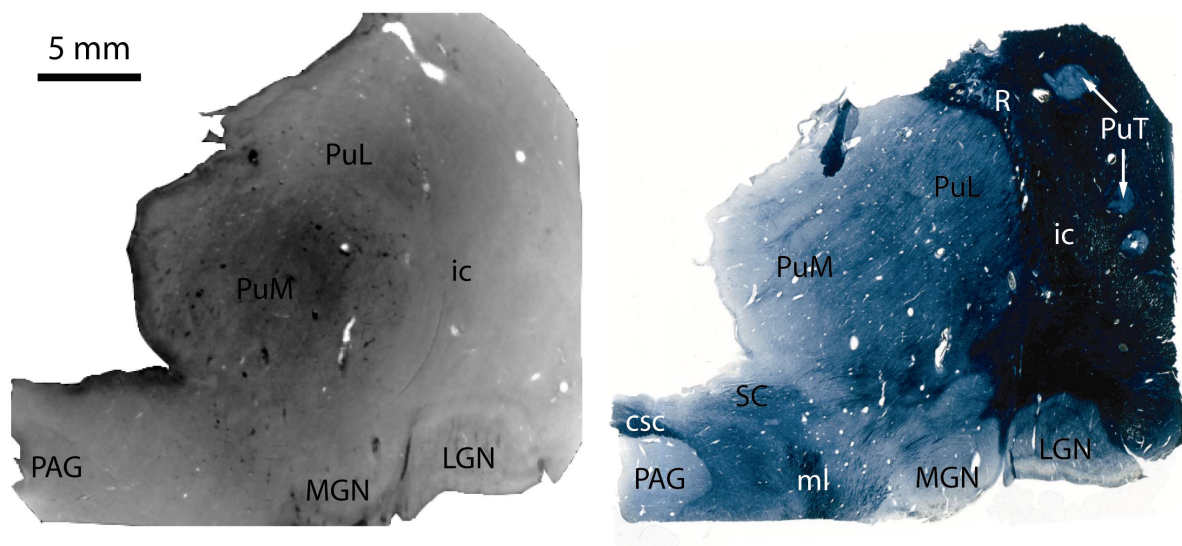


Figure 2. One grating-based SR μ CT-slice and the corresponding frontal myelin-stained histological slice. The blue-colored regions correspond to fiber tracts, which contain myelin. A comparison between the tomography and histology data points out, that besides all the blood vessels more than the half of the structures visible on the histological slice can also be identified in the corresponding tomogram.

Another procedure, the Nissl-staining using cresyl violet, allows differentiation of grey nuclei on the basis of cyto-architectonic characteristics in terms of cell sizes and densities. Such Nissl-stained sections of the thalamus are shown on the right hand side of Figure 3. The two sections are located around 1.4 and 0.8 (upper and lower right) cm anterior to the level shown in Figure 2. During this procedure, the cells adopt a blue color as seen in the zoom in of Figure 3. There, the blue-colored structures correspond to individual cells. Therefore, on these low-power images, the intensity of the blue color is mostly related to the cell density. Besides the structures visible in Figure 2, additional nuclei or fiber tracts can be identified at these more anterior levels: the *anteroventral nucleus* (AV), the *mediodorsal nucleus* (MD), the *ventral lateral nucleus* (VL), the *ventral anterior nucleus* (VA), the *zona incerta* (ZI), the *subthalamic nucleus* (STh), the *globus pallidus, internal* (GPi) and *external* (GPe) segments, the *optic tract* (ot), the *lateral dorsal nucleus* (LD), the *stria*

medullaris (sm), the *central lateral nucleus* (CL), the *centromedian nucleus* (CM), the *parafascicular nucleus* (Pf), the *red nucleus* (RN), the *fasciculus cerebello-thalamicus* (fct) and the *ventral posterior lateral nucleus* (VPL).

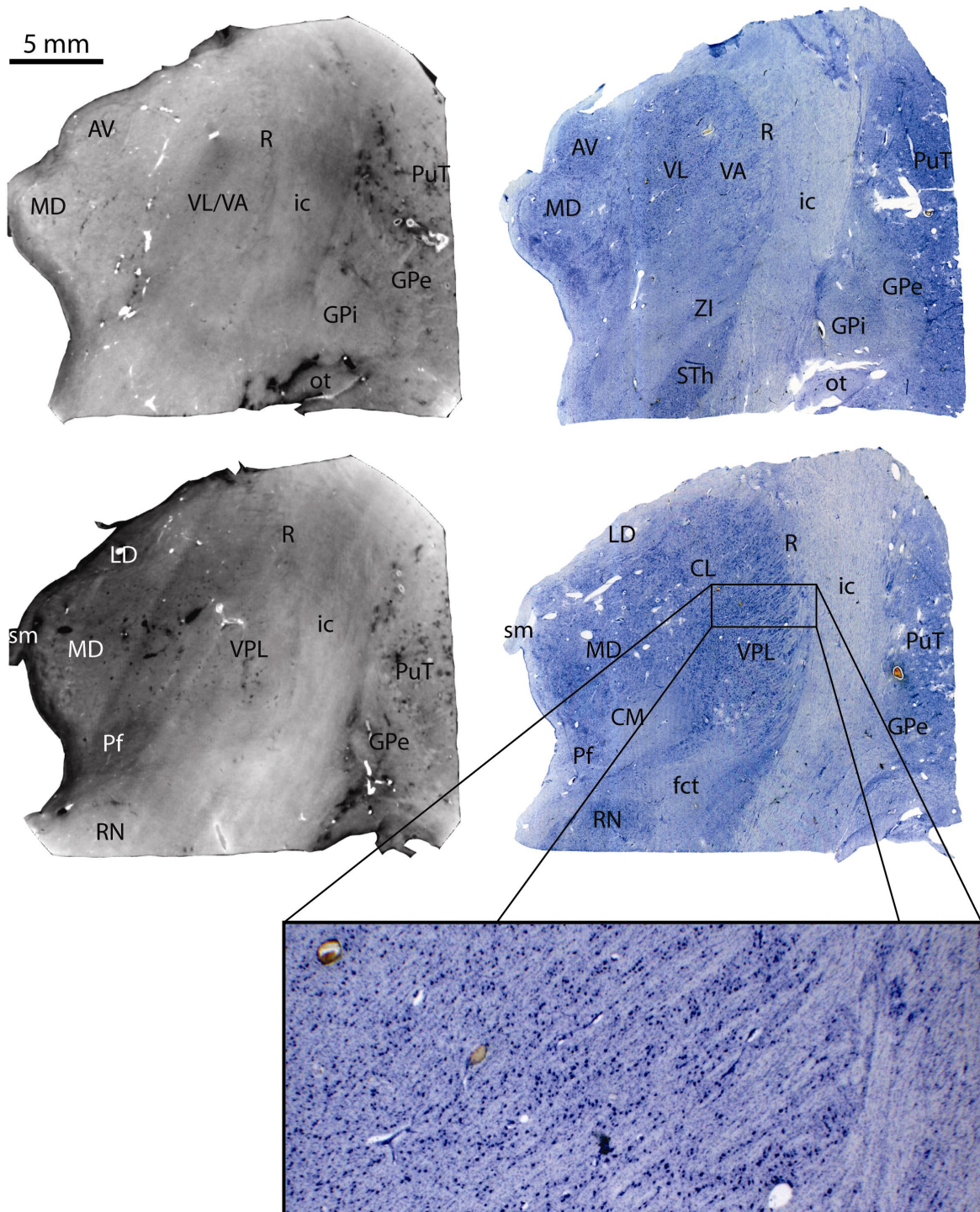


Figure 3. A comparison between the phase contrast and Nissl stained slices shows that also here most of the structures seen in the histology can be identified in the tomograms. With the Nissl, the cells are stained in blue as can be seen in the inset at higher magnification.

As already mentioned, the disadvantages of the histology are the multiple preparation steps which make this technique time consuming and which induce unknown changes in the anisotropic and inhomogeneous tissues like it is the case for brain tissue. According to the selected histological slices, tomograms of the grating-based phase contrast results can be seen on the left hand side of the Figures 2 and 3. With the aid of the histological slices many of the structures can be identified in the phase contrast results. The benefit of this non-destructive imaging technique is that the form and position of the structures are not modified. Another advantage of the tomography results is the isotropic pixel size. For this reason the spatial resolution in the horizontal and sagittal direction of the thalamus illustrated in Figure 4 is even better than that of the present histological data set. Of course, the results of histological sections in the horizontal or sagittal plane would again be better than the tomograms. However, histology results in high quality outcome in only two dimensions. The spatial resolution of the third dimension is always a few magnitudes larger than that of the other two dimensions. Here, the structures can even be better identified than on the frontal tomograms. Besides the already specified structures one can distinguish the *mammillothalamic tract* (mtt), the *fornix* (fx), *posterior commissure* (pc), the *suprageniculate nucleus / posterior nucleus complex* (SG/Po), the *superior colliculus* (SC), the *habenular nucleus* (Hb), the *caudate nucleus* (Cd) and the *fasciculus thalamicus* (ft).

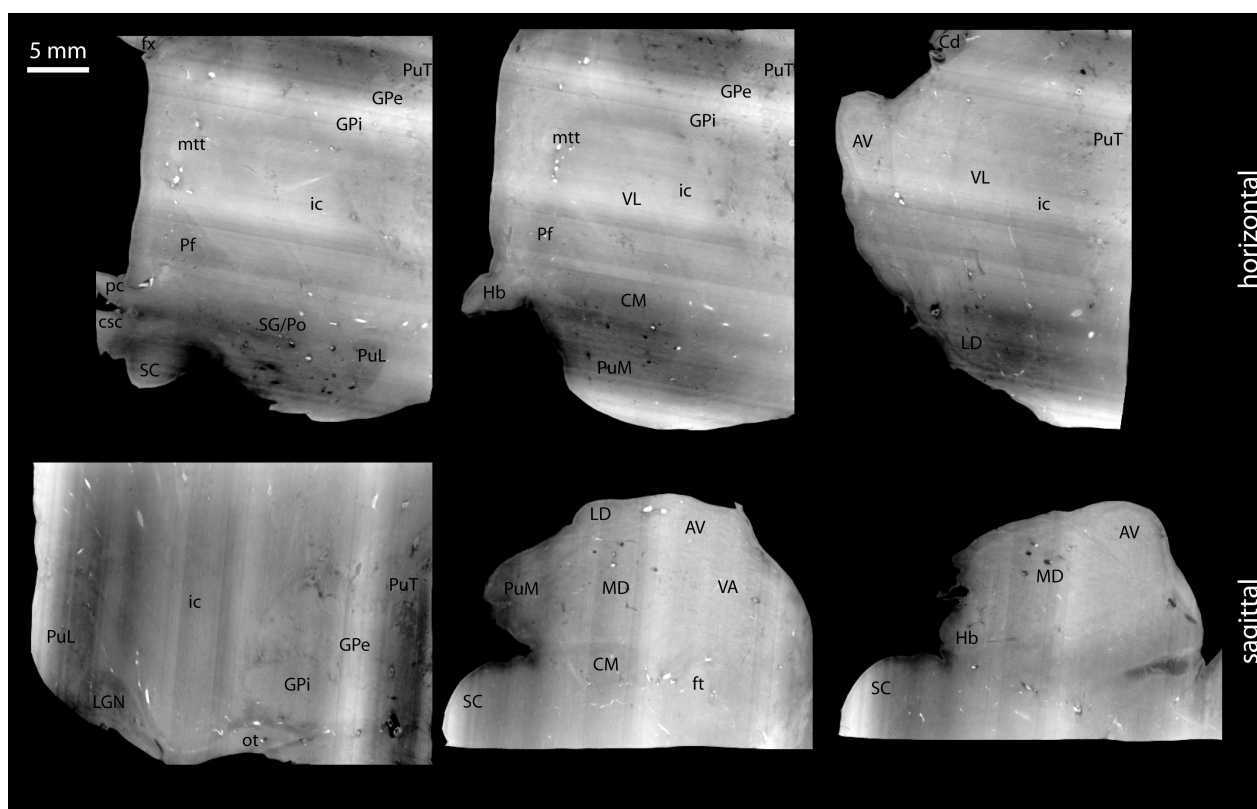


Figure 4. The horizontal and sagittal views of the grating interferometry even more illustrate the possibility to differentiate between different structures inside and outside the thalamus.

3.2 Internal strain field induced by sectioning and Nissl staining

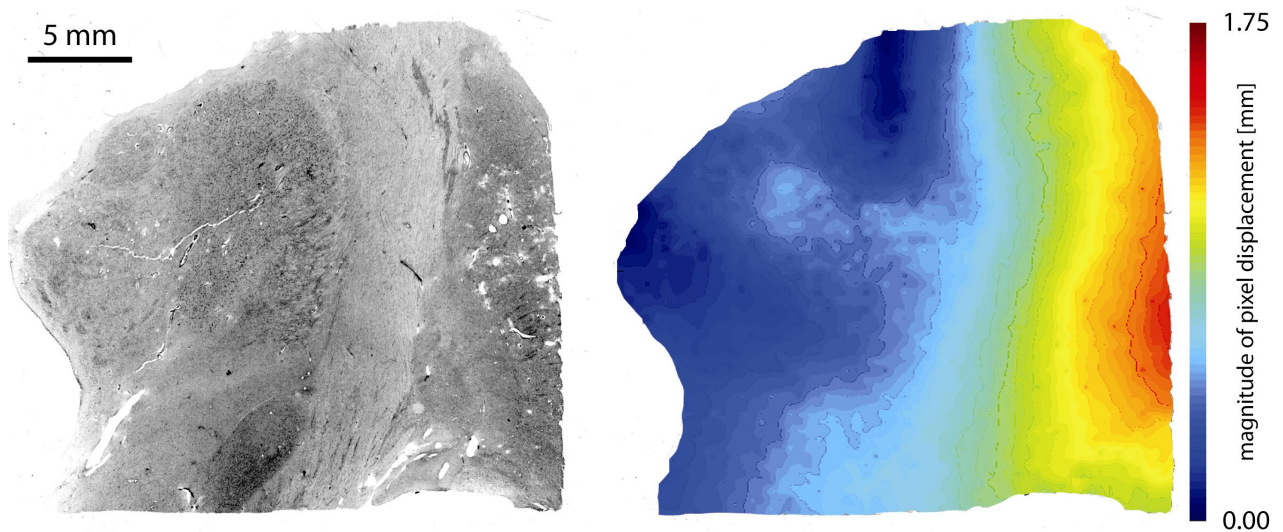


Figure 5. One Nissl-stained histological slice converted to gray scale for the non-rigid registration. The right image shows the corresponding magnitude of the deformation field caused by sectioning and staining.

For the determination of the deformation field, the Nissl-stained sections converted to gray scale were non-rigidly registered. Figure 5 shows one selected slice and the corresponding contribution of the magnitude of the pixel displacements caused during the histological preparation steps. The maximal displacement of this slice amounts to 1.75 mm what corresponds to 5 % of the slice extension. These maximal strain values are found mainly outside the thalamus, at the level of the *putamen* and the *globus pallidus*, most probably to due to large number of blood vessels in this area. The magnitude of the displacements of the internal capsule is around 0.8 mm whereas the strains inside the thalamus are smaller than that value.

4. CONCLUSIONS

Grating-based phase contrast SR μ CT is eminently suited for the imaging of human brain tissue with micrometer resolution. The high-quality images of the human thalamus can be used to determine the 3D deformation vector field, which is induced by sectioning and staining during histology and to improve the histological data. Therewith, the corrected histological slices with sub-micrometer resolution should improve the accuracy of stereotactic brain atlases, which can be used for non-invasive MR-guided neurosurgery without intra-cerebral penetration such as with gamma knife or high-intensity focused ultrasounds.

ACKNOWLEDGEMENTS

The authors gratefully acknowledge P. Zimmermann (Basel) for the extraction of the human brain, K. Scheffler and H. Crooijmans (Basel) for the MRI measurements of the brain and A. Andronache (Zurich) for availability of the non-rigid registration tool. The project was partially funded by Swiss National Science Foundation (CR2312_125 406) and was supported by beam time from the ESRF (proposal MD-328).

REFERENCES

- [1] Martin, E., Jeanmonod, D., Morel, A., Zadicario, E. and Werner, B., "High-Intensity Focused Ultrasound for Noninvasive Functional Neurosurgery," *Ann. Neurol.* 66, 858-861 (2009).
- [2] Schaltenbrand, G. and Wahren, W., [Atlas for Stereotaxy of the Human Brain], Thieme, Stuttgart, (1977).
- [3] Morel, A., [Stereotactic atlas of the human thalamus and basal ganglia], Informa Healthcare, New York, (2007).
- [4] Germann, M., Morel, A., Beckmann, F., Andronache, A., Jeanmonod, D. and Müller, B., "Strain fields in histological slices of brain tissue determined by synchrotron radiation-based micro computed tomography," *J. Neurosci. Methods* 170(1), 149-155 (2008).
- [5] Brooks, R.A., Di Chiro, G. and Keller, M.R., "Explanation of Cerebral White - Gray Contrast in Computed Tomography," *J. Comput. Assist. Tomogr.* 4(4), 489-491 (1980).
- [6] Fitzgerald, R., "Phase-Sensitive X-Ray Imaging," *Phys. Tod.* 53(7), 23-26 (2000).
- [7] Schulz, G., Weitkamp, T., Zanette, I., Pfeiffer, F., Beckmann, F., David, C., Rutishauser, S., Reznikova, E. and Müller, B., "High-resolution tomographic imaging of a human cerebellum: comparison of absorption and grating-based phase contrast," *J. R. Soc. Interface*, in press (2010).
- [8] David, C., Nöhammer, B., Solak, H.H. and Ziegler, E., "Differential x-ray phase contrast imaging using a shearing interferometer," *Appl. Phys. Lett.* 81, 3287-3289 (2002).
- [9] Momose, A., Kawamoto, S., Koyama, I., Hamaishi, Y., Takai, K. and Suzuki, Y., "Demonstration of X-Ray Talbot interferometry," *Jpn. J. Appl. Phys., Part 2* 42(7B), 866-868 (2003).
- [10] Weitkamp, T., Diaz, A., David, C., Pfeiffer, F., Stampanoni, M., Cloetens, P. and Ziegler, E., "X-ray phase imaging with a grating interferometer," *Opt. Express* 13(16), 6296-6304 (2005).
- [11] Pfeiffer, F., Kottler, C., Bunk, O. and David, C., "Hard X-ray phase tomography with low-brilliance sources," *Phys. Rev. Lett.* 98(10), 108105 (2007).
- [12] Pfeiffer, F., Grünzweig, C., Bunk, O., Frei, G., Lehmann, E. and David, C., "Neutron phase imaging and tomography," *Phys. Rev. Lett.* 96(21), 215505-1 - 215505-4 (2006).
- [13] Weitkamp, T., Tafforeau, P., Boller, E., Cloetens, P., Valade, J.-P., Bernard, P., Peyrin, F., Ludwig, W., Helfen, L. and Baruchel, J., "Status and evolution of the ESRF beamline ID19," *AIP Conf. Proc.* 1221, 33-38 (2010).
- [14] David, C., Bruder, J., Rohbeck, T., Grünzweig, C., Kottler, C., Diaz, A., Bunk, O. and Pfeiffer, F., "Fabrication of diffraction gratings for hard X-ray phase contrast imaging," *Microel. Eng.* 84, 1172-1177 (2007).
- [15] Weitkamp, T., David, C., Kottler, C., Bunk, O. and Pfeiffer, F., "Tomography with grating interferometers at low-brilliance sources" *Proc. SPIE* 6318, 63180S (2006).
- [16] Müller, B., Bernhardt, R., Weitkamp, T., Beckmann, F., Brauere, R., Schurigt, U., Schrott-Fischer, A., Glueckert, R., Ney, M., Beleites, T., Jolly, C. and Schamweber, D., "Morphology of bony tissues and implants uncovered by high-resolution tomographic imaging," *Int. J. Mater. Res.* 98(7), 613-621 (2007).
- [17] Faris, G.W. and Byer, R.L., "Three-dimensional beam-deflection optical tomography of a supersonic jet," *Appl. Opt.* 27, 5202-5212 (1988).
- [18] Pfeiffer, F., Bunk, O., Kottler, C. and David, C., "Tomographic reconstruction of three-dimensional objects from hard X-ray differential phase contrast projection images," *Nucl. Instrum. Methods Phys. Res.* 580(2), 925-928 (2007).
- [19] Andronache, A., von Siebenthal, M., Székely, G. and Cattin, P., "Non-rigid registration of multi-modal images using both mutual information and cross-correlation," *Med. Image Anal.* 12(1), 3-15 (2008).
- [20] Fierz, F.C., Beckmann, F., Huser, M., Irsen, S.H., Leukers, B., Witte, F., Degistirici, Ö., Andronache, A., Thie, M. and Müller, B., "The morphology of anisotropic 3D-printed hydroxyapatite scaffolds," *Biomaterials* 29(28), 3799-3806 (2008).
- [21] Viola, P. and Wells, W.M. "Alignment by maximization of mutual information," *Proc. 5th Int. Conf. on Comp. Vis.* 16-23 (1995).
- [22] Maes, F., Collignon, A., Vandermeulen, D., Marchal, G. and Suetens, P. "Multi-modality image registration by maximization of mutual information," *Proc. IEEE Math. Meth. in Biomed. Im. Anal.* 14-22 (1996).

2.3 Grating-based phase contrast X-ray SR μ CT of the human cerebellum

Phase contrast tomography was used for the visualization of the human cerebellum, where, besides structures like white matter, stratum granulosum, stratum moleculare and differently sized blood vessels, individual Purkinje cells surrounded by soft tissue could be identified.

Published in Journal of the Royal Society Interface

High-resolution tomographic imaging of a human cerebellum: comparison of absorption and grating-based phase contrast

Georg Schulz^{1,*}, Timm Weitkamp², Irene Zanette², Franz Pfeiffer³, Felix Beckmann⁴, Christian David⁵, Simon Rutishauser⁵, Elena Reznikova⁶ and Bert Müller¹

¹*Biomaterials Science Center, University of Basel, Basel, Switzerland*

²*European Synchrotron Radiation Facility, Grenoble, France*

³*Department of Physics/Biophysics (E17), Technische Universität München, Garching, Germany*

⁴*Institute for Materials Research, GKSS Research Centre, Geesthacht, Germany*

⁵*Laboratory for Micro- and Nanotechnology, Paul Scherrer Institut, Villigen, Switzerland*

⁶*Institute of Microstructure Technology, Karlsruhe Institute for Technology, Karlsruhe, Germany*

Human brain tissue belongs to the most impressive and delicate three-dimensional structures in nature. Its outstanding functional importance in the organism implies a strong need for brain imaging modalities. Although magnetic resonance imaging provides deep insights, its spatial resolution is insufficient to study the structure on the level of individual cells. Therefore, our knowledge of brain microstructure currently relies on two-dimensional techniques, optical and electron microscopy, which generally require severe preparation procedures including sectioning and staining. X-ray absorption microtomography yields the necessary spatial resolution, but since the composition of the different types of brain tissue is similar, the images show only marginal contrast. An alternative to absorption could be X-ray phase contrast, which is known for much better discrimination of soft tissues but requires more intricate machinery. In the present communication, we report an evaluation of the recently developed X-ray grating interferometry technique, applied to obtain phase-contrast as well as absorption-contrast synchrotron radiation-based microtomography of human cerebellum. The results are quantitatively compared with synchrotron radiation-based microtomography in optimized absorption-contrast mode. It is demonstrated that grating interferometry allows identifying besides the blood vessels, the stratum moleculare, the stratum granulosum and the white matter. Along the periphery of the stratum granulosum, we have detected microstructures about 40 μm in diameter, which we associate with the Purkinje cells because of their location, size, shape and density. The detection of individual Purkinje cells without the application of any stain or contrast agent is unique in the field of computed tomography and sets new standards in non-destructive three-dimensional imaging.

Keywords: synchrotron radiation-based microtomography; absorption contrast; X-ray phase contrast; X-ray grating interferometry; X-ray Talbot interferometry; human brain tissue

1. INTRODUCTION

With more than 50 billion neurons, most of them located in the cerebellar cortex, the human cerebellum includes around 50 per cent of the neurons of the entire brain (Trepel 2008). *Purkinje* cells are the largest cells of the cerebellum exhibiting spherical shapes with diameters of about 40–70 μm . These cells form the

nerve centre where the impulses of almost all neurons of the cerebellar cortex converge and are transferred to their destination beyond the cortex. Today, only two-dimensional methods, such as conventional histology and fluorescence microscopy, serve for Purkinje cell visualization. They include serious preparation steps, namely sectioning and staining. Sectioning destroys the three-dimensional nature of the brain specimens and the subsequent preparation steps induce local shrinkage, which requires correction of

*Author for correspondence (georg.schulz@unibas.ch).

the images (Germann *et al.* 2008). Therefore, non-destructive three-dimensional imaging techniques should be identified that provide enough contrast between internal features of the human cerebellum and also offer sufficient spatial resolution for uncovering individual cells—if possible, without selective staining.

Magnetic resonance tomography (MRT) is well established for imaging human brain tissue. It yields superb contrast between white and grey matter, but only limited spatial resolution. At present, the best medical MRT scanners produce voxel lengths at least one order of magnitude larger than the typical diameter of Purkinje cells. Although clinical X-ray computed tomography (CT) can give better spatial resolution it also does not reach the level of individual cells. Osmium-stained, individual ganglion cells encircled by soft tissue of the human inner ear, however, have been made visible by synchrotron radiation-based microcomputed tomography (SR μ CT), recently (Lareida *et al.* 2009). Together with the calculations on absorption contrast between white and grey matter (Brooks *et al.* 1980), we hypothesize that SR μ CT with the advantages of high monochromatic photon flux and spatial coherence could generate detailed images of human cerebellum that give deep insight into the anatomy at the cellular level.

Nonetheless, considerable doubt remains as to whether the density resolution in absorption contrast mode will actually result in high-quality images of unstained brain tissue. Consequently, the phase-contrast mode should be evaluated as well. X-ray phase-contrast approaches apply a variety of different principles but are all based on the phase shifts of X-ray waves penetrating the specimen (Fitzgerald 2000; Momose 2005). Set-ups based on a *crystal interferometer* (Bonse & Hart 1965) provide a direct measure of the profile of phase shifts induced into the X-ray wave by the specimen. Such instrumentation was successfully applied to mouse kidney (Beckmann *et al.* 1995) and rat cerebellum (Momose & Fukuda 1995). The obtained data clearly visualize subtle differences in tissue density. Unfortunately, the field of view is limited as the result of technological constraints in building the crystal interferometer. Moreover, it is a fact that the requirements for the experimental conditions are more restrictive. The second, and probably most widely used, class of X-ray phase-contrast techniques is *propagation-based* or *inline* methods. They emerged in the mid-1990s, after the first third-generation synchrotron light sources went into operation (Snigirev *et al.* 1995; Cloetens *et al.* 1996). *Inline* phase contrast does not need additional optical components as the *Fresnel* diffraction in the space between the sample and detector creates the contrast. This approach works only reasonably well for the third-generation synchrotron light sources, which possess a sufficient degree of spatial coherence. One particularly successful implementation of quantitative *inline* phase contrast is a technique known as *holotomography*, in which images recorded at several distances behind the specimen are combined to quantitatively retrieve the phase shift (Cloetens *et al.* 1999). A prominent, recent example is the imaging of a fossilized fish (Pradel *et al.* 2009), containing the

only known three-dimensional representation of a fossilized brain so far. The third approach, particularly relevant for soft tissues, is *analyser-based* imaging (ABI). Here, an analyser crystal is incorporated between the specimen and the detection unit to uncover the specimen-induced phase shift of the monochromatic X-rays (Förster *et al.* 1980; Davis *et al.* 1995). Combined with suitable data analysis, as shown for the *diffraction-enhanced imaging* (DEI) (Chapman *et al.* 1997), ABI gives access to absorption, refraction and scattering. Nevertheless, ABI requires a monochromatic X-ray beam with small divergence and high-quality, sufficiently large analyser crystals.

The recently developed *grating* or *Talbot* interferometry (David *et al.* 2002; Momose *et al.* 2003; Weitkamp *et al.* 2005; Pfeiffer *et al.* 2007c) is another, powerful phase-contrast technique. The X-ray interferometer consists of two line-grid structures placed between the specimen and the detector. Experiments on extracted rabbit liver (Momose *et al.* 2006), rat heart (Weitkamp *et al.* 2008) and rat brain (Pfeiffer *et al.* 2007a, 2009) have been performed. It has to be demonstrated, however, whether the spatial resolution of grating interferometry allows visualization of human brain tissue down to the level of individual cells.

The present communication aims at evaluating the potential of SR μ CT in absorption and phase-contrast mode to reveal morphological features in human cerebellum, especially the white and grey matter as well as Purkinje cells.

2. MATERIAL AND METHODS

2.1. Preparation of the brain specimen

The specimen was extracted from the donated body of a 68 year old male. All procedures were conducted in accordance with the Declaration of Helsinki and according to the ethical guidelines of the Canton of Basel. The brain was extracted at the Institute of Anatomy (University of Basel, Switzerland) within 48 h after death, and subsequently transferred to 10 per cent formalin for fixation. After approximately three months of fixation, a small block of the cerebellum was extracted at the University Hospital Zurich, Switzerland. The size of the block is about $6 \times 6 \times 11 \text{ mm}^3$. For the measurement, the block was placed and fixed in a 0.5 ml Eppendorf container filled with 4 per cent formalin solution.

2.2. Grating interferometry

The three-dimensional distribution of the complex refractive index of an object for X-rays of a given wavelength and photon energy can be written as

$$n(x, y, z) = 1 - \delta(x, y, z) + i\beta(x, y, z). \quad (2.1)$$

The imaginary part $\beta(x, y, z)$ describes the absorption of X-rays in the sample. It is related to the widely used linear X-ray attenuation coefficient $\mu(x, y, z)$ by

$$\mu(x, y, z) = \frac{4\pi}{\lambda} \cdot \beta(x, y, z), \quad (2.2)$$

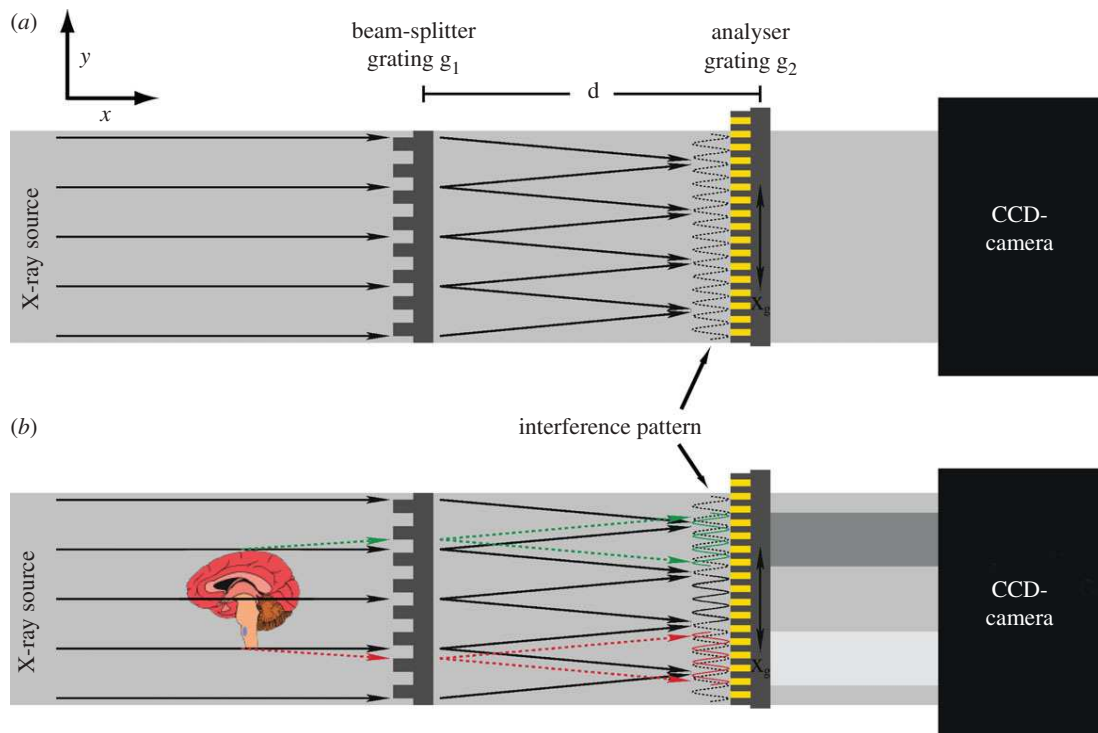


Figure 1. Top view of the experimental set-up consisting of the detector and the grating interferometer composed of a beam-splitter and an analyser grating. The x - and y -axis form a horizontal plane in which the coordinate x corresponds to the beam direction. The z -axis is oriented parallel to the x - y -plane in the direction of the viewer. The tomography rotation axis is oriented parallel to the z -axis. A phase object causes slight deflection of the incoming X-rays.

where λ is the wavelength of the incident X-rays. Conventional absorption tomography yields virtual slices or volume data corresponding to the local X-ray absorption coefficient $\mu(x, y, z)$.

Phase-contrast CT, on the other hand, provides the real part of the refractive index, often expressed in terms of its decrement from unity $\delta(x, y, z)$. It is related to the electron density distribution $\rho_e(x, y, z)$ by

$$\delta(x, y, z) = \frac{r_e \lambda^2}{2\pi} \rho_e(x, y, z), \quad (2.3)$$

for X-ray energies far away from the absorption edges. Here, the constant r_e is the classical electron radius.

For the detection of $\delta(x, y, z)$ a grating interferometer as schematically illustrated in figure 1 was used. Two gratings are arranged perpendicular to the incident X-ray beam. The *beam-splitter* grating g_1 consists of silicon stripes with the periodicity p_1 and a phase shift of $\Delta\phi = \pi$ in the X-ray wave. The requirements of the grating thickness D and absorption contrast C are determined by equation (2.4) using spectral data of the real part of the refractive index decrement $\delta(\lambda)$ and the linear X-ray absorption coefficients $\mu(\lambda)$ for the grating materials.

$$\Delta\phi = 2\pi \frac{D \cdot \delta(\lambda)}{\lambda}; \quad C = \frac{1 - \exp(-\mu(\lambda) \cdot D)}{1 + \exp(-\mu(\lambda) \cdot D)}. \quad (2.4)$$

At the X-ray photon energy of 23 keV used, a Si grating g_1 with $D = 28.4 \mu\text{m}$ provides π phase shift and negligible absorption contrast of $C_{g_1} = 1.1 \times 10^{-2}$. The grating lines induce fringe patterns in the X-ray

intensity distribution downstream. At distances from the beam-splitter grating of

$$d_n = \frac{np_1^2}{8\lambda}, \quad (2.5)$$

the intensity fringe contrast takes extreme values, with maximal contrast for odd *Talbot* orders $n = 1, 3, 5, \dots$, and vanishing contrast for even values of n (Weitkamp *et al.* 2006). The grating g_2 , termed *analyser* grating, with a periodicity $p_2 \approx p_1/2$, should have strongly absorbing stripes with a contrast of $C_{g_2} \approx 1$, here made of gold. The absorption requirement to the X-ray analyser grating is important to obtain the maximum visibility of the moiré fringes and to demonstrate the extreme resolution of $\Delta\delta = 10^{-8} - 10^{-9}$ of the real part of the refractive index decrement for this X-ray *Talbot* interferometry phase-contrast CT imaging of fine structures of the brain specimen. The distance from grating g_1 to grating g_2 equals the *Talbot* distance d_n with an odd *Talbot* order n .

The beam-splitter grating g_1 was fabricated at the Paul Scherrer Institut (Villigen, Switzerland) in a process involving lithography and anisotropic wet-etching into $\langle 110 \rangle$ -oriented silicon (David *et al.* 2007). The analyser grating g_2 was fabricated at the Karlsruhe Institute of Technology (Karlsruhe, Germany) by soft X-ray lithography of SU-8 resist (Reznikova *et al.* 2008). The unique planar technology provides aspect ratios of more than 50 for SU-8 polymer lamellar submicron grating matrixes that are filled uniformly with electroplated gold. The SU-8 polymer

created during the X-ray exposure and post-exposure-bake processes has unequalled mechanical, chemical and radiation stability.

A phase object between the X-ray source and the grating interferometer disturbs the interference pattern by deflecting the X-rays (figure 1b). These deflections cause slight spatial shifts of the stripes in the pattern. The distortions cannot be detected directly, as the detector pixel size is larger than the displacements. Grating g_2 has the function of detecting the displacements by using a *phase-stepping* method. As additional information, the phase-stepping method also provides the relative attenuation factor besides the relative object's phase shift. A detailed description of grating interferometry and of the phase-stepping method is given in Weitkamp *et al.* (2005). The quantitative relation between local beam propagation direction $\alpha(y, z)$, wave phase shift $\Phi(y, z)$ and decrement of X-ray refractive index $\delta(x, y, z)$ is

$$\alpha(y, z) = \frac{\lambda}{2\pi} \frac{\partial \Phi(y, z)}{\partial y} = \int_{-\infty}^{\infty} \frac{\partial \delta(x, y, z)}{\partial y} dx. \quad (2.6)$$

Analysis of the phase-stepping data from the interferometer yields $\alpha(y, z)$. The projection of δ along the beam propagation direction can then be obtained by calculating the indefinite integral (or, in terms of discrete values, the cumulative sum) of α along y . Tomographic reconstruction then yields the three-dimensional distribution of δ . If the filtered backprojection method is used for the tomographic reconstruction, the integration of α can be included in the filter kernel (Pfeiffer *et al.* 2007c). This is different from most implementations of analyser crystal-based tomography, first demonstrated by Dilmanian *et al.* (2000), in which the tomographically reconstructed phase-related quantity is usually the gradient $\partial\delta/\partial z$, owing to the fact that both the tomography rotation axis and the diffraction plane are usually vertical, although occasional exceptions are reported (Maksimenko *et al.* 2005).

The influence of small angle scattering on the $\delta(x, y, z)$ distribution was neglected. This was justified because the scattering by the analysed specimen (human brain tissue) is very weak. In addition, while scattering affects the signal-to-noise ratio, it has no influence on the retrieved value of δ .

The grating interferometry experiments were performed at the beamline ID19 (ESRF, Grenoble, France; Weitkamp *et al.* 2010). X-rays were taken from a U32 undulator with its gap set to 15.15 mm. The photon energy of 23 keV was selected using a double-crystal Si(111) monochromator in Bragg geometry. During the experiment, the photon flux density at the beamline ID19 corresponded to 10^{11} photons $\text{mm}^{-2} \text{s}^{-1}$. With a resulting field of view of 10.4 mm width and 6.1 mm height, two scans at different height position of the specimen were acquired in order to image the entire cerebellum piece. The interferometer consisted of a beam-splitter grating g_1 with a periodicity of $p_1 = 4.785 \mu\text{m}$ and a Si structure height of 29 μm , and an analyser grating g_2 with a periodicity of $p_2 = 2.400 \mu\text{m}$ and a structure height of 50 μm corresponding to an absorption contrast value of $C_{g_2} =$

0.993. With a distance between source and interferometer of 150 m and a distance between the gratings of $d = 479.4 \text{ mm}$ (9th Talbot order), the ratio of the grating periods, p_2/p_1 , was matched to the beam divergence (Weitkamp *et al.* 2006). The width of the contrast curve of a phase-stepping scan in this configuration was $p_2/(2d) = 2.5 \mu\text{rad}$ (full width half maximum (FWHM)). This is comparable to the rocking curve width of a Si-333 analyser crystal at the same energy (2.4 μrad FWHM), which could thus be expected to yield images of similar angular sensitivity in an analyser-based imaging set-up. However, since the energy bandwidth of Si-333 at 23 keV is more than 15 times narrower than that of Si-111, such an ABI set-up would be substantially less photon efficient than the grating-based set-up used here.

The Eppendorf container with the cerebellum in formalin solution was fixed at the high precision rotation stage and immersed in a water tank with parallel polymethylmethacrylat plates for the measurements. Note that the water-filled tank is fixed during the whole experiment. For this reason, all the changes in the projections during the scan should have been cancelled by the flat-field projections. In addition, no visible changes on the polymer were seen after multiple days of measurements. This arrangement ensured minimized artefacts owing to X-ray phase curvature induced by the container surface. Specimen and tank were located about 10 cm upstream of the beam-splitter grating. The detector, placed about 3 cm downstream of the analyser grating, was a lens-coupled scintillator and charge-coupled device (CCD) system using a FReLoN 2K (Fast-Readout, Low-Noise, ESRF Grenoble, France) CCD with 2048×2048 pixels. The effective pixel size corresponded to 5.1 μm . Projection radiographs were taken in 1501 steps over a range of 360° (i.e. step size 0.24°). At each projection angle, four phase-stepping images were taken over one period of the interferometer fringe pattern. The exposure time for each image was 1 s.

Repeated measurements on the formalin fixated soft tissue showed reproducibility. No influence of X-rays on the specimen was detected.

2.3. SR μ CT in absorption-contrast mode

SR μ CT experiments in absorption-contrast mode were carried out at the beamline BW2 operated by the GKSS-Research Center at the DORIS storage ring (HASYLAB at DESY, Hamburg, Germany; Beckmann *et al.* 2004, 2008) using a monochromatic beam of 14 keV. The wiggler source was set to a gap of 40 mm. The photon flux density during the experiment at the beamline BW2 is estimated to be about 2×10^{10} photons $\text{mm}^{-2} \text{s}^{-1}$. In order to enlarge the field of view, the experiment was performed with an asymmetric rotation axis position, shifted by 2 mm from the centre of the detection unit as used previously (e.g. Müller *et al.* (2007)). Using a detector with a field of view of $4.57 \times 3.05 \text{ mm}^2$, 1440 projections were recorded during the rotation of the specimen by 360° . The pixel size amounted to 3.0 μm . The spatial resolution of the entire absorption-contrast set-up was

determined by 10 per cent of the modulation transfer function (MTF) (Müller *et al.* 2002*b*) corresponding to 6.48 μm . The twofold binning of the projected highly X-ray absorbing edge led to a reduced spatial resolution of 8.77 μm again determined by 10 per cent of the MTF.

2.4. Data processing

In order to improve the density resolution of the absorption-contrast dataset, the projections were binned twofold (Thurner *et al.* 2004). This consequently led to a pixel size of 6.0 μm comparable to the 5.1 μm pixel size of the phase-contrast data. The absorption-contrast tomograms were obtained by means of the standard filtered back-projection reconstruction algorithm (Kak & Slaney 2001). The phase-contrast projection dataset was reconstructed using a modified filter kernel (Hilbert transform) in combination with standard filtered back-projection algorithm (Faris & Byer 1988; Pfeiffer *et al.* 2007*b,c*). Grating interferometric tomography provides, along with the decrement of the real part of the refractive index, the absorption-contrast tomograms at the selected photon energy, i.e. the imaginary part of the refractive index. For the reconstruction of these absorption-contrast projections, the same standard filtered back-projection reconstruction algorithm as for the BW2 data was used.

As it is important to compare identical volumes, the datasets obtained from the different facilities were registered using a three-dimensional rigid algorithm (Andronache *et al.* 2008; Fierz *et al.* 2008) with six degrees of freedom, namely three translation and three rotation degrees. For the registration, the more precise values of the pixel sizes, namely (5.95 ± 0.02) μm for the absorption contrast and (5.06 ± 0.02) μm for the phase-contrast results had to be used. These values correspond to averaged pixel sizes that were determined by the defined moving of a narrow object over several thousand pixels. Because of the different nature of image modalities, the registration was performed using the classical maximization of mutual information (MI) principle (Viola & Wells 1995; Maes *et al.* 1996). For robust registration, the absorption-contrast dataset had to be filtered using a 5×5 pixel median filter. This filtered dataset was only used for the registration. As a result of the registration and the determination of the common volume, we obtained three equally oriented sets of three-dimensional data of the cerebellum termed ‘absorption contrast BW2’, ‘absorption contrast ID19’ and ‘phase contrast ID19’.

For the analysis of the datasets, the histograms were approximated with a multi-Gaussian fit (Müller *et al.* 2002*a*) using the Levenberg–Marquardt algorithm in OriginPro 7.5 (OriginLab Corporation, Northampton, USA). The centre positions of the Gaussians on the abscissa then correspond to the absorption or decrement of the real part of the refractive index, and, for homogeneous objects, their width, expressed in terms of standard deviation, to the statistical errors of these values. For inhomogeneous objects, the standard deviation is basically dependent on the variation of the μ - or δ -values inside the different components.

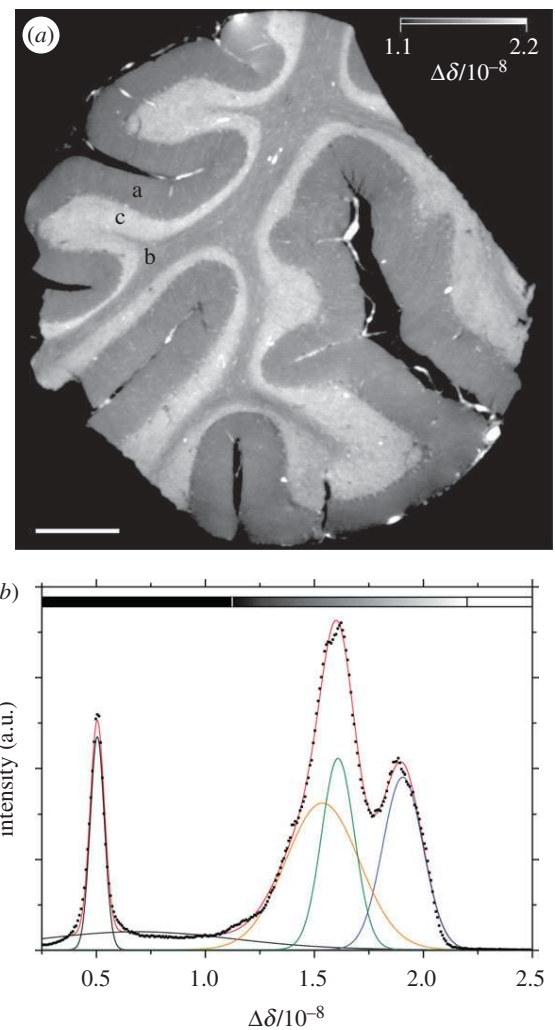


Figure 2. One reconstructed slice plus the appropriate histogram of the phase-contrast results showing three different strata and several blood vessels (bright regions in the slices that exceed the grey-scale range) of the human cerebellum. The mean value of the blood vessels amounts $\Delta\delta = 3.6 \times 10^{-8}$. The formalin peak (left peak in the diagram) has the value $\Delta\delta = 5.03 \times 10^{-9}$ with the standard deviation $\sigma_{\text{form}} = 0.32 \times 10^{-9}$. Thus, the grey-scale range corresponds to 34 standard deviations of the formalin peak. The standard deviation is a measure of the homogeneity of the tissue or solution: the narrower the width the Gaussian is, the more homogeneous the substance. (a) Scale bar, 1 mm. (b) Orange line, stratum moleculare (a); green line, white matter (b); navy blue line, stratum granulosum (c).

3. RESULTS

3.1. Phase-contrast SR μ CT

The reconstructed slice of the grating-based SR μ CT measurement (figure 2*a*) allows clear differentiation between the four morphological features, i.e. stratum moleculare, stratum granulosum and white matter, as well as blood vessels. The value $\Delta\delta = \delta_{\text{H}_2\text{O}} - \delta$ describes the decrement of the real part of the refractive index relative to water $\delta_{\text{H}_2\text{O}}$. The related histogram (figure 2*b*) shows besides the formalin peak at $\Delta\delta = 0.5 \times 10^{-8}$, two clearly distinguishable peaks with maxima at $\Delta\delta = 1.6 \times 10^{-8}$ and $\Delta\delta = 1.9 \times 10^{-8}$.

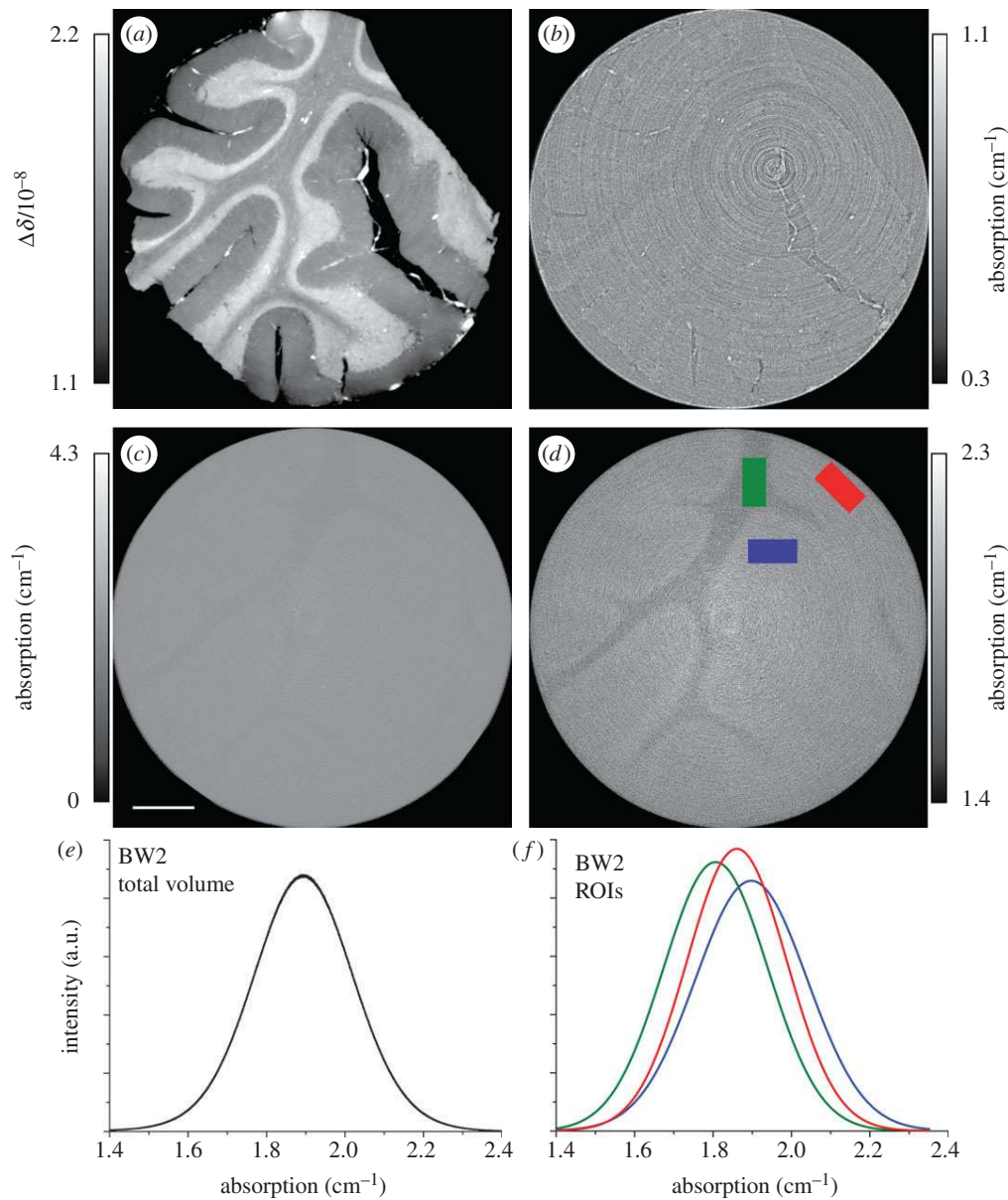


Figure 3. Grating interferometry phase-contrast reconstruction with a grey-scale range corresponding to 34 standard deviations of the formalin peak (a) compared with accordant BW2 absorption-contrast reconstruction with a grey-scale range corresponding to 34 (c) and 3 (d) standard deviations of the formalin peak. Figure (b) shows the absorption-contrast reconstruction obtained from grating interferometry with a grey-scale range of 3 standard deviations. Figure (e) demonstrates the histogram of the whole three-dimensional dataset whereas figure (f) illustrates the histogram of the areas labelled in figure (d), summed over 50 slices. ROI, region of interest.

Using a function composed of five Gaussians the histogram is reasonably well fitted, as shown by the solid red line in figure 2. The fit shows that the Gaussians corresponding to stratum moleculare and the white matter overlap so that a purely intensity-based segmentation is impossible. Fortunately, the stratum granulosum separates the two features and hence allows for segmentation of stratum moleculare and white matter.

The grey-scale range of the reconstructed slice corresponds to 34 standard deviations of the formalin peak $\sigma_{\text{form}} \approx \text{FWHM}_{\text{form}}/2.35 = 3.2 \times 10^{-10}$. As it can be assumed that the distilled water has no significant density fluctuations, the standard deviation of the background signal in the reconstructed slice can be interpreted as the measurement resolution of the

real part of the refractive index. Using the value of $\sigma_{\text{H}_2\text{O}} = 2.3 \times 10^{-10}$ in equation (2.3), the corresponding electron density resolution is 0.15 electrons per nm^3 and the mass density sensitivity for aqueous specimens is 0.25 mg cm^{-3} . The standard deviation of water in the processed projections of $\sigma_{\text{H}_2\text{O}} = 1.7 \times 10^{-8} \text{ rad}$ can then be interpreted as the measurement sensitivity of the deflection angles.

The Gaussian fit (figure 2b) was also used to quantify the values of the decrement of the real part of the refractive index for the features inside the human cerebellum plus formalin. Here the values $\Delta\delta_{\text{form}} = (0.50 \pm 0.03) \times 10^{-8}$ for the formalin, $\Delta\delta_{\text{med}} = (1.61 \pm 0.08) \times 10^{-8}$ for the white matter, corresponding to the green-coloured Gaussian, $\Delta\delta_{\text{mol}} = (1.54 \pm 0.17) \times 10^{-8}$ for the stratum

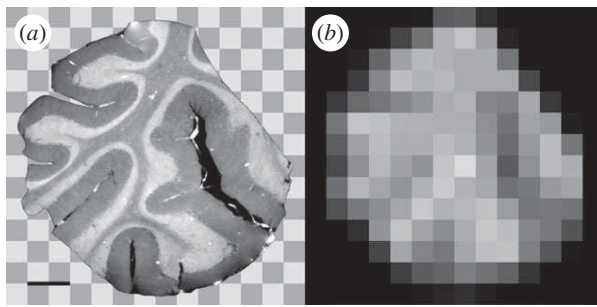


Figure 4. A 100-fold binning of the phase-contrast results reveals the distinction of the spatial resolution between SR μ CT and contemporary medical MRT. For that, we assumed a pixel size of 0.5 mm for nowadays common medical high-resolution MR-results. The black bar corresponds to 1 mm.

moleculare (orange Gaussian) and $\Delta\delta_{\text{gran}} = (1.90 \pm 0.09) \times 10^{-8}$ for the stratum granulosum (blue Gaussian) were obtained.

3.2. Density resolution in absorption and phase-contrast SR μ CT

As it is impossible to calculate the precise absorption values of the three different substances, formalin and white and grey matter, by plotting Gaussian fits in the histogram of the whole dataset (figure 3e), volumes representing the corresponding substances were chosen as represented in figure 3d. The dimension of the selected blocks was $65 \times 135 \times 50$ voxels. Using Gaussian plots, we obtained the values $\mu_{\text{form}} = (1.86 \pm 0.13) \text{ cm}^{-1}$ for the formalin, $\mu_{\text{med}} = (1.79 \pm 0.14) \text{ cm}^{-1}$ for the white matter and $\mu_{\text{grey}} = (1.90 \pm 0.14) \text{ cm}^{-1}$ for grey matter (figure 3f). Thus, the measurement sensitivity of the ‘absorption contrast BW2’ results in a value of 0.13 cm^{-1} .

3.3. Spatial resolution of SR μ CT

The internal stresses in formalin fixed bone were shown to be in the range of 50–70 MPa (Almer & Stock 2007). In order to quantify the shrinkage of the human brain during formalin fixation, the whole brain was additionally scanned on a Verio 3 Tesla whole body MRT scanner (Siemens HealthCare, Erlangen, Germany) with 0.7 mm isotropic pixel size before the extraction of the explored cerebellum block and compared with scans at different steps of fixation. The preliminary results show that the volume shrinkage of the whole human brain during 10 per cent formalin fixation is around 8 per cent.

Because of the huge differences in the pixel sizes, it was impossible to rigidly register the MRT results with the grating interferometry volume (figure 4a) in order to find the exact position and orientation of the small block inside the brain. To demonstrate the huge discrepancy of the pixel sizes between the clinical MRT- and SR μ CT-results and resultant failure of the registration, a 100-fold binning of the grating-based phase-contrast results was performed (figure 4b). The

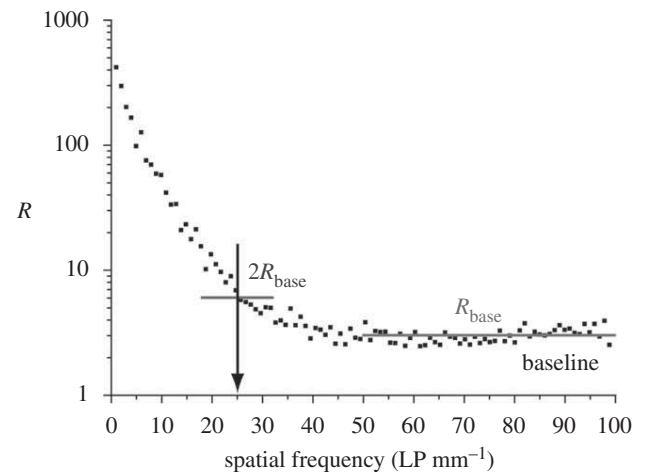


Figure 5. For the calculation of the spatial resolution, the ratio between $\text{rSP}_{\text{struc}}$ of a tomogram ROI with a fine structure and rSP_{back} of a tomogram ROI with background (water) was plotted over spatial frequency.

resulting pixel size of 0.5 mm matches the current typical medical high-resolution data.

The lowest limit of the spatial resolution achievable with a grating X-ray interferometer (Weitkamp *et al.* 2005) is given by twice the absorption grating period p_2 . In general, it becomes worse for higher Talbot orders. Resolution can be further limited by the detection system. An estimation of the spatial resolution of the experimental data was obtained by means of Fourier analysis of the processed projections and reconstructed tomograms. For that purpose, the *radial spectral power* (rSP) of a fine structure containing slice region of interest (200×200 pixels) was calculated ($\text{rSP}_{\text{struc}}$) and divided by the rSP of a background region of the same size (rSP_{back}) (Modregger *et al.* 2007). This ratio R was plotted against the spatial frequency in figure 5. The baseline observed for frequencies higher than 50 line pairs per millimetre (LP mm^{-1}) was associated with noise. Finally, the spatial resolution was estimated as the first observed frequency greater than twice the mean value of the baseline R_{base} . This value (25 LP mm^{-1}) corresponds to a peak to peak distance of $40 \mu\text{m}$. The spatial resolution was taken as half of this value, amounting to $20 \mu\text{m}$ as given for instance by Wang *et al.* (1991). Other calculations with different regions of interest of the tomograms resulted in an uncertainty of only $1 \mu\text{m}$. The same procedure was followed to determine the spatial resolution of the processed projections. The estimation resulted in a better spatial resolution of the projections compared with the tomograms, amounting to $(16.5 \pm 0.5) \mu\text{m}$. This value indicates the spatial resolution averaged over the two dimensions of the projection. The larger value of the reconstructed slices arises from the blurring during the application of the reconstruction algorithm.

3.4. Three-dimensional visualization of the grating-based phase-contrast results

The representation in the upper part of figure 6 is a virtual cut through a three-dimensional rendering of the phase-contrast tomogram. Using an intensity-based

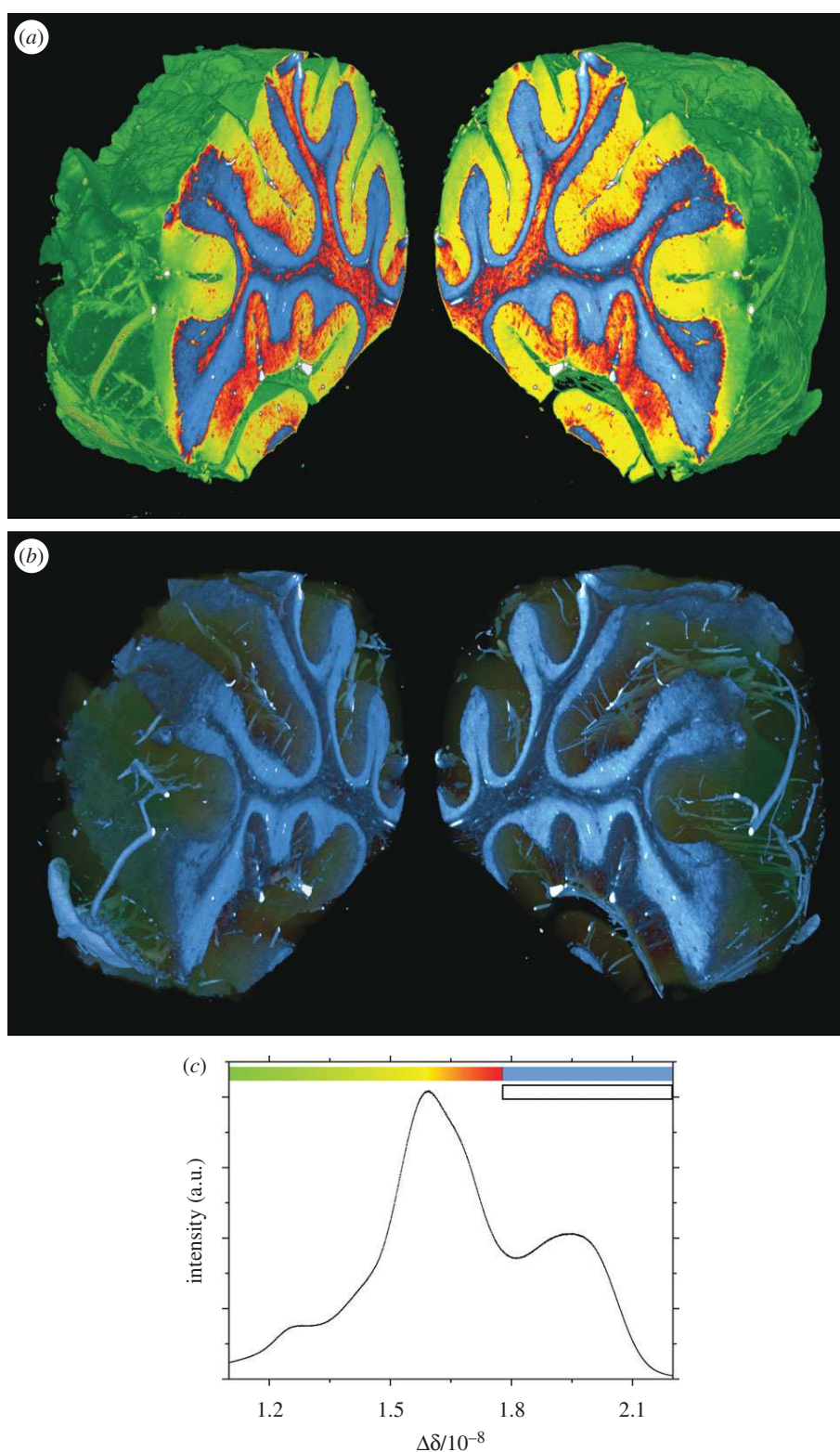


Figure 6. The phase-contrast three-dimensional rendering of the whole specimen with a virtual cut through it (*a,b*) demonstrates the feasibility to segment one of the shown structures by simple intensity-based segmentation. For the segmentation of the stratum granulosum the quantitative threshold values correspond to the grey-scale values of figure 2*a*. These values are also shown in the histogram of the whole dataset (*c*).

labelling of the dataset one can differentiate between the stratum granulosum (blue), the stratum moleculare (green–yellow–red gradient) and the white matter (mainly red). For the labelling, the threshold values of the histogram of the tomogram shown in figure 2 were

applied. The intensity-based segmentation of the stratum granulosum as represented in the middle of figure 6 was generated increasing the transparency of voxels with $\Delta\delta$ -values in the green–yellow–red gradient labelled range. This choice of the segmentation

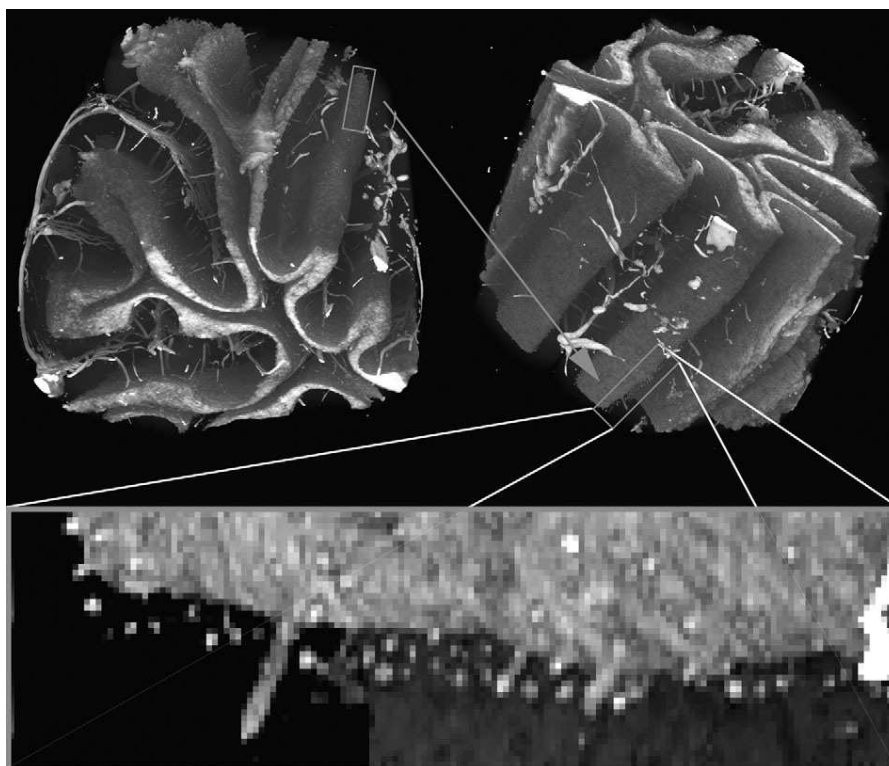


Figure 7. Another phase-contrast three-dimensional rendering of the specimen presumably shows the so-called Purkinje cells. The grey-scale values correspond to the white bar in the histogram in figure 6c.

highlights the characteristic course of blood vessels inside the cerebellum with an entrance angle of 90° to the surface of the stratum granulosum. The characteristics of the blood vessels can be seen even better in figure 7. The grey-scale range of this representation corresponds to the $\Delta\delta$ -values illustrated by the white bar in the histogram of figure 6. Besides the blood vessels, one can detect spherical microstructures with diameters of around $40\ \mu\text{m}$, 7–10 pixels wide, along the surface of stratum granulosum. On the basis of the location and the size of these features they are identified as the Purkinje cells.

4. DISCUSSION

Examining the histogram of one reconstructed slice (figure 2b), one observes that only four of the five Gaussians can be clearly related to known morphological structures of the human cerebellum. The fifth Gaussian with the largest half width describes the $\Delta\delta$ -values lying between the formalin and stratum moleculare related peaks. Therefore, this Gaussian basically corresponds to the partial volume between these two components. Aside from the partial volume one finds an additional peak at $\Delta\delta = 1.3 \times 10^{-8}$, which appears rather as a shoulder. This shoulder becomes more obvious in the histogram of the entire three-dimensional dataset (figure 6c). The quantitative analysis of the shoulder reveals that the related $\Delta\delta$ -values are located in areas of the cerebellum that were in direct contact with the formalin solution during the whole fixation period. Obviously,

the formalin treatment of the human cerebellum changes the electron density at the tissue periphery.

The usefulness of the absorption-contrast data of the second-generation synchrotron radiation source is restricted because intensity-based segmentation is in fact fairly complicated. The histogram of figure 3f illustrates the crucial overlap of the absorption values of the three components. Note that the formalin solution yields absorption values just between those of white and grey matter. Hence, another solution with higher or lower absorption should be applied. Phosphate buffer, for example, leads to higher absorption values (Germann *et al.* 2008) and is, therefore, better suited. The intensity-based segmentation of white and grey matter, however, remains difficult, since the green-coloured and blue-coloured peaks overlap in a significant manner.

The detailed comparison between the absorption-contrast data obtained from grating interferometry (figure 3b) and the conventional ones (figure 3d), both grey-scaled to three times the standard deviations σ_{form} of the formalin peak, shows that the grating interferometry results yield less contrast between the internal features. This behaviour is expected because the selected photon energy is too high for optimal image acquisition. The optimal energy of 14 keV for aqueous specimen with diameter $D = 1\ \text{cm}$ can be calculated from the equation $\mu = 2/D$ (Grodzins 1983a,b). The sharp features present in the ID19 absorption data concern internal interfaces as the results of edge enhancement and are not seen in the optimized absorption-contrast tomogram from the second-generation source.

The measurement sensitivity for the real part of the refractive index of the presented phase-contrast measurement (perhaps better termed as the resolution power) is enormously high and corresponds to an angular resolution of 1.7×10^{-8} rad. This corresponds to the size a small lorry parked on the Moon would appear from Earth. This value, however, is a factor of three lower than that found in a previous study (Pfeiffer *et al.* 2009). The difference is predominantly due to data binning, which resulted in $15 \mu\text{m}$ voxel size compared with the $5 \mu\text{m}$ in the present study (Thurner *et al.* 2004). Further influencing parameters are the operation mode of the insertion device, the photon energy that was around 10 per cent lower in the present study, the modified exposure time and the higher resolving FReLoN unit.

Comparing the histograms of a single phase-contrast slice (figure 2*b*) with the entire dataset (figure 6*c*), one recognizes significant differences. The slice-wise cross-check of the histograms allows us to conclude that the broader peaks in figure 6 are the consequence of relatively small displacements of the peak positions from slice to slice. It leads to rather higher uncertainties of the $\Delta\delta$ -values given in §3.1.

The sensitivity of the grating interferometry, however, is so high that individual Purkinje cells become visible without the application of any contrast agent. This is the most important result of the study, and to the best of our knowledge the first time that X-ray tomography permitted the identification of unstained cells in human soft tissue. So far, only osmium-stained ganglion cells have been made visible in absorption-contrast mode (Lareida *et al.* 2009).

The three-dimensional images of the Purkinje cells can be weighted against histological results. First, the grating-based SR μ CT data only show the larger features, namely the perikaryon and not the detailed dendritic tree, which propagates outwards in the direction of the stratum moleculare. Besides the limited spatial resolution, the reason behind this could be similar electron density values of the dendritic tree and the stratum moleculare. Second, according to the present tomographic study, the maximum diameter of an individual Purkinje cell corresponds to about $40 \mu\text{m}$ and the cell area to around $700 \mu\text{m}^2$. There is no doubt that the visualization of the Purkinje cells is close to the limit of the experimental set-up. A true measurement of the cell size is therefore impossible. Nevertheless, the spatial resolution of $20 \mu\text{m}$, together with the pixel size of $5.1 \mu\text{m}$, allows a rough estimate of the diameters of the features detected, which correspond in location and size to the Purkinje cells often visualized in two-dimensional histological slices shown, for instance, in Fatemi *et al.* (2002). Our results agree well with the data of Fatemi *et al.*, who obtained for the cell area $(661 \pm 85) \mu\text{m}^2$ from unfixed cerebellar sections but less with the result of stained histological slices by Tran *et al.* (1998), who found $(374 \pm 34) \mu\text{m}^2$. The alcohol fixation process apparently induces a significant shrinkage of the cells. Third, the two-dimensional Purkinje cell density of normal brain was determined at (16 ± 4) cells per mm^2 (Jeste *et al.* 1984), a value also obtained from our tomographic

data. Note, the density of Purkinje cells is reduced by diseases such as schizophrenia, autism, Huntington's disease and other movement disorders (Jeste *et al.* 1984; Tran *et al.* 1998; Fatemi *et al.* 2002). In summary, there remains no doubt that the micro-features shown in figure 7 are the Purkinje cells, since the location, size, shape and density are very well comparable with the histological results.

5. SUMMARY AND CONCLUSION

Grating-based X-ray tomography offers superior three-dimensional images of the human cerebellum, which not only allow for the discrimination between grey and white matter but also between stratum moleculare and stratum granulosum. Additionally, the clear visualization of non-stained individual Purkinje cells is possible—a technique that is unrivalled so far.

The authors gratefully acknowledge M. Müller-Gerbl and P. Zimmermann for the organization and extraction of the human brain, A. Morel and M. Imholz for the brain specimen blocking and A. Andronache for availability of the rigid registration tool. The project was partially funded by Swiss National Science Foundation (CR23I2_125 406) and was supported by the ESRF (proposal MD-407) and HASYLAB, DESY (proposal II-20060035 EC) by allocation of beam time. F. Pfeiffer acknowledges support of the DFG cluster of Excellence Munich-Centre for Advanced Phototonics.

REFERENCES

- Almer, J. D. & Stock, S. R. 2007 Micromechanical response of mineral and collagen phases in bone. *J. Struct. Biol.* **157**, 365–370. (doi:10.1016/j.jsb.2006.09.001)
- Andronache, A., von Siebenthal, M., Székely, G. & Cattin, P. 2008 Non-rigid registration of multi-modal images using both mutual information and cross-correlation. *Med. Image Anal.* **12**, 3–15. (doi:10.1016/j.media.2007.06.005)
- Beckmann, F., Bonse, U., Busch, F., Günnewig, O. & Biermann, T. 1995 A novel system for X-ray phase-contrast microtomography. *HASYLAB Annu. Rep.* **2**, 691–692.
- Beckmann, F., Donath, T., Dose, T., Lippmann, T., Martins, R. V., Metge, J. & Schreyer, A. 2004 Microtomography using synchrotron radiation at DESY: current status and future developments. *Proc. SPIE* **5535**, 1–10. (doi:10.1117/12.560561)
- Beckmann, F., Herzen, J., Haibel, A., Müller, B. & Schreyer, A. 2008 High density resolution in synchrotron-radiation-based attenuation-contrast microtomography. *Proc. SPIE* **70781D**, 1–13. (doi:10.1117/12.794617)
- Bonse, U. & Hart, M. 1965 An X-ray interferometer. *Appl. Phys. Lett.* **6**, 155–156. (doi:10.1063/1.1754212)
- Brooks, R. A., Di Chiro, G. & Keller, M. R. 1980 Explanation of cerebral white–gray contrast in computed tomography. *J. Comput. Assist. Tomogr.* **4**, 489–491. (doi:10.1097/00004728-198008000-00016)
- Chapman, D. *et al.* 1997 Diffraction enhanced X-ray imaging. *Phys. Med. Biol.* **42**, 2015–2025. (doi:10.1088/0031-9155/42/11/001)
- Cloetens, P., Barrett, R., Baruchel, J., Guigay, J.-P. & Schlenker, M. 1996 Phase objects in synchrotron radiation hard X-ray imaging. *J. Phys. D Appl. Phys.* **29**, 133–146. (doi:10.1088/0022-3727/29/1/023)

- Cloetens, P., Ludwig, W., Baruchel, J., Van Dyck, D., Van Landuyt, J., Guigay, J. P. & Schlenker, M. 1999 Holotomography: quantitative phase tomography with micrometer resolution using hard synchrotron radiation X-rays. *Appl. Phys. Lett.* **75**, 2912–2914. (doi:10.1063/1.125225)
- David, C., Nöhammer, B., Solak, H. H. & Ziegler, E. 2002 Differential X-ray phase contrast imaging using a shearing interferometer. *Appl. Phys. Lett.* **81**, 3287–3289. (doi:10.1063/1.1516611)
- David, C., Bruder, J., Rohbeck, T., Grünzweig, C., Kottler, C., Diaz, A., Bunk, O. & Pfeiffer, F. 2007 Fabrication of diffraction gratings for hard X-ray phase contrast imaging. *Microelectron. Eng.* **84**, 1172–1177. (doi:10.1016/j.mee.2007.01.151)
- Davis, T. J., Gao, D., Gureyev, T. E., Stevenson, A. W. & Wilkins, S. W. 1995 Phase-contrast imaging of weakly absorbing materials using hard X-rays. *Nature* **373**, 595–598. (doi:10.1038/373595a0)
- Dilmanian, F. A., Zhong, Z., Ren, B., Wu, X. Y., Chapman, L. D., Orion, I. & Thomlinson, W. C. 2000 Computed tomography of X-ray index of refraction using the diffraction enhanced imaging method. *Phys. Med. Biol.* **45**, 933–946. (doi:10.1088/0031-9155/45/4/309)
- Faris, G. W. & Byer, R. L. 1988 Three-dimensional beam-deflection optical tomography of a supersonic jet. *Appl. Opt.* **27**, 5202–5212. (doi:10.1364/AO.27.005202)
- Fatemi, S. H., Halt, A. R., Realmuto, G., Earle, J., Kist, D. A., Thuras, P. & Merz, A. 2002 Purkinje cell size is reduced in cerebellum of patients with autism. *Cell. Mol. Neurobiol.* **22**, 171–175. (doi:10.1023/A:1019861721160)
- Fierz, F. C. et al. 2008 The morphology of anisotropic 3D-printed hydroxyapatite scaffolds. *Biomaterials* **29**, 3799–3806. (doi:10.1016/j.biomaterials.2008.06.012)
- Fitzgerald, R. 2000 Phase-sensitive X-ray imaging. *Phys. Today* **53**, 23–26. (doi:10.1063/1.1292471)
- Förster, E., Goetz, K. & Zaumseil, P. 1980 Double crystal diffraction for the characterization of targets for laser fusion experiments. *Krist. Tech.* **15**, 937–945. (doi:10.1002/crat.19800150812)
- Germann, M., Morel, A., Beckmann, F., Andronache, A., Jeanmonod, D. & Müller, B. 2008 Strain fields in histological slices of brain tissue determined by synchrotron radiation-based micro computed tomography. *J. Neurosci. Methods* **170**, 149–155. (doi:10.1016/j.jneumeth.2008.01.011)
- Grodzins, L. 1983a Optimum energies for X-ray transmission tomography of small samples. *Nucl. Instrum. Methods* **206**, 541–545. (doi:10.1016/0167-5087(83)90393-9)
- Grodzins, L. 1983b Critical absorption tomography of small samples. *Nucl. Instrum. Methods* **206**, 547–552. (doi:10.1016/0167-5087(83)90394-0)
- Jeste, D. V., Barban, L. & Parisi, J. 1984 Reduced purkinje cell density in Huntington's disease. *Exp. Neurol.* **85**, 78–86. (doi:10.1016/0014-4886(84)90162-6)
- Kak, A. C. & Slaney, M. 2001 *Principles of computerized tomographic imaging* Philadelphia, PA: SIAM.
- Lareida, A., Beckmann, F., Schrott-Fischer, A., Glueckert, R., Freysinger, W. & Müller, B. 2009 High-resolution X-ray tomography of the human inner ear: synchrotron radiation-based study of nerve fiber bundles, membranes, and ganglion cells. *J. Microsc.* **234**, 95–102. (doi:10.1111/j.1365-2818.2009.03143.x)
- Maes, F., Collignon, A., Vandermeulen, D., Marchal, G. & Suetens, P. 1996 Multi-modality image registration by maximization of mutual information. In *Proc. IEEE Math. Meth. in Biomed. Im. Anal.*, 21–22 June 1996, San Francisco, CA, pp. 14–22. San Francisco, CA: Society for Industrial and Applied Mathematics. (doi:10.1109/MMBIA.1996.534053)
- Maksimenco, A., Ando, M., Hiroshi, S. & Yuasa, T. 2005 Computed tomographic reconstruction based on X-ray refraction contrast. *Appl. Phys. Lett.* **86**, 124105. (doi:10.1063/1.1891305)
- Modregger, P., Lübbert, D., Schäfer, P. & Köhler, R. 2007 Spatial resolution in Bragg-magnified X-ray images as determined by Fourier analysis. *Phys. Status Solidi a* **204**, 2746–2752. (doi:10.1002/pssa.200675685)
- Momose, A. 2005 Recent advances in X-ray phase imaging. *Jpn J. Appl. Phys. Part 1* **44**, 6355–6367. (doi:10.1143/JJAP.44.6355)
- Momose, A. & Fukuda, J. 1995 Phase-contrast radiographs of nonstained rat cerebellar specimen. *Med. Phys.* **22**, 375–379. (doi:10.1118/1.597472)
- Momose, A., Kawamoto, S., Koyama, I., Hamaishi, Y., Takai, K. & Suzuki, Y. 2003 Demonstration of X-ray Talbot interferometry. *Jpn. J. Appl. Phys., Part 2* **42**, 866–868.
- Momose, A., Yashiro, W., Takeda, Y., Suzuki, Y. & Hattori, T. 2006 Phase tomography by X-ray Talbot interferometry for biological imaging. *Jpn J. Appl. Phys. Part 1* **45**, 5254–5262. (doi:10.1143/JJAP.45.5254)
- Müller, B., Beckmann, F., Huser, M., Maspero, F. A., Székely, G., Ruffieux, K., Thurner, P. J. & Wintermantel, E. 2002a Non-destructive three-dimensional evaluation of a polymer sponge by micro-tomography using synchrotron radiation. *Biomol. Eng.* **19**, 73–78. (doi:10.1016/S1389-0344(02)00014-X)
- Müller, B. et al. 2002b Non-destructive three-dimensional evaluation of biocompatible materials by microtomography using synchrotron radiation. *Proc. SPIE* **4503**, 178–188. (doi:10.1117/12.452843)
- Müller, B. et al. 2007 Morphology of bony tissues and implants uncovered by high-resolution tomographic imaging. *Int. J. Mater. Res.* **98**, 613–621.
- Pfeiffer, F., Bunk, O., David, C., Bech, M., Le Duc, G., Bravin, A. & Cloetens, P. 2007a High-resolution brain tumor visualization using three-dimensional X-ray phase contrast tomography. *Phys. Med. Biol.* **52**, 6923–6930. (doi:10.1088/0031-9155/52/23/010)
- Pfeiffer, F., Bunk, O., Kottler, C. & David, C. 2007b Tomographic reconstruction of three-dimensional objects from hard X-ray differential phase contrast projection images. *Nucl. Instrum. Methods Phys. Res. Sect. A* **580**, 925–928. (doi:10.1016/j.nima.2007.06.104)
- Pfeiffer, F., Kottler, C., Bunk, O. & David, C. 2007c Hard X-ray phase tomography with low-brilliance sources. *Phys. Rev. Lett.* **98**, (doi:10.1103/PhysRevLett.98.108105)
- Pfeiffer, F., David, C., Bunk, O., Poitry-Yamate, C., Grütter, R., Müller, B. & Weitkamp, T. 2009 High-sensitivity phase-contrast tomography of rat brain in phosphate buffered saline. *J. Phys. Conf. Ser.* **186**, 0120461. (doi:10.1088/1742-6596/186/1/012046)
- Pradel, A., Langer, M., Maisey, J. G., Geffard-Kuriyama, D., Cloetens, P., Janvier, P. & Tafforeau, P. 2009 Skull and brain of a 300-million-year-old chimaeroid fish revealed by synchrotron holotomography. *Proc. Natl Acad. Sci. USA* **106**, 5224–5228. (doi:10.1073/pnas.0807047106)
- Reznikova, E., Mohr, J., Boerner, M., Nazmov, V. & Jakobs, J. 2008 Soft X-ray lithography of high aspect ratio SU8 submicron structures. *Microsyst. Technol.* **14**, 1683–1688. (doi:10.1007/s00542-007-0507-x)
- Snigirev, A. A., Snigireva, I., Kohn, V., Kuznetsov, S. & Schelokov, I. 1995 On the possibilities of X-ray phase contrast microimaging by coherent high-energy synchrotron radiation. *Rev. Sci. Instrum.* **66**, 5486–5492. (doi:10.1063/1.1146073)

- Turner, P. J., Beckmann, F. & Müller, B. 2004 An optimization procedure for spatial and density resolution in hard X-ray micro-computed tomography. *Nucl. Instrum. Methods Phys. Res. B* **225**, 599–603. (doi:10.1016/j.nimb.2004.05.027)
- Tran, K. D., Smutzer, G. S., Doty, R. L. & Arnold, S. E. 1998 Reduced Purkinje cell size in the cerebellar vermis of elderly patients with schizophrenia. *Am. J. Psych.* **155**, 1288–1290.
- Trepel, M. 2008 *Neuroanatomie/Struktur und Funktion* Munich, Germany: Urban & Fischer.
- Viola, P. & Wells, W. M. 1995 Alignment by maximization of mutual information. In *Proc. 5th Int. Conf. on Comp. Vis., 20–23 June, Cambridge, MA*, pp. 16–23. (doi:10.1109/ICCV.1995.466930)
- Wang, L., Ho, P. P., Liu, C., Zhang, G. & Alfano, R. R. 1991 Ballistic 2-D imaging through scattering walls using an ultrafast optical Kerr gate. *Science* **253**, 769–771. (doi:10.1126/science.253.5021.769)
- Weitkamp, T., Diaz, A., David, C., Pfeiffer, F., Stampanoni, M., Cloetens, P. & Ziegler, E. 2005 X-ray phase imaging with a grating interferometer. *Opt. Expr.* **13**, 6296–6304. (doi:10.1364/OPEX.13.006296)
- Weitkamp, T., David, C., Kottler, C., Bunk, O. & Pfeiffer, F. 2006 Tomography with grating interferometers at low-brilliance sources. *Proc. SPIE* **6318**, 63180S. (doi:10.1117/12.683851)
- Weitkamp, T., David, C., Bunk, O., Bruder, J., Cloetens, P. & Pfeiffer, F. 2008 X-ray phase radiography and tomography of soft tissue using grating interferometry. *Eur. J. Radiol.* **68S**, S13–S17.
- Weitkamp, T. *et al.* 2010 Status and evolution of the ESRF beamline ID19. *AIP Conf. Proc.* **1221**, 33–38. (doi:10.1063/1.3399253)

2.4 Multimodal imaging: PC- μ CT, μ MRI and histology

The following section deals with the advantages and disadvantages of X-ray phase contrast microtomography, magnetic resonance microscopy and histology. Furthermore, it presents a possibility to merge these complementary imaging techniques.

Published in Scientific Reports



SUBJECT AREAS:

BIOMEDICAL
ENGINEERING

BRAIN

STRUCTURE OF SOLIDS AND
LIQUIDS

BIOPHYSICS

Multimodal imaging of human cerebellum - merging X-ray phase microtomography, magnetic resonance microscopy and histology

Georg Schulz¹, Conny Waschkies², Franz Pfeiffer³, Irene Zanette^{3,4}, Timm Weitkamp⁵, Christian David⁶ & Bert Müller¹

Received
20 July 2012

Accepted
2 October 2012

Published
9 November 2012

Correspondence and
requests for materials
should be addressed to
B.M. (bert.mueller@
unibas.ch)

¹Biomaterials Science Center, University of Basel, Basel, Switzerland, ²Animal Imaging Center, Institute for Biomedical Engineering, ETH & University of Zurich, Switzerland, ³Department of Physics (E17), Technische Universität München, Garching, Germany, ⁴European Synchrotron Radiation Facility, Grenoble, France, ⁵Synchrotron Soleil, Gif-sur-Yvette, France, ⁶Laboratory for Micro- and Nanotechnology, Paul Scherrer Institut, Villigen, Switzerland.

Imaging modalities including magnetic resonance imaging and X-ray computed tomography are established methods in daily clinical diagnosis of human brain. Clinical equipment does not provide sufficient spatial resolution to obtain morphological information on the cellular level, essential for applying minimally or non-invasive surgical interventions. Therefore, generic data with lateral sub-micrometer resolution have been generated from histological slices post mortem. Sub-cellular spatial resolution, lost in the third dimension as a result of sectioning, is obtained using magnetic resonance microscopy and micro computed tomography. We demonstrate that for human cerebellum grating-based X-ray phase tomography shows complementary contrast to magnetic resonance microscopy and histology. In this study, the contrast-to-noise values of magnetic resonance microscopy and phase tomography were comparable whereas the spatial resolution in phase tomography is an order of magnitude better. The registered data with their complementary information permit the distinct segmentation of tissues within the human cerebellum.

Minimally or non-invasive surgical interventions on the brain are generally based on less detailed patient-specific imaging (pre- and intra-operative) and high-resolution generic anatomical data. The generic knowledge of brain microstructure currently relies on two-dimensional (2D) evaluation of histological slices, which requires time-consuming sectioning, staining, and (manual, expert-based) image analysis. The advantages of histology are sub-micrometer resolution and excellent tunable contrast depending on the staining protocol^{1,2}. However, the technique does not provide isotropic three-dimensional (3D) information of the soft and hard tissues, as is regularly obtained using magnetic resonance imaging (MRI) and X-ray computed tomography (CT). Furthermore, it is hard to imagine image-guided neurosurgery³ without MR guidance. Conventional MRI is a well-established technique for brain imaging, and yields superb contrast between white and grey matter but only limited spatial resolution. At present, medical MR systems produce images with typically sub-millimetre voxel lengths. Small animal MR microscopy (μ MRI) scanners equipped with stronger gradient systems and operating at higher magnetic field strengths have been used to visualize mouse brains *in vivo*^{4,5} and pieces of human brain post-mortem^{6,7} with voxel sizes of a few tens of micrometers. Conventional CT also provides fully quantitative 3D data ultimately reaching higher spatial resolution than MRI. The CT contrast for brain tissue, however, is weak. Despite low inherent brain tissue contrast, micro-CT (μ CT) as a non-destructive technique has already been used to correct deformations induced in data sets obtained by histological sectioning during the preparation of histology⁸. In order to obtain a better contrast than in these absorption-based studies, synchrotron radiation-based phase-contrast μ CT (PC- μ CT)^{9,10} was recently applied to human brain¹¹. X-ray phase-contrast methods are based on the phase shifts of X-ray waves penetrating the specimen which is related to the decrement $\delta(x,y,z)$ of the real part of the refractive index distribution. A variety of PC- μ CT methods based on crystal interferometry¹², propagation-based (or *inline*) contrast^{13,14} or analyzer-based imaging (ABI)^{15,16} are available today. More recently, grating interferometry^{17–19} (also known as *Talbot* interferometry)

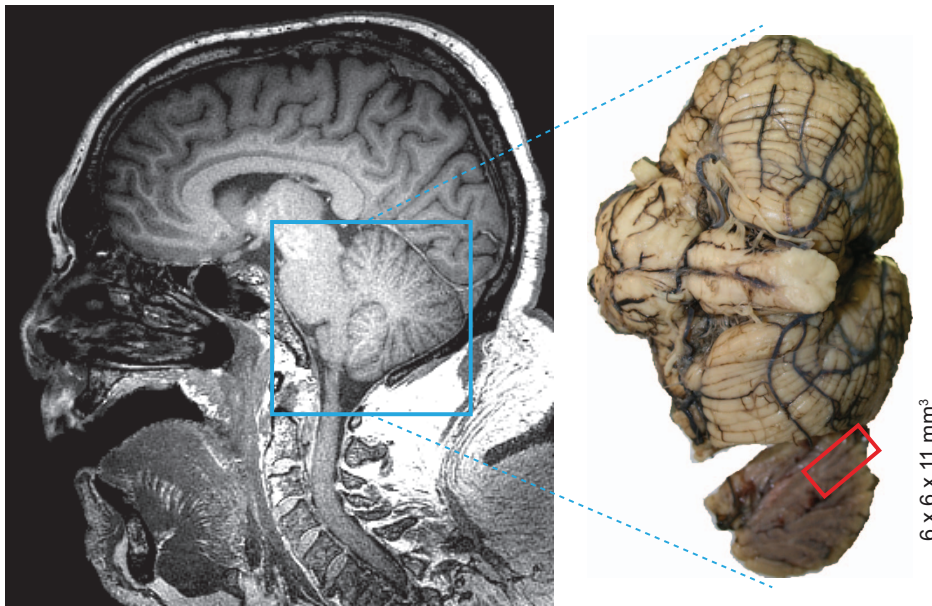


Figure 1 | Cerebellum block extraction. The photograph (right) and MR-slice acquired using a Verio 3T whole body scanner (Siemens Health Care, Erlangen, Germany) illustrate the location and size of the cerebellum within the donated body.

was developed, which reaches the especially high contrast required for identifying structures with small differences in electron density as is the case in brain^{11,20,21}.

In the light of these inherent advantages and disadvantages of MR- and CT-based techniques and histology, the aim of the present communication is to elucidate how far the combination of the complementary methods μ MRI, grating-based PC- μ CT and histology yields additional information on the microanatomy of the human cerebellum.

Results

3D imaging. A specimen taken from the human cerebellum (Figure 1) was visualised in 3D using grating-based PC- μ CT and μ MRI. Figure 2 shows virtual cuts through identical regions of the brain tissue obtained with the two imaging techniques after non-rigid 3D registration²². In the mixed T1/T2*-weighted μ MRI images white matter structures appear darker than grey matter structures. Grey matter consists of two components: the stratum granulosum and the stratum moleculare. Because of the weak MR-contrast between these layers, however, it is impossible to segment these structures with an intensity-based algorithm. PC- μ CT, on the contrary, provides high contrast between these grey matter layers: with the stratum granulosum appearing as a bright feature and the stratum moleculare as the dark outer structure. The white matter (interior dark region in PC- μ CT) exhibits δ -values very similar to the stratum moleculare and can only be segmented because the stratum granulosum is located between the two tissues. Therefore, an intensity-based segmentation is also impossible in this case. This can be deduced from the related histograms of the 3D data in Figure 2. The histogram of the μ MRI data (green-coloured triangles in the figure) shows a shoulder (left) associated with white matter, and a peak associated with grey matter (right). The histogram of the PC- μ CT data (red-coloured squares) contains two peaks and a shoulder. The first peak corresponds to the stratum moleculare, which was in direct contact with formalin during the whole fixation period of the brain. The second peak is a superposition of the stratum moleculare that was in contact with formalin only for restricted periods of time and the white matter. The shoulder on the right originates from the stratum granulosum.

Tissue contrast. The images in Figure 2 acquired with PC- μ CT and μ MRI show the characteristic morphology of the human cerebellum. The contrast-to-noise ratio c between two anatomical structures can be defined as

$$c = \frac{|x_{c1} - x_{c2}|}{FWHM_{back}} \quad (1)$$

where x_{ci} are the centre positions of the related peaks in the histograms and $FWHM_{back}$ is the full-width-at-half-maximum of the background signal, here formaldehyde solution and perfluoropolyether, respectively. This definition of the denominator was chosen for practical reasons (see supplementary material). Using Equation 1, six c -values between the four anatomical structures were determined for PC- μ CT and μ MRI (Figure 3). The highest contrast in the PC- μ CT images is the contrast between stratum granulosum and tissue in contact with formalin (E) and has the value of $c_{PC-\mu CT_max} = 6.4 \pm 0.2$. Using μ MRI a maximum value of $c_{\mu MRI_max} = 9.5 \pm 0.1$ was determined, corresponding to the contrast between white matter and tissue in contact with formalin (C).

Joint histogram. The superposition of peaks in the individual histograms prevents the segmentation of the anatomical features. In particular, it is impossible to differentiate between stratum moleculare and stratum granulosum in the μ MRI data, and between white matter and stratum moleculare in the PC- μ CT data. Combining μ MRI and PC- μ CT using a joint histogram, however, allows the distinct discrimination between the characteristic soft tissues (Figure 4). To do so, the first step was the identification of the 2D maxima in the joint histogram corresponding to the tissues of interest using a multi-Lorentzian fit. Subsequently, the intersections of the Lorentzians were calculated. These intersections characterize the interfaces between the anatomical structures and allow a distinct differentiation between white matter, given in red, stratum granulosum in blue, and stratum moleculare in yellow. In addition, the green-coloured peak indicates regions of stratum moleculare, which were in direct contact with formalin during the whole fixation period.

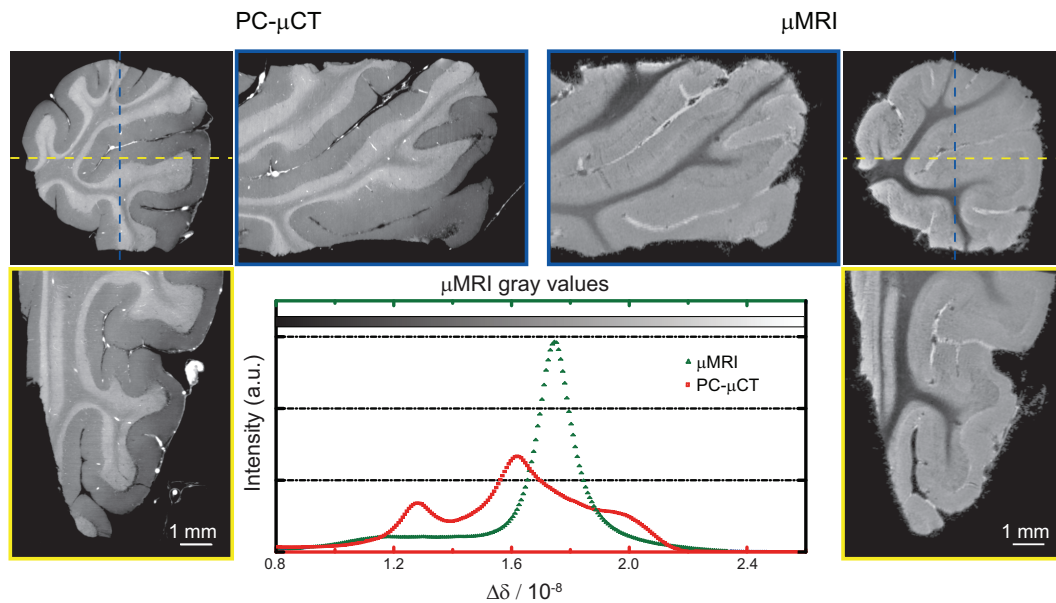


Figure 2 | X-ray phase micro computed tomography and MR microscopy of the cerebellum. The selected orthogonal virtual cuts through the specimen and the corresponding histograms of the 3D data illustrate the power and complementary nature of the two techniques for imaging the human cerebellum.

Spatial resolution. In order to evaluate the spatial resolution of μ MRI, PC- μ CT, and histology, firstly line plots through the registered data of the human cerebellum (see Figure 5) were inspected. The spatial resolution of the imaging techniques can be deduced by comparing the roughness of the line plots. Histology has the best spatial resolution followed by PC- μ CT then μ MRI. To quantify this observation, the spatial resolution λ_{SR} was calculated by Fourier analysis^{11,23}. The radial spectral power (rSP) of a structure of interest in a 100×100 pixel region of a selected slice (rSP_{struc}) was calculated and divided by the rSP of a background region of same size (rSP_{back}) (i.e. of formalin for PC- μ CT, perfluoropolyether for μ MRI and glass without brain tissue for histology). This ratio was plotted

against the spatial frequency. The peak-to-peak distance of the first frequency larger than twice the mean value of the baseline (noise) was divided by two to determine the spatial resolution²⁴. The λ_{SR} -values corresponded to $(6 \pm 1) \mu\text{m}$ for histology, to $(20 \pm 5) \mu\text{m}$ for PC- μ CT, and to $(210 \pm 40) \mu\text{m}$ for μ MRI.

Multimodality. The morphology of the cerebellum can be properly visualized combining μ MRI, PC- μ CT, and histology. Figure 6 illustrates one possible way of combining the 2D images of the three techniques used in this study. Each technique is represented by one of the colour channels red/green/blue (RGB) (see Figure 6, left image). Such a colour representation directly illustrates the contributions of the individual techniques. For example the yellow colour, which indicates the stratum granulosum, is mainly the superposition of contrast from the PC- μ CT and μ MRI, whereas the purple colour (white matter) primarily arises from the PC- μ CT and the histology signals.

Discussion

Grating interferometry is based on the detection of the deflection angles of the X-rays passing through the specimen. After reconstruction, a 3D distribution of the decrement δ of the real part of the refractive index of the specimen can be obtained, which is directly related to the electron density distribution

$$\delta(x, y, z) = \frac{r_e \lambda^2}{2\pi} \rho_e(x, y, z) \quad (2)$$

with the classical electron radius r_e and the X-ray wavelength λ ²⁵.

In MRI, contrast between different tissues is determined by their relative spin densities ρ_s , their characteristic relaxation properties at the purported magnetic field strength, i.e. their distinguished T_1 (longitudinal) and T_2 resp. T_2^* (transversal) relaxation times, and the imaging sequence and parameters used (in particular the echo time TE , the repetition time TR and the flip angle α). In a very general manner, the measured amplitude of the signal for a gradient echo sequence can be described as

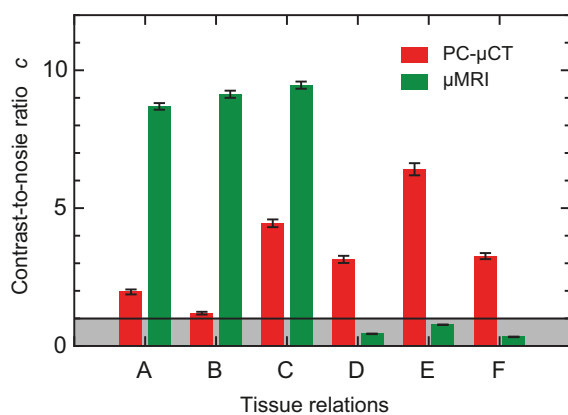


Figure 3 | Tissue contrast in human cerebellum. The above data compare contrast values between μ MRI and PC- μ CT for white matter and stratum granulosum (A), white matter and stratum moleculare (B), white matter and tissue in contact with formalin (C), stratum granulosum and stratum moleculare (D), stratum granulosum and tissue in contact with formalin (E) and between stratum moleculare and tissue with formalin (F).

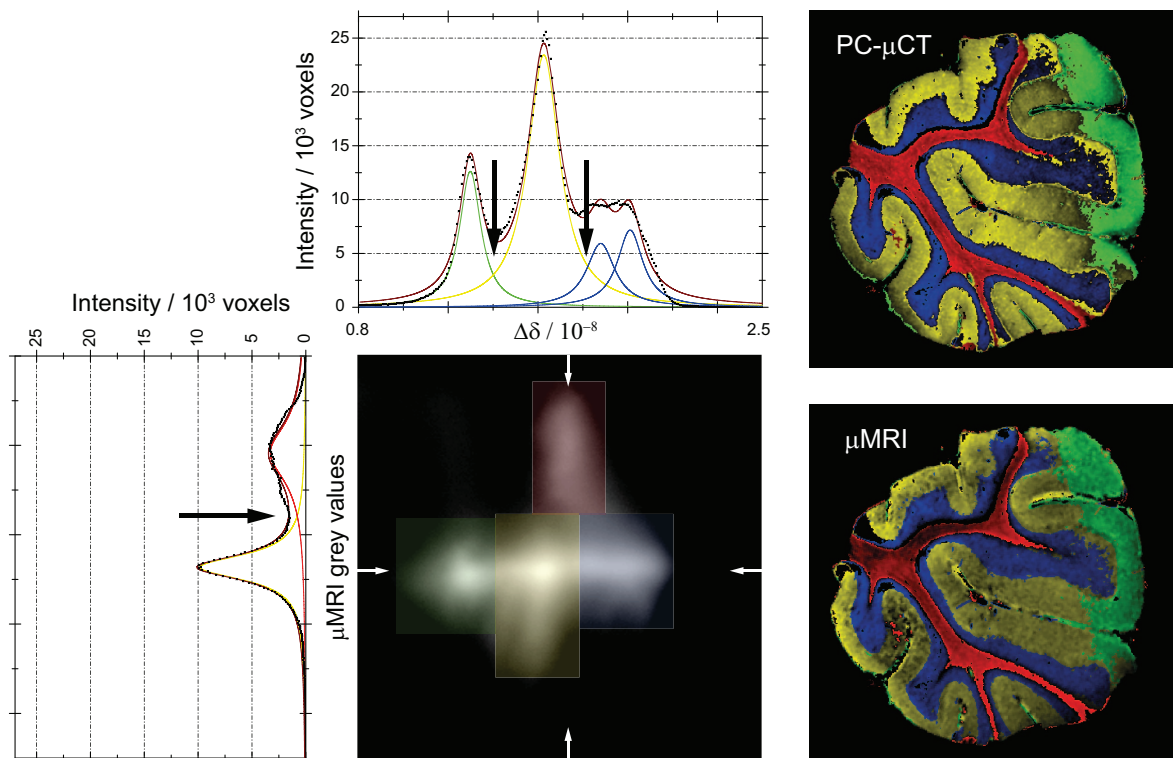


Figure 4 | Segmentation by means of a joint histogram. From the joint histogram of the phase tomography and MR microscopy data it is possible to distinctly segment the stratum granulosum, stratum moleculare, white matter, and brain tissue that was in direct contact with formalin for a longer period of time than other parts. The white arrows indicate the positions of the related line plots. The colours of the virtual cuts of PC- μ CT and μ MRI on the right side correspond to the colours assigned to the four peaks in the joint histogram.

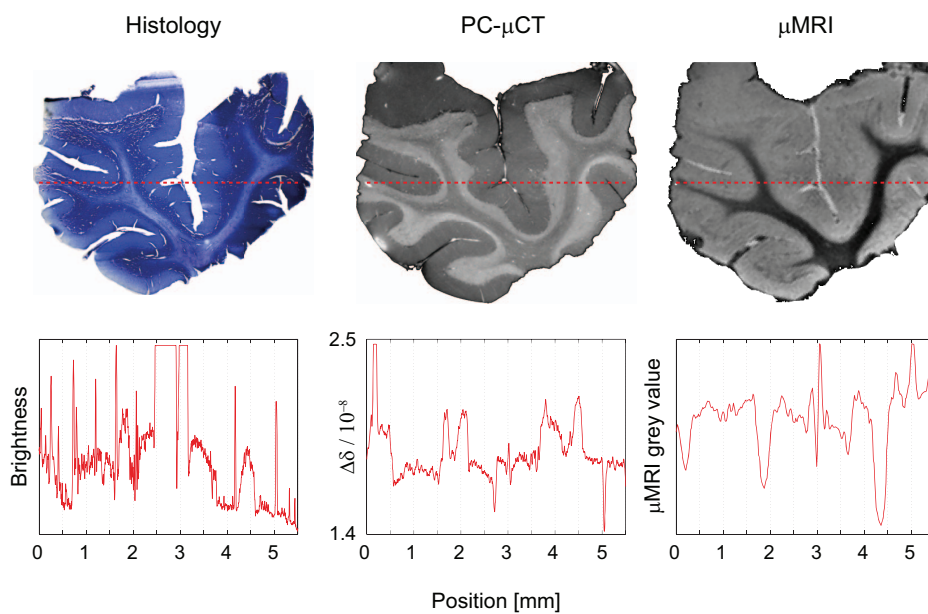


Figure 5 | Spatial resolution of histology, X-ray phase tomography, and MR microscopy. Comparable line plots through selected slices demonstrate that the spatial resolution decreases from histology via PC- μ CT to μ MRI.

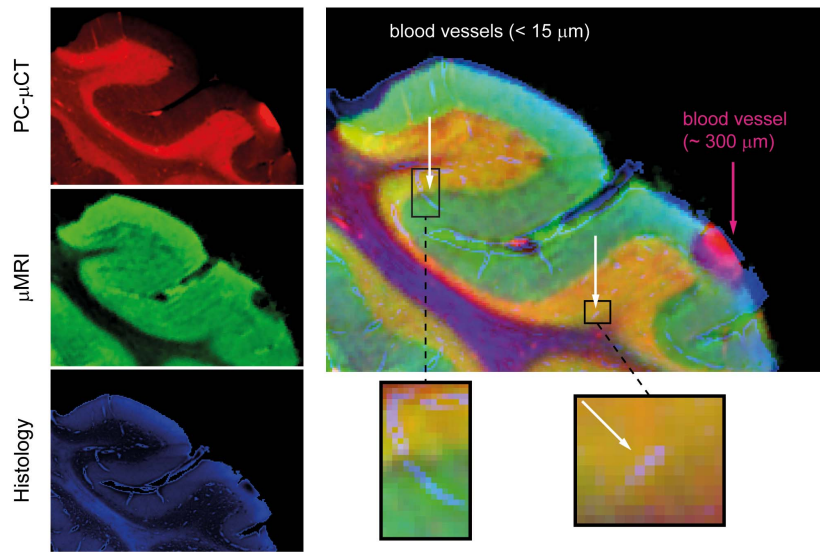


Figure 6 | Multimodal imaging of the cerebellum. The fusion of slices from PC- μ CT, μ MRI, and histology using the RGB channels directly visualizes the contributions from the three imaging techniques. The combination of the three techniques permits the distinction of otherwise indistinguishable anatomical features, such as the separation between white matter (violet), stratum granulosum (yellow), stratum moleculare (green) and blood vessels of different sizes (purple and white arrows). The enlarged regions (with different magnification) show the light blue coloured small capillaries.

$$S(\rho, T_1, T_2, TE, TR) \propto \rho_s \sin \alpha \left(1 - e^{-\frac{TR}{T_1}}\right) \frac{e^{-\frac{TE}{T_2}}}{1 - \cos \alpha e^{-\frac{TR}{T_1}}} \quad (3)$$

where

$$\frac{1}{T_2^*} = \frac{1}{T_2} + \gamma \Delta B_0 \text{ with } \gamma \Delta B_0 \approx 60 \text{ Hz} \quad (4)$$

takes into account the refocusing of magnetization components that were dephased under the readout gradient of the imaging sequence, while dephasing of magnetization resulting from static field inhomogeneities such as susceptibility effects contribute to the image contrast. In order to optimize tissue contrast, dedicated imaging sequence parameters were chosen based on literature values for grey and white matter at magnetic fields of 9.4 T²⁶.

Before the acquired data can be compared and combined, they must be registered with each other in 3D space. It was shown that the 3D registration using the maximization of the mutual information²² gives precise results for the registration of tomography data from different imaging modalities²⁷. A rigid registration including three degrees of translation and three degrees of rotation seems to be sufficient for the 3D data set acquired by PC- μ CT and μ MRI. Although the brain tissue undergoes shrinkage during formalin fixation, further deformations over long-time periods are minimal. Nevertheless, an affine registration with an additional three scaling factors compensates for the error in individual pixel sizes. In our case a non-rigid registration was required to correlate the corresponding voxels between the imaging modalities. This approach accounts for possible deformations within the brain tissue induced during the transfer of the specimen from the cylindrical polyethylene container (filled with formaldehyde) used in PC- μ CT measurements into the container (with perfluoropolyether) for μ MRI. Because of the deformations induced during sectioning and staining, the histological slice was also non-rigidly registered with the tomography data.

The virtual cuts through the μ MRI and PC- μ CT data sets in Figure 2 elucidate the pros and cons of each method. It is well known that MRI provides superb contrast between white and grey matter. White matter (dark region) can easily be distinguished from the grey

matter (bright region) in our mixed T1/T2*-weighted μ MRI images. On the contrary, differentiation between layers of grey matter tissues, in particular between stratum granulosum and stratum moleculare, is hardly possible. Here, PC- μ CT provides a clear distinction between these anatomical structures. White matter (inner dark region), however, has a comparable electron density to stratum moleculare (outer dark region). These observations are quantified using Equation 1 and summarized in Figure 3. With the definition of the contrast-to-noise ratio c presented in this manuscript, a value $c > 1$ is required to distinguish anatomical structures using intensity-based algorithms. Therefore, one can conclude that the PC- μ CT contrast is sufficiently high to distinguish between the four tissues whereas μ MRI contrast is restricted to white and grey matter. Additionally, the PC- μ CT pixel size is a factor of nine smaller than μ MRI, although the maximal c -value observed in the PC- μ CT results is slightly lower than the maximal μ MRI contrast-to-noise ratio. Binning the tomography data reduces the spatial resolution but improves the contrast²⁸. Therefore, we can state that the contrast-to-noise between the two methods yields comparable values.

In addition to the contrast-to-noise ratio c , we also consider the spatial resolution λ_{SR} to assess image quality. Following the work of Thurner *et al.*²⁸, we combine these two values in the quality factor q

$$q = \frac{c}{\lambda_{SR}} \quad (5)$$

Using the maximal contrast values of PC- μ CT and μ MRI and the corresponding spatial resolution values, one obtains quality factors of $(0.32 \pm 0.09) \mu\text{m}^{-1}$ for PC- μ CT and $(0.05 \pm 0.01) \mu\text{m}^{-1}$ for μ MRI. Based on this definition, PC- μ CT yields six times better images than μ MRI. More importantly, however, the complementary results of the two data sets can be derived using a joint histogram as presented in Figure 4. Three anatomical structures can be segmented, i.e. white matter (red), stratum granulosum (blue) and stratum moleculare (yellow). Furthermore, due to its high sensitivity, PC- μ CT allows the detection of differences within the tissue induced by different periods of formalin fixation. The green regions in Figure 4 correspond to domains of stratum moleculare, which were in direct



contact with formalin for the whole fixation period of 120 days and not only for 20 days.

In summary, we demonstrate the advantages and disadvantages of PC- μ CT, μ MRI and histology and present a method to combine data from these complementary techniques in order to segment the anatomical layers of the human cerebellum post mortem. The clear segmentation of the three layers allows us to quantify the ratios between these volumes. Given that cell death in the cerebellum is a common cause of neurological disease, e.g. in cerebellar ataxias²⁹ and that abnormalities in the cerebellum have more recently also been implicated in autism and neuropsychiatric disorders^{30,31} methods for a reliable quantitative assessment of cerebellar morphology and pathology are certainly needed. Unfortunately, the currently available stereological methods for the cerebellum are very time consuming and often lack precision^{31,32}. The presented method has the potential to significantly reduce the effort and improve the quality of quantitative stereological assessments of the cerebellum.

Methods

Specimen preparation. The brain from the donated body of a 68-year-old male was extracted at the Institute of Anatomy (University of Basel, Switzerland) within 48 h after death. The whole brain was transferred to 10% formalin solution for fixation. All procedures were conducted in accordance with the Declaration of Helsinki and according to the ethical guidelines of the Canton of Basel. The small cerebellum block ($6 \times 6 \times 11$ mm³) was extracted at the University Hospital Zurich, Switzerland, after approximately three months of fixation (Figure 1). During the measurements the specimen was placed in a 0.5 mL Eppendorf container filled with 4% formalin solution for PC- μ CT and with perfluoropolyether (Fomblin® Y-LC 80, Solvay Solexis, Bollate, Italy) for μ MRI in order to reduce the background signal and susceptibility artefacts at the tissue-liquid interface³³.

Grating-based X-ray phase tomography. A detailed description of grating interferometry can be found in the literature^{11,19,34,35}. The experiment was performed at the beamline ID19 (ESRF, Grenoble, France) at the interferometer installed there³⁶ with X rays from the U32 undulator with a gap set to 15.15 mm. Using a double-crystal Si(111)-monochromator in Bragg geometry a photon energy of 23 keV was selected. The imaging of the entire specimen required two scans to obtain a field of view 11 mm high and 6 mm wide. The beam-splitter grating g_1 (made at the Paul Scherrer Institut, Villigen, Switzerland) with a periodicity of $p_1 = 4.785$ μ m had a Si structure height of 29 μ m, which corresponds, within a few percent, to a phase shift of π for 23-keV X rays. The analyzer grating g_2 (made at the Karlsruhe Institute of Technology, Eggenstein-Leopoldshafen, Germany) had lines of gold with a periodicity of $p_2 = 2.400$ μ m and 50 μ m structure height. This corresponds to an intensity transmission of only about 6×10^{-3} through the teeth of the analyzer grating comb, i.e., a contrast of 100%. With a distance between source and interferometer of 150 mm and a distance between the gratings of $d = 479.4$ mm (corresponding to the 9th Talbot order), the ratio of the grating periods p_2/p_1 was matched to the beam divergence³⁵. The sample container was immersed in a water tank with parallel polymethylmethacrylate plates in order to minimize artefacts due to X-ray phase curvature induced by a conical container-air interface. The specimen was located 10 cm upstream of the beam-splitter grating. The detector was a lens-coupled scintillator and charge-coupled device (CCD) system using a FreLoN 2K (Fast-Readout, Low-Noise, ESRF Grenoble, France) CCD with 2048×2048 pixels and an effective pixel size of 5.1 μ m, placed approximately 3 cm downstream of the analyzer grating. Projection radiographs were taken in 1501 steps over a range of 360°. At each projection angle, four phase-stepping images with an exposure time of 1 s each were taken over one period of the interference pattern.

Magnetic resonance microscopy. The μ MRI measurements were carried out on a 9.4 T, 30 cm horizontal small animal MR unit (Bruker BioSpec, Bruker BioSpin MRI, Ettlingen, Germany) equipped with a transceiver cryogenic quadrature radio frequency (RF) surface coil (CryoProbe™) designed for MRI of the mouse brain at increased sensitivity. High-resolution structural images were acquired with a T₂*-weighted 3D FLASH sequence with isotropic voxel size of 45 μ m (field of view (FOV) $1.35 \times 0.90 \times 1.35$ mm³, acquisition matrix (MTX) $300 \times 200 \times 300$, echo time (TE) 12 ms repetition time (TR) 400 ms, flip angle (α) 15°, number of averages (NA) 1 at a total acquisition time of 400 minutes.

Histology. Sections of 50 μ m thickness of the cerebellum block were prepared using a microtome with vibrating blade HM 650 V (Micom International GmbH, Walldorf, Germany). For the staining procedure, the sections were mounted on gelatinized slides and stained for Nissl with cresyl violet¹. Microphotographs of selected slices were taken using a Leica MZ16 microscope and DFC420-C digital camera.

Data processing. The reconstruction of the phase-contrast dataset was carried out using a modified filter kernel (Hilbert transform) in combination with a standard back-projection algorithm^{34,37,38}. Because the signal intensity in the μ MRI images

varies with the coil sensitivity profile, further processing was performed. For the correction of the inhomogeneities a modified fuzzy C-means algorithm was applied³⁹. For a reasonable analysis of the joint histogram, the 3D datasets were non-rigidly registered using the classical maximization of mutual information (MI) principle^{40,41}. The chosen registration algorithm is based on the adaptive hierarchical image subdivision strategy, which decomposes the non-rigid matching problem into numerous local affine registrations of image segments of decreasing size⁴². The local registrations were again performed using the classical maximization of MI principle. The local registration parameters were identified using the Powell multi-dimensional search algorithm⁴² such that the MI between the reference and the floating sub-images was maximized. The hierarchical image splitting strategy⁴³ recently underwent several improvements and was extended to 3D^{23,44}. For region selection in the joint histogram, the line plots were approximated with a multi-Lorentzians fit using the Levenberg-Marquardt algorithm in OriginPro 7.5 (OriginLab Corporation, Northampton, USA).

- Morel, A. *Stereotactic Atlas of the Human Thalamus and Basal Ganglia*. (Informa Healthcare New York, 2007).
- Schaltenbrand, G. &ahren, W. *Atlas for Stereotaxy of the Human Brain*. (Thieme, Stuttgart, 1977).
- Jolesz, F. A., Nabavi, A. & Kikinis, R. Integration of interventional MRI with computer-assisted surgery. *J. Magn. Reson. Imaging* **13**, 69–77 (2001).
- Benveniste, H. & Blackband, S. MR microscopy and high resolution small animal MRI: Applications in neuroscience research. *Prog. Neurobiol.* **67**, 393–420 (2002).
- Ahrens, E. T. *et al.* MR microscopy of transgenic mice that spontaneously acquire experimental allergic encephalomyelitis. *Magn. Reson. Med.* **40**, 119–132 (1998).
- Fatterpekar, G. M. *et al.* Cytoarchitecture of the human cerebral cortex: MR microscopy of excised specimens at 9.4 Tesla. *Am. J. Neuroradiol.* **23**, 1313–1321 (2002).
- Fatterpekar, G. M. *et al.* MR microscopy of normal human brain. *Magn. Reson. Imaging Clin. N. Am.* **11**, 641–653 (2003).
- Germann, M. *et al.* Strain fields in histological slices of brain tissue determined by synchrotron radiation-based micro computed tomography. *J. Neurosci. Methods* **170** (1), 149–155 (2008).
- Fitzgerald, R. Phase-sensitive X-ray imaging. *Phys. Today* **53** (7), 23–26 (2000).
- Momose, A., Fujii, A., Kadowaki, H. & Jinnai, H. Three-dimensional observation of polymer blend by X-ray phase tomography. *Macromolecules* **38** (16), 7197–7200 (2005).
- Schulz, G. *et al.* High-resolution tomographic imaging of a human cerebellum: Comparison of absorption and grating-based phase contrast. *J. R. Soc. Interface* **7**, 1665–1676 (2010).
- Bonse, U. & Hart, M. An X-ray interferometer. *Appl. Phys. Lett.* **6** (8), 155–156 (1965).
- Snigirev, A. A., Snigireva, I., Kohn, V., Kuznetsov, S. & Schelokov, I. On the possibilities of x-ray phase contrast microimaging by coherent high-energy synchrotron radiation. *Rev. Sci. Instrum.* **66** (12), 5486–5492 (1995).
- Cloetens, P., Barrett, R., Baruchel, J., Guigay, J.-P. & Schlenker, M. Phase objects in synchrotron radiation hard x-ray imaging. *J. Phys. D: Appl. Phys.* **29**, 133–146 (1996).
- Förster, E., Goetz, K. & Zaumseil, P. Double crystal diffractometry for the characterization of targets for laser fusion experiments. *Krist. Tech.* **15** (8), 937–945 (1980).
- Davis, T. J., Gao, D., Gureyev, T. E., Stevenson, A. W. & Wilkins, S. W. Phase-contrast imaging of weakly absorbing materials using hard X-rays. *Nature* **373**, 595–598 (1995).
- David, C., Nöhhammer, B., Solak, H. H. & Ziegler, E. Differential X-ray phase contrast imaging using a shearing interferometer. *Appl. Phys. Lett.* **81**, 3287–3289 (2002).
- Momose, A. *et al.* Demonstration of X-ray Talbot interferometry. *Jpn. J. Appl. Phys., Part 2* **42** (7B), 866–868 (2003).
- Weitkamp, T. *et al.* X-ray phase imaging with a grating interferometer. *Opt. Express* **13**, 6296–6304 (2005).
- Pfeiffer, F. *et al.* High-sensitivity phase-contrast tomography of rat brain in phosphate buffered saline. *J. Phys. Conf. Ser.* **186**, 012046 (2009).
- Pfeiffer, F. *et al.* High-resolution brain tumor visualization using three-dimensional X-ray phase contrast tomography. *Phys. Med. Biol.* **52** (23), 6923–6930 (2007).
- Andronache, A., von Siebenthal, M., Székely, G. & Cattin, P. Non-rigid registration of multi-modal images using both mutual information and cross-correlation. *Med. Image Anal.* **12** (1), 3–15 (2008).
- Modregger, P., Lübbert, D., Schäfer, P. & Köhler, R. Spatial resolution in Bragg-magnified X-ray images as determined by Fourier analysis. *Phys. Status Solidi A* **204**, 2746–2752 (2007).
- Wang, L., Ho, P. P., Liu, C., Zhang, G. & Alfano, R. R. Ballistic 2-D imaging through scattering walls using an ultrafast optical Kerr gate. *Science* **253**, 769–771 (1991).
- Als-Nielsen, J. & McMorrow, D. *Elements of Modern X-ray Physics*. (John Wiley & Sons, Chichester, 2011).
- Kuo, Y.-T., Herlihy, A. H., So, P.-W., Bhakoo, K. K. & Bell, J. D. In vivo measurements of T1 relaxation times in mouse brain associated with different



- modes of systemic administration of manganese chloride. *J. Magn. Reson. Imaging* **21**, 234–239 (2005).
27. Müller, B. *et al.* Three-dimensional registration of tomography data for quantification in biomaterials science. *Int. J. Mater. Res.* **103**, 242–249 (2012).
 28. Thurner, P., Beckmann, F. & Müller, B. An optimization procedure for spatial and density resolution in hard X-ray micro-computed tomography. *Nucl. Instrum. Methods Phys. Res. B* **225**, 599–603 (2004).
 29. van Gaalen, J. & van de Warrenburg, B.P.C. A practical approach to late-onset cerebellar ataxia: putting the disorder with lack of order into order. *Pract. Neurol.* **12**, 14–24 (2012).
 30. Villanueva, R. The cerebellum and neuropsychiatric disorders. *Psychiatry Res. in press*, published online before print 22 March (2012).
 31. Andersen, K., Andersen, B. B. & Pakkenberg, B. Stereological quantification of the cerebellum in patients with Alzheimer's disease. *Neurobiol. Aging* **33**, 197.e111–197.e120 (2010).
 32. Agashiwala, R. M., Louis, E. D., Hof, P. R. & Perl, D. P. A novel approach to non-biased systematic random sampling: A stereologic estimate of Purkinje cells in the human cerebellum. *Brain Res.* **1236**, 73–78 (2008).
 33. Smith, B. R., Huff, D. S. & Johnson, G. A. Magnetic resonance imaging of embryos: An internet resource for the study of embryonic development. *Comp. Med. Imag. Graph.* **23**, 33–40 (1999).
 34. Pfeiffer, F., Kottler, C., Bunk, O. & David, C. Hard X-ray phase tomography with low-brilliance sources. *Phys. Rev. Lett.* **98**, 108105 (2007).
 35. Weitkamp, T., David, C., Kottler, C., Bunk, O. & Pfeiffer, F. Tomography with grating interferometers at low-brilliance sources. *Proc. SPIE* **6318**, 63180S (2006).
 36. Weitkamp, T. *et al.* Recent developments in X-ray Talbot interferometry at ESRF-ID19. *Proc. SPIE* **7804**, 780406 (2010).
 37. Faris, G. W. & Byer, R. L. Three-dimensional beam-deflection optical tomography of a supersonic jet. *Appl. Opt.* **27**, 5202–5212 (1988).
 38. Pfeiffer, F., Bunk, O., Kottler, C. & David, C. Tomographic reconstruction of three-dimensional objects from hard X-ray differential phase contrast projection images. *Nucl. Instrum. Methods Phys. Res. Sect. A* **580**, 925–928 (2007).
 39. Ahmed, M. N., Yamany, S. M., Mohamed, N., Farag, A. A. & Moriarty, T. A modified fuzzy C-means algorithm for bias field estimation and segmentation of MRI data. *IEEE Trans. Med. Imaging* **21**, 193–199 (2002).
 40. Maes, F., Collignon, A., Vandermeulen, D., Marchal, G. & Suetens, P. Multimodality image registration by maximization of mutual information. *Mathematical Methods in Biomedical Image Analysis. IEEE*, 14–22 (1996).
 41. Viola, P. & Wells, W. M. Alignment by maximization of mutual information. *Proceedings of the fifth international conference on computer vision*, 16–23 (1995).
 42. Press, W. H., Flannery, B. P., Teukolsky, S. A. & Vetterling, W. T. *Numerical Recipes in C - The Art of Scientific Computing*. (Cambridge University Press, 1988).
 43. Likar, B. & Pernus, F. A hierarchical approach to elastic registration based on mutual information. *Image Vis. Comput.* **19** (1–2), 33–44 (2001).
 44. Schulz, G. *et al.* Three-dimensional strain fields in human brain resulting from formalin fixation. *J. Neurosci. Methods* **202**, 17–27 (2011).

Acknowledgements

The authors gratefully acknowledge M. Müller-Gerbl and P. Zimmermann for the organization and carrying out the extraction of the human brain, J. Kapfhammer for anatomical and medical information, A. Morel for the brain specimen blocking, M. Imholz for the histology of the specimen, S. Rutishauser for the preparation of the beam-splitter grating, M. Rudin for giving us the opportunity to perform the magnetic resonance microscopy experiments and A. Andronache for making the non-rigid registration tool available. The authors thank M. N. Holme for improving the readability and for correcting the language. T. W. acknowledges support from the French research networks (réseau thématique de recherche avancée, RTRA) “Digiteo” and “Triangle de la Physique” (grants 2009-034T and 2009-79D). F. P. acknowledges financial support through the DFG Cluster of Excellence Munich-Center for Advanced Photonics and the European Research Council (FP7, Starting Grant No. 240142). The project was partially funded by the Swiss National Science Foundation (CR23I2_125 406) and was supported by the ESRF (proposal MD-407) through beam time allocation. This work was partly conducted with the support of the Karlsruhe Nano Micro Facility (KNMF), a Helmholtz Research Infrastructure at Karlsruhe Institute of Technology (KIT).

Author contributions:

G.S. prepared the specimen for the measurements; F.P., T.W. and C.D. developed the phase-contrast set up; G.S., I.Z., T.W. and B.M. performed phase-contrast tomography experiments; C.W. performed magnetic resonance microscopy experiments; G.S. and B.M. analyzed the data and prepared the figures; G.S. and B.M. wrote the initial manuscript; all authors discussed the results and contributed to the final manuscript.

Additional information

Supplementary information accompanies this paper at <http://www.nature.com/scientificreports>

Competing financial interests: The authors declare no competing financial interests.

License: This work is licensed under a Creative Commons Attribution-NonCommercial-NoDerivs 3.0 Unported License. To view a copy of this license, visit <http://creativecommons.org/licenses/by-nc-nd/3.0/>

How to cite this article: Schulz, G. *et al.* Multimodal imaging of human cerebellum - merging X-ray phase microtomography, magnetic resonance microscopy and histology. *Sci. Rep.* **2**, 826; DOI:10.1038/srep00826 (2012).

3 Conclusions

The human brain increases its volume after extraction due to lower pressure outside the cranium. On the other hand a volume shrinkage occurs during the formalin fixation which can be explained by a cross-linking process of the proteins. The quantification of these counteractive processes can be performed using an affine registration algorithm applied on MRI data sets at diverse steps of the study.

In addition to the global changes, the extraction and formalin fixation induces a local strain field because of the inhomogeneity of the brain tissue. These local artifacts can be achieved by means of a 3D non-rigid registration. The resulting corrected data sets generate a morphological condition of the brain which is very close to the post mortem situation inside the cranium.

Taking advantage of immense high photon flux density (e.g. 10^{10} photons mm^{-2} s^{-1} at DORIS storage ring, HASYLAB at DESY, Hamburg) and tunable energies SR μ CT shows true micrometer resolution, but only allows investigation on human tissues post mortem as the dosage is definitely too high for living organisms.

Grating-based phase contrast μ CT using hard X-rays shows a much higher contrast between structures within soft tissues, than absorption contrast. The reason is the composition of soft tissue which mainly consists of elements with low atomic numbers ($Z < 10$).

With its spatial resolution in the sub-micrometer range, histology can dissolve structures one magnitude smaller than PC- μ CT can achieve. Compared to μ MRI this difference is even of two magnitudes. The combination of the three complementary imaging techniques allows the segmentation of anatomical layers of the human cerebellum post mortem and, in addition, contains the high-resolution information from histology.

The high sensitivity of grating-based phase contrast even allows the visualization of structures within the human thalamus. Due to the marginal differences in absorption and electron density within the thalamus, the visualization of it is one of the most ambitious challenges in X-ray tomography. The high-quality images can be used for the determination of the 3D deformation vector field induced by sectioning and staining of the inhomogeneous soft tissue during histology.

Grating-based SR μ CT also offers superior 3D images of the human cerebellum, which not only allow for the discrimination between gray and white matter but also between stratum moleculare and stratum granulosum. With an electron density resolution of 0.15 electrons per nm^3 corresponding to a mass density sensitivity of 0.25 mg cm^{-1} for aqueous specimens, a clear visualization of individual non-stained Purkinje cells surrounded by soft tissue is possible - a technique that is so far unrivaled.

Having voxel sizes of a few tens micrometers, MR microscopy shows sufficient contrast between white and gray matter, but almost no differences within the gray matter can be observed. Contrary to that, PC- μ CT shows a clear contrast between two tissues of gray matter, but only marginal contrast between stratum moleculare and white matter. The complementary information of PC- μ CT and μ MRI were merged by means of a joint histogram which allows a clear segmentation of all of these structures.

PC- μ CT shows a comparable maximal contrast-to-noise ratio to μ MRI for the human cerebellum. However, PC- μ CT yields six times higher values for the quality factor which is based on the contrast and spatial resolution.

Bibliography

- [1] F. Azevedo, L. Carvalho, L. Grinberg, J. Farfel, R. Ferretti, R. Leite, W. Filho, R. Lent, S. Herculano-Houzel. *Equal numbers of neuronal and nonneuronal cells make the human brain an isometrically scaled-up primate brain*. The Journal of Comparative Neurology **513**, 532-541 (2009).
- [2] J. Kennedy, G. ter Haar, D. Cranston. *High intensity focused ultrasound: surgery of the future?* British Journal of Radiology **76** (909), 590-599 (2003).
- [3] F. Jolesz, N. McDannold. *Current status and future potential of MRI-guided focused ultrasound surgery*. Journal of Magnetic Resonance Imaging **27** (2), 391-399 (2008).
- [4] E. Martin, D. Jeanmonod, A. Morel, E. Zadicario, B. Werner. *High intensity focused ultrasound for non-invasive functional neurosurgery*. Annals of Neurology **66**, 858-861 (2009).
- [5] G. Schaltenbrand, W. Wahren. *Atlas for stereotaxy of the human brain*. (Thieme, Stuttgart, 1977).
- [6] A. Morel. *Stereotactic atlas of the human thalamus*. (Informa Healthcare, New York, 2007).
- [7] H. C. Burck. *Histologische Technik*. 5th edn. (Thieme, Stuttgart, 1982).
- [8] B. Romeis, P. Böck. *Mikroskopische Technik*. 17th edn. (Urban & Fischer, München, 1989).
- [9] R. Quester, R. Schröder. *The shrinkage of the human brain stem during formalin fixation and embedding in paraffin*. Journal of Neuroscience Methods **75**, 81-89 (1997).
- [10] A. Andronache, M. von Siebenthal, G. Székely, P. Cattin. *Non-rigid registration of multi-modal images using both mutual information and cross-correlation*. Medical Image Analysis **12**, 3-15 (2008).
- [11] R. A. Brooks, G. Di Chiro, M. R. Keller. *Explanation of cerebral white - gray contrast in computed tomography*. Journal of Computer Assisted Tomography **4**, 489-491 (1980).
- [12] M. Germann, A. Morel, F. Beckmann, A. Andronache, D. Jeanmonod, B. Müller. *Strain fields in histological slices of brain tissue determined by synchrotron radiation-based micro computed tomography*. Journal of Neuroscience Methods **170**, 149-155 (2008).
- [13] J. Als-Nielsen, D. McMorrow. *Elements of Modern X-ray Physics*. (John Wiley & Sons, Chichester, 2011).

-
- [14] A. Momose, J. Fukuda. *Phase-contrast radiographs of nonstained rat cerebellar specimen*. *Medical Physics* **22**, 375-379 (1995).
- [15] R. Fitzgerald. *Phase-sensitive X-ray imaging*. *Physics Today* **53**, 23-26 (2000).
- [16] A. Momose. *Recent advances in X-ray phase imaging*. *Japanese Journal of Applied Physics Part 1* **44**, 6355-6367 (2005).
- [17] U. Bonse, M. Hart. *An X-ray interferometer*. *Applied Physics Letters* **6**, 155-156 (1965).
- [18] F. Beckmann, U. Bonse, F. Busch, O. Günnewig, T. Biermann. *A novel system for X-ray phase-contrast microtomography*. *HASYLAB Jahresbericht*, 691-692 (1995).
- [19] A. A. Snigirev, I. Snigireva, V. Kohn, S. Kuznetsov, I. Schelokov. *On the possibilities of x-ray phase contrast microimaging by coherent high-energy synchrotron radiation*. *Review of Scientific Instruments* **66**, 5486-5492 (1995).
- [20] P. Cloetens, R. Barrett, J. Baruchel, J.-P. Guigay, M. Schlenker. *Phase objects in synchrotron radiation hard X-ray imaging*. *Journal of Physics D: Applied Physics* **29**, 133-146 (1996).
- [21] K. A. Nugent, T. E. Gureyev, D. F. Ciukson, D. Paganin, Z. Barnea. *Quantitative phase imaging using hard X-rays*. *Physical Review Letters* **77**, 2961-2964 (1996).
- [22] S. W. Wilkins, T. E. Gureyev, D. Gao, A. Pogany, A. W. Stevenson. *Phase-contrast imaging using polychromatic hard X-rays*. *Nature* **384**, 335-338 (1996).
- [23] P. Cloetens, W. Ludwig, J. Baruchel, D. Van Dyck, J. Van Landuyt, J. P. Guigay, M. Schlenker. *Holotomography: Quantitative phase tomography with micrometer resolution using hard synchrotron radiation X-rays*. *Applied Physics Letters* **75**, 2912-2914 (1999).
- [24] A. Pradel, M. Langer, J. G. Maisey, D. Geffard-Kuriyama, P. Cloetens, P. Janvier, P. Tafforeau. *Skull and brain of a 300-million-year-old chimaeroid fish revealed by synchrotron holotomography*. *Proceedings of the National Academy of Sciences* **106**, 5224-5228 (2009).
- [25] E. Förster, K. Goetz, P. Zaumseil. *Double crystal diffractometry for the characterization of targets for laser fusion experiments*. *Kristall und Technik* **15**, 937-945 (1980).
- [26] T. J. Davis, D. Gao, T. E. Gureyev, A. W. Stevenson, S. W. Wilkins. *Phase-contrast imaging of weakly absorbing materials using hard X-rays*. *Nature* **373**, 595-598 (1995).
- [27] D. Chapman, W. Thomlinson, R. E. Johnston, D. Washburn, E. Pisano, N. Gmür, Z. Zhong, R. Menk, F. Arfelli, D. Sayers. *Diffraction enhanced X-ray imaging*. *Physics in Medicine and Biology* **42**, 2015-2025 (1997).

- [28] C. David, B. Nöhammer, H. H. Solak, E. Ziegler. *Differential X-ray phase contrast imaging using a shearing interferometer*. Applied Physics Letters **81**, 3287-3289 (2002).
- [29] A. Momose, S. Kawamoto, I. Koyama, Y. Hamaishi, K. Takai, Y. Suzuki. *Demonstration of X-ray Talbot interferometry*. Japanese Journal of Applied Physics Part 2 **42**, 866-868 (2003).
- [30] T. Weitkamp, A. Diaz, C. David, F. Pfeiffer, M. Stampanoni, P. Cloetens, E. Ziegler. *X-ray phase imaging with a grating interferometer*. Optics Express **13**, 6296-6304 (2005).
- [31] F. Pfeiffer, O. Bunk, C. David, M. Bech, G. Le Duc, A. Bravin, P. Cloetens. *High-resolution brain tumor visualization using three-dimensional X-ray phase contrast tomography*. Physics in Medicine and Biology **52**, 6923-6930 (2007).
- [32] F. Pfeiffer, C. David, O. Bunk, C. Poitry-Yamate, R. Grütter, B. Müller, T. Weitkamp. *High-sensitivity phase-contrast tomography of rat brain in phosphate buffered saline*. Journal of Physics: Conference Series **186**, 0120461-3 (2009).
- [33] F. Pfeiffer, O. Bunk, C. Kottler, C. David. *Tomographic reconstruction of three-dimensional objects from hard X-ray differential phase contrast projection images*. Nuclear Instruments and Methods in Physics Research Section A: Accelerators, Spectrometers, Detectors and Associated Equipment **580**, 925-928 (2007).
- [34] F. Pfeiffer, T. Weitkamp, O. Bunk, C. David. *Phase retrieval and differential phase-contrast imaging with low-brilliance X-ray sources*. Nature Physics **2**, 258-261 (2006).
- [35] F. Pfeiffer, C. Kottler, O. Bunk, C. David. *Hard X-ray phase tomography with low-brilliance sources*. Physical Review Letters **98**, 108105 (2007).
- [36] M. Trepel *Neuroanatomie / Struktur und Funktion*. 4th edn. (Urban & Fischer, München, 2008).
- [37] A. Lareida, F. Beckmann, A. Schrott-Fischer, R. Glueckert, W. Freysinger, B. Müller. *High-resolution X-ray tomography of the human inner ear: synchrotron radiation-based study of nerve fiber bundles, membranes, and ganglion cells*. Journal of Microscopy **234**, 95-102 (2009).
- [38] E. T. Ahrens, D. H. Laidlaw, C. Readhead, C. F. Brosnan, S. E. Fraser, R. E. Jacobs. *MR microscopy of transgenic mice that spontaneously acquire experimental allergic encephalomyelitis*. Magnetic Resonance in Medicine **40**, 119-132 (1998).
- [39] H. Benveniste, S. Blackband. *MR microscopy and high resolution small animal MRI: Applications in neuroscience research*. Progress in Neurobiology **67**, 393-420 (2002).

-
- [40] G. M. Fatterpekar, T. P. Naidich, B. N. Delman, J. G. Aguinaldo, S. H. Gultekin, C. C. Sherwood, P. R. Hof, B. P. Drayer, Z. A. Fayad. *Cytoarchitecture of the human cerebral cortex: MR microscopy of excised specimens at 9.4 Tesla*. American Journal of Neuroradiology **23**, 1313-1321 (2002).
- [41] G M. Fatterpekar, B. N. Delman, W. W. Boonn, S. H. Gultekin, Z. A. Fayad, P. R. Hoff, T. P. Naidich. *MR microscopy of normal human brain*. Magnetic Resonance Imaging Clinics of North America **11**, 641-653 (2003).

Acknowledgements

This work could only be successful with the support of many people. It is a great pleasure for me to express my gratitude to everyone for the support and contributions during the last years.

First of all I want to thank my “Doktorvater” **Prof Dr. Bert Müller** for giving me the opportunity to work on this PhD thesis at the Biomaterials Science Center. I have to thank for all the discussions and approaches to challenging problems. I thank **Prof. Dr. Ernst Meyer** for kindly acting as co-referee and for the evaluation of my thesis.

Furthermore, I thank **Prof. Dr. Franz Pfeiffer** from TU München, **Dr. Timm Weitkamp** from SOLEIL and **Dr. Christian David** from PSI for introducing me into phase contrast computed tomography.

I would like to express my gratitude to **Prof. Dr. Philippe Cattin** for supporting me during challenging programming problems in MATLAB and **Dr. Adrian Andronache** for the availability of the registration tool.

Sincere thanks are given to **Dr. Irene Zanette** for giving me support during all the beamtimes at ESRF and **Dr. Felix Beckmann** during the beamtimes at DESY and for introducing me into the field of computed tomography.

The PhD thesis was based on the work of **Dr. Marco Germann**. Thank you for the introduction into this interesting topic and the support in medical questions.

Special thanks go to all the members of the Biomaterials Science Center for the great atmosphere, especially **Hans Deyhle** for all the fruitful discussions and **Maggie Holme** for the great help as native speaker.

I gratefully acknowledge **Prof. Dr. Magdalena Müller-Gerbl** and **Peter Zimmermann** for the organization and extraction of the human brain.

I would like to thank **Dr. Anne Morel** and **Martha Imholz** for the excellent support during medical questions and for histology.

I am very grateful to **Dr. Henk-Joost Crooijmans** and **Dr. Conny Waschkies** for carrying out the magnetic resonance imaging and magnetic resonance microscopy experiments.

Very special thanks go to **Dr. Julia Herzen** and **Marian Willner** for the support and fruitful discussions during the long sleepless beamtime nights in Hamburg and Grenoble.

Last but not least I thank to all my friends with whom my life was always exciting and my parents for giving me all the assistance I needed and for making my studies possible. Most of all I thank **Karo** for enriching my life with her love and for all the support during the last four years.

Curriculum Vitae

Family Name: Schulz
First Name: Georg
Citizenship: Germany
Date of Birth: 31.07.1980
Place of Birth: Fergana, Usbekistan

Education

2008-2012 Doctor of philosophy (PhD) in experimental physics
at University of Basel, Switzerland (Prof. B. Müller)
2001-2008 Diploma in theoretical physics
at Albert-Ludwigs-University in Freiburg i. Breisgau,
Germany (Prof. J. Briggs)
1993-2000 University-entrance diploma
at Gymnasium Melle, Germany

Professional Experience

2008-2012 PhD work at Biomaterials Science Center,
University of Basel, Switzerland
2008 Scientific assistant,
Theoretical Quantum Dynamics,
Institute of Physics,
University of Freiburg i. Breisgau, Germany
2007-2008 Supervising tutor for laboratory courses for first-year students,
Institute of Physics,
University of Freiburg i. Breisgau, Germany
2000-2001 Military Service in Fürstenu, Germany